A study on the response of a target plate to a foreign object placed at various depths in a cylindrical charge.

M.M. Hoare

MSc Dissertation

in the Department of Mechanical Engineering

Faculty of Engineering and the Built Environment

University of Cape Town

February 2023

Declaration

I, Matthew Michael Hoare, know the meaning of plagiarism and declare that all the work in the document, save for that which is properly acknowledged, is my own. This thesis/dissertation has been submitted to the Turnitin module (or equivalent similarity and originality checking software) and I confirm that my supervisor has seen my report and any concerns revealed by such have been resolved with my supervisor. I am now presenting the report for examination for the degree of M.Sc Eng (Mechanical).

Signed by candidate

M.M. Hoare

February 2023

Abstract

The threat of Improvised Explosive Devices (IEDs) has grown exponentially in the 21st century, as the methods and means of warfare have adapted to modern threats such as terrorism. IEDs are especially damaging and lethal because they are often randomly embedded with a variety of projectiles that consist of readily available items, such as ball bearings, nails or glass. The versatile nature of IEDs makes it very difficult to conduct a generalised study on their impact. One major challenge in IED research is the wide range of potential IED geometries, sizes, explosion types and embedded object configurations. Understanding the behaviour of a simplified IED, consisting of a blast-driven ball bearings embedded in explosive charges, will provide insights into the mechanics of IEDs and its subsequent interactions with a target with a view to developing better protection from IEDs.

This dissertation presents the results of a study investigating the damage caused by a simplified IED which consists of a cylindrical explosive charge that was embedded with a single ball bearing. The influence of the placement of a ball bearing along the axis within a rear-detonated cylindrical charge was studied and the placement effects were evaluated in terms of the impact velocity of the ball bearing and its subsequent damage on a Domex 700 steel (also referred to as Strenx in Europe) target plate. Typical deformation of a structure from an IED is a result from of blast loading (pressure wave) and impact loading from the shrapnel/fragment. In this study the combined blast and impact events of a simplified IED were decoupled into separate events to gain a better understanding of the contributions of the different loading conditions. The target plates were exposed to bare charges to quantify the effects on blast loading events. Impact tests were carried out using a two-stage gas gun to relate impact velocity to the deflection of the target plate. Tests were also carried out with explosive charges embedded with a ball bearing at

varying depths to analyse the combined event. For all blast tests, the charge diameter was kept constant. Three different charge masses with varying placements of the ball bearing were investigated. Computational simulations, validated using experimental data, were used to elucidate additional details to gain insight about the momentum transfer during the blast event. The results showed similar critical influence of the placement of the ball bearing relative to the charge for the different charge masses used.

Acknowledgements

I would like express my sincere gratitude to my primary supervisor, Prof. Steeve Chung Kim Yuen for his support and guidance throughout this project. Thank you for your advice, support and thorough proof-reading. Without your help, this dissertation would not have come to fruition.

To my co-supervisors, Dr Reuben Govender and Dr Trevor Cloete. Your input in this project was greatly appreciated. Dr Reuben Govender, your help with the hopkinson bar set up was vital, along with the help you provided with the electronics. Dr Trevor Cloete, your aid with the two stage gas gun was essential to calibrating and gathering the data correctly.

To my research partner, Pierre Van Der Merwe. The many discussions had about our projects and research helped to overcome many problems that occurred along the way. Your support meant a lot to me.

I would like to extend my thanks and appreciation to the Masters Crew within the BISRU research group for their help and support. As well as the many dart games played.

I would like to acknowledge the staff members of the UCT mechanical workshop for machining many of the experimental parts. I would like to thank Penny Louw for her help in conducting the tensile tests of the Domex 700.

And finally I would like to thank my friends, family, and loved ones. Not only for your unending support through my Masters degree, but throughout my educational journey. Your support and guidance motivated me and kept me going.

Contents

List of Figures

List of Tables

Chapter 1

Introduction

1.1 Background and Motivation

Improvised Explosive Devices (IEDs) are widely used by insurgents and armed groups as a way of disrupting the equipment and personnel of opposing forces, and often inflicting casualties to civilians in the vicinity. IEDs have caused more civilian deaths than any other explosive weapon type for the last decade. From October 2010 through to the end of September 2020, over 28000 incidents of explosive violence were reported in English-speaking media, resulting in over 25000 casualties. 48% of the casualties were affected by from improvised explosive devices [1].

IEDs are often described as home-made bombs or destructive devices. They are found in many shapes and forms, ranging from small pipe bombs to massive devices designed for inflicting high numbers of casualties and structural damage [2]. The improvised aspect of the device means that detection can often be difficult as all the components in the device are not standardized. IEDs may also be surrounded or packed with other materials such as glass, nails or metal fragments to enhance the lethality of the device. Chemical components may also be added [2].

The added component of shrapnel such as nails, ball bearings or any small metal ob-

jects, inflicts additional damage to the blast loads. An example of this was the IED used in the Manchester Arena Bombing which killed 23 people (including the attacker) [3] and over 100 were admitted to hospitals [4]. Understanding the behaviour of shrapnel when located at different places within a charge was gained, shrapnel placed closer to the edge of the charge remains a greater cause for concern for injuries and damage to humans and equipment. With this greater understanding, engineers can design better preventative measures to mitigate or remove any damage to equipment and reduce human casualties.

This dissertation presents the results of a study investigating the damage caused by a simplified IED which consists of a rear-detonated cylindrical explosive charge that was embedded with a single ball bearing. The influence of the placement of a ball bearing along the axis within a rear-detonated cylindrical charge, as shown in Figure 1.1, was studied. The placement effects were evaluated in terms of the impact velocity of the ball bearing and its subsequent damage on a Domex 700 steel target plate. In this study the combined blast and impact tests were investigated as two separate events. A two-stage gas gun was used to investigate the effects of shrapnel, idealised as ball bearings, impacting target plates at varying impact velocity ranges ($82m \cdot s^{-1}$ to $506m \cdot s^{-1}$). Additionally, target plates were exposed to a bare cylindrical charge to investigate the effect of blast waves of a target plate. Subsequently, target plates were exposed to tests where a ball bearing was embedded at varying depths within a cylindrical charge of identical mass to the bare charge tests to investigate the combined event against the impact tests and blast tests. The charge diameter was kept constant at $20mm$ and three charge sizes were used, namely $10g$. $20g$ and $30g$. Computational simulations, once validated via experimental work, were used to elucidate more information about the blast wave interactions within the experimental tests, and to gain additional data to expand on the experimental work. The results showed similar critical influence of the placement of the ball bearing relative to the charge for the different charge masses used.

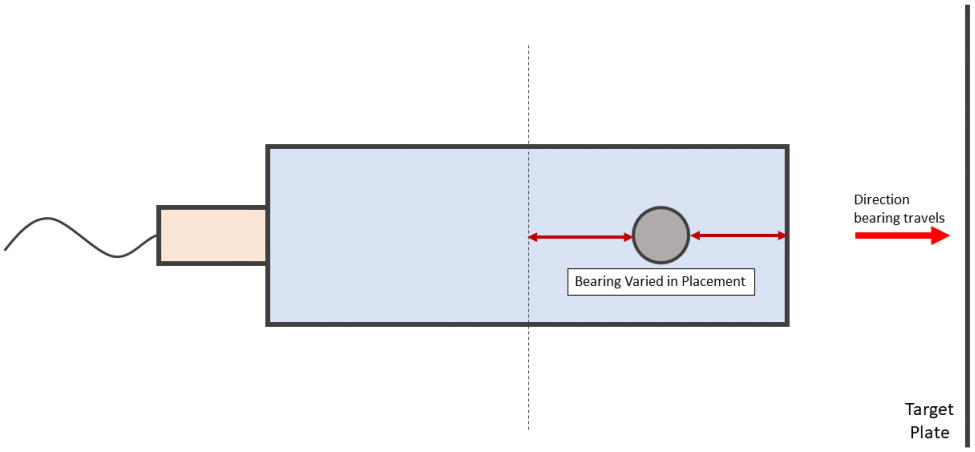

Figure 1.1 Schematic illustrating the layout for potential bearing placement in several locations inside a charge.

1.2 Aim of Study

The main aim of this dissertation was to study how a ball bearing placed at different depths along the axis of a cylindrical charge, with varied mass, affected the response of a steel target plate and to investigate the loading contributions of each loading event within the combined loading.

1.3 Objectives of Study

The aim of this project was achieved by fulfilling the following objectives:

- Investigate the response of a target plate to only blast loading.
- Investigate the response of a target plate to only impact testing.
- Investigate the response of a target plate to combined blast and impact testing in the following manner:
  - Investigate how the length of a charge with a constant diameter affects the velocity of the ball bearings and the damage the ball bearing causes to a steel target plate.

  - Investigate how the depth of a ball bearing along the cylindrical axis of a charge affects the velocity of the ball bearing and the damage the ball bearing causes to a steel target plate.

- Formulate a numerical simulation to replicate a blast-driven ball bearing for varying bearing depths and charge lengths at a target plate.
- Conduct a parametric study, using both numerical simulations and experiments, to compare how the length of the charge and depth of the ball bearing in the charge along the cylindrical axis affects a target plate deflection.
- Use the data gathered to draw conclusions and recommendations on the investigation.

1.4 Scope and Limitations

The dissertation focused on the effects of the ball bearing placement along the cylindrical axis of a charge and its subsequent effect on the impact velocity of the ball bearing and the response of a target plate. In addition, the effect of the length of a charge was investigated in terms of the impact velocity of a ball bearing at various depths along the cylindrical axis. The research was carried out both computationally and experimentally. While some basic material properties for Domex 700 were determined for computational reasons, more in depth material characteristics, especially those relating to dynamic properties and material model failure were not carried out. The material model implemented in the computation work was, therefore, only examined in the plastic deformation of the target plate. Failure that included tearing could not simulated.

The deformation of the ball bearing after testing was not examined. The variation in charge diameter on the ball bearings velocity was also not investigated. The target plate was kept perpendicular to the flight of the bearing. The charge masses were limited to a maximum of 75g of PE4.

1.5 Thesis Development

A review of relevant literature is presented in Chapter 2. This is followed by the experimental arrangements used to achieve the first two objectives, which are presented in Chapter 3. The results from the experimental arrangements are presented in Chapter 4. The numerical simulation set-up and the results of the numerical set-up are presented in Chapters 5 and 6 respectively. The results are then discussed in Chapter 7, with conclusions and recommendations for future research being presented in Chapter 8.

Chapter 2

Literature Review

In this chapter, literature from past studies that relate to this research will be discussed. The Chapter includes blast theory, blast propagation and fragmentation.

2.1 Improvised Explosive Devices

An improvised explosive device (IED) is a home-made bomb that is frequently used by insurgents and other non-state military groups [5]. IEDs are crude weapons that can be used against military personnel, vehicles or structures.

2.1.1 Elements of an Improvised Explosive Device

All IEDs consist of a switch or trigger, an initiator, an explosive or main charge and a power source [2], as indicated in Figure 2.1. IEDs can often be packed with other components such as ball bearings or nails to create deadly shrapnel once detonation occurs [6].

The individual components of an IED can vary depending on its intended use. Different types of triggers are used, with the most common being initiated by a human via a receiver. Common examples of the trigger would be cell phones, a switch and battery or even an infra-red beam [5]. Some examples of the explosives used would be mortar rounds, aerial bombs, fertilizers, TNT and gunpowder. The explosives normally contain

an oxidizer and a fuel source such as ammonium nitrate/fuel oil (ANFO), with ammonium nitrate acting as the oxidizer and oil serving as the fuel source [2, 7]. Table 2.1 lists common types of explosives used in IEDs. IEDs can also contain other elements to increase damage and psychological effect such as mechanical, radiological, chemical, and biological components. An example of nails being used in an IED was the Atlanta Olympic park bombing in 1996, when nails were packed into the bomb killing two people and injuring many more [2]. The size of an IED can also vary by shape and size, from the size of a landmine or vest to a truck [5, 8].

Table 2.1 *Table listing the common explosives used in IEDs [2].*

Explosive Type	**Common Uses**	**Common Form**	**Known IED use**
Ammonium nitrate and fuel oil (ANFO)	Mining and blasting	Solid	Oklahoma City bombing
Triacetone Triperoxide (TATP)	Mixed with other materials	Crystalline Solid	2005 bombings in London
Semtex, C-4	Military	Plastic Solid	Irish Republican Army bombings
Ethylene glycol dinitrate (EGDN)	Component of low freezing dynamite	Liquid	Millennium Bomber, LA 1999
Urea nitrate	Fertilizer	Crystalline solid	World Trade Center 1993
Smokeless powder	Ammunition	Solid	Olympic Park bombings

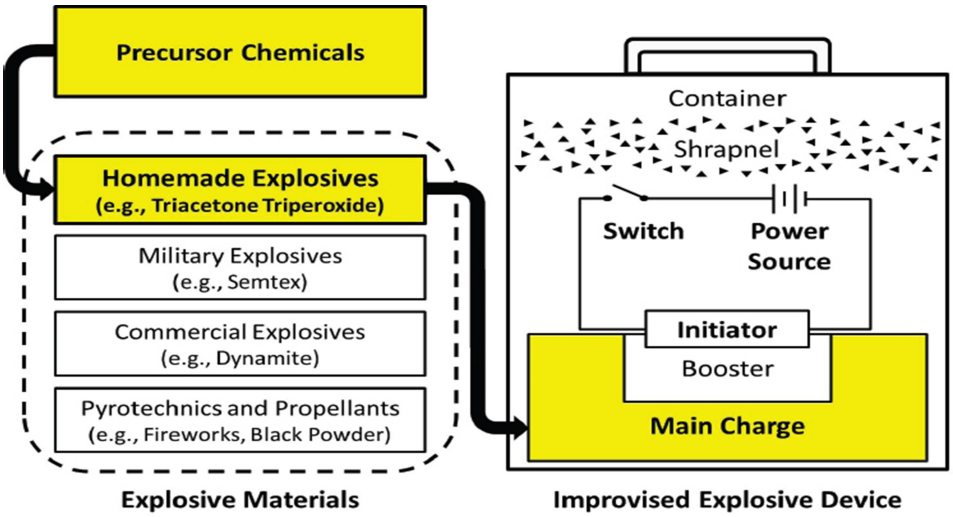

Figure 2.1 Schematic of the contents of an IED [9].

2.1.2 Common uses and impacts of an Improvised Explosive Device

IEDs have been shown to be very effective in the field of war. They have been hidden behind signs or even camouflaged to look like debris or inside animal carcasses to prevent detection [10], allowing for the targets, be that people or mechanical devices, to get close before detonation occurs. This process allows for maximum damage and casualties. Depending on the size of the IED used, the damage caused to a building is usually devastating. A delivery truck used as an IED would cause damage up to a distance of 1500m from the blast point, indicating the magnitude of the harm that an IED can cause [2]. Injuries to humans involved are immediate or delayed depending on the type of IED detonated and distance between source of charge and target. Common immediate health problems would be from over pressure damage (damage to the ears and lungs), fragmentation injury (projectiles penetrating the body), impact injuries (broken bones or amputations) and thermal injuries (burn injuries). Chemical or biological components in the IED may cause added injuries. Post-traumatic stress disorder has also often been associated with IEDs [2].

Two examples of an IED attack include the Oklahoma City bombing in 1995 and the Atlanta Olympic park bombing in 1996. In the Oklahoma City Bombing, a truck was used to deliver the blast load. At the time, it was the worst terrorist attack in the United

States, killing 169 people [9]. In the Atlanta Olympic park bombing, IEDs in the form of pipe bombs with nails added as shrapnel were used, killing two people and injuring over 100 people [9, 11].

2.2 Review of explosives

Upon detonation, IEDs can have both blast and projectile impacting the surrounding people or structures. Due to the complexities of the combined blast and projectile impact loads, the problem was simplified and investigated separately before analysing the coupled problem.

2.2.1 Characterisation of explosions

Explosions are created by a substance or device that can create a volume of rapidly expanding gas in an extremely short time period [12], and release an intense burst of energy in a few seconds [13]. Consequently, explosives are regarded as violent, sudden, noisy and often startling [14]. Explosions can be classified into three categories: mechanical explosions(a pressurised vessel exploding), nuclear explosions (atomic bomb), and chemical explosions (plastic explosive) [12, 14]. Chemical explosives can be classified into two explosive mechanisms, namely detonation and deflagration. Detonations are characterised by extremely rapid decomposition while deflagration involves the fast burning of the material [12]. Detonating explosives are usually divided into two categories, primary and secondary categories. Primary explosives detonate by ignition from a source such as a spark or an impact. Secondary explosives require a detonator or a supplementary booster to detonate [12].

2.2.2 Pressure History from Blast Events

Goel et al. [15, 16] discussed the blast wave parameters and the pressure profile associated with blast waves including the distance from the blast, type of explosive and the point in which the pressure is measured, such as air or surface. Explosives contain large amounts of concentrated energy. When a detonation occurs, and the charge explodes the energy is

released quickly and moves outward from the centre of the explosion [15]. This outward movement of energy causes the surrounding medium to compress and move outward with a velocity front. The velocity front, or peak, is referred to as the blast wave which is determined by both the size and shape of the charge before detonation as well as the distance from the detonation point [15].

Figure 2.2 depicts the typical pressure history generated by a blast load, characterized by an almost instantaneous increase in pressure from the ambient pressure, P_a, to its peak, P_{SO}. Thereafter, the peak over pressure decays exponentially with time to below the ambient pressure and finally back up to the ambient pressure. The period during which the pressure is less than the ambient pressure is referred to as the negative duration.

When the pressure is greater than the ambient pressure (period between T1 and T2), it is referred as the positive period [15]. The impulse of a positive blast profile can also be deduced using integration, as shown in Equation 2.1, where the integral limits are determined by the positive pressure times.

$$I = \int_{A1}^{A2} \int_{T1}^{T2} P(t) dA dt \tag{2.1}$$

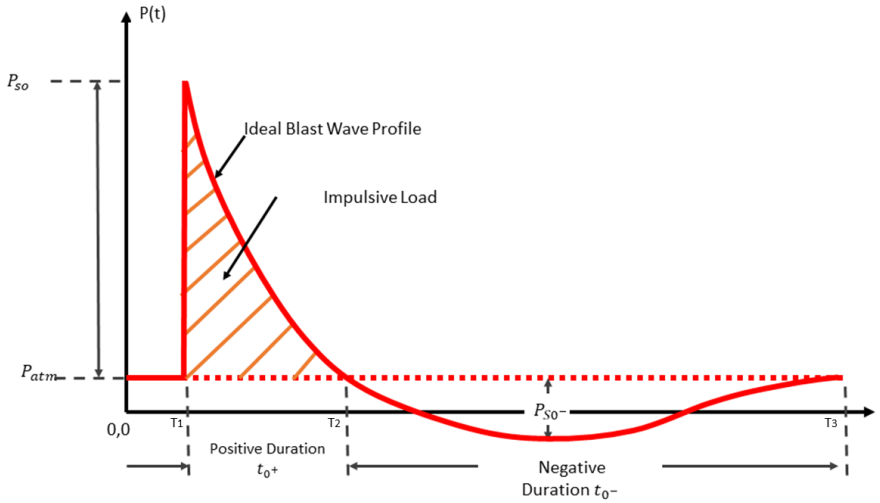

Figure 2.2 Graph illustrating the typical blast wave pressure profile for spherical charges [15].

The blast pressure profile was derived from Friedlander's equation, and the modified Friedlander equation (Equation 2.2)is described by Goel *et al.* [16].

$$P(t) = P_O + P_{POS}(1 - \frac{t}{t_{pos}})e^{-b\frac{t}{t_{pos}}} \tag{2.2}$$

Where $P(t)$ is the time-dependent pressure, P_O is the ambient air pressure, t_{pos} is the positive duration of the pressure and b is the dimensionless wave decay coefficient. t and t_o is the time of arrival for the pressure wave in milliseconds. The pressure profile shown in Figure 2.2 was derived by Kinney and Graham [17] who determined the pressure profile for the positive phase uniquely for the 1kg of TNT and described mathematically as shown in Equation 2.3.

$$P(t) = P_{max}(1 - \frac{t}{t_d})e^{\frac{\alpha t}{e^t d}} \tag{2.3}$$

Where α is a time constant that depends on the pressure factor P_{max}/P_O and t_d is the duration of the positive phase.

The maximum overpressure not only decreases in time but also with distance. As the distance between the point of detonation and location of measurement increases, the peak pressure decreases in magnitude as depicted in Figure 2.3 [18]. Figure 2.3 shows the different profiles at different distances from the blast centre. Note that $t_3 > t_2 > t_1$, while $P_1 > P_2 > P_3$, showing that magnitude and time are dependent on the distance from the blast.

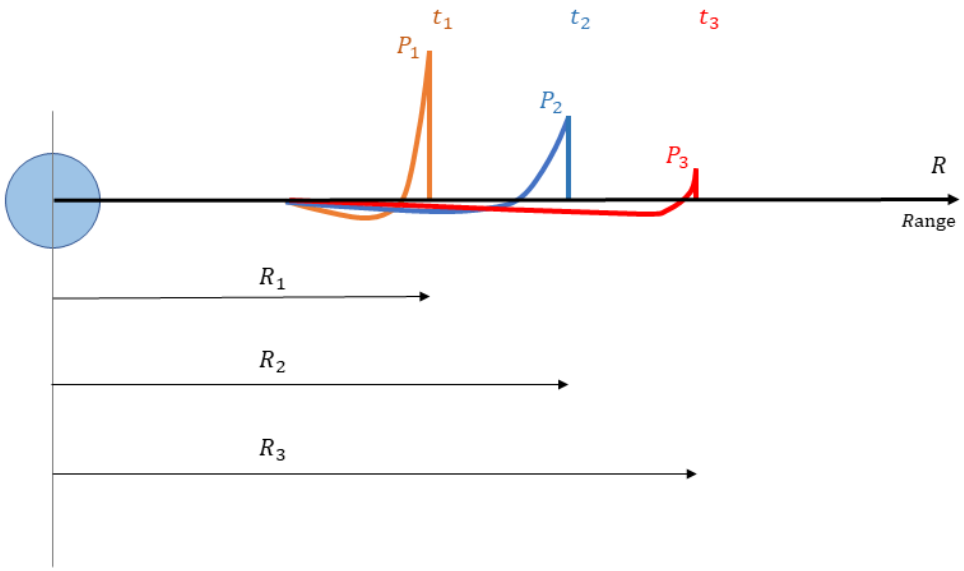

Figure 2.3 Illustration of the spatial profile of the blast wave for different times/distances [18].

2.2.3 Theories of Detonation

Many theories and blast models have been proposed to gain an understanding of explosions, the effect of blast loads and its subsequent effect on structures. While there are many aspects to blast theories, two broad categories are discussed in this section, namely the simple or ideal blast theories and the non-ideal blast theory.

2.2.3.1 Ideal detonation theory

Given that the detonation process is not simple, it is idealised in terms of a chemical reaction, where the thermodynamics and kinetics have to be quantified, and the shock hydrodynamics and fluid dynamics governing the expanding gas flow behind the detonation wave are examined [13]. Chapman [19] and Jouguet [20] each described an ideal theory independently of each other. The combined Chapman-Jouguet model (CJ) is also one of the simplest models describing blasts. This model assumes that the products from

the thermodynamic reaction reach equilibrium instantaneously [13].

A pressure versus specific volume graph can be used to represent various points in the ideal theory. In Figure 2.4, the Hugoniot curves (which describe the the conservation of energy for reacted and unreacted explosive products) and the Rayleigh line (which describes the conservation of mass and momentum from the unreacted explosives to the detonated products) are depicted [21]. As depicted in Figure 2.4, at some point in the charge before detonation, the charge is characterised by point A, which shows the initial condition where the explosive is still not shocked and unreacted. As the shock wave reaches point A, it experiences large amounts of pressure with a small decrease in volume, which then refines the characteristics of that point and it moves up the Hugoniot curve to point C, which shows the jump to fully shocked but yet unreacted explosive material. Once the front has passed and the charge mass at that point has reacted, it travels down the Rayleigh line to Point B, which sits on the Hugoniot curve of Detonation Products. The CJ point, as depicted in Figure 2.4, (Point B) represents the hypothesized steady-state detonation condition depicting the state of products behind the detonation front.

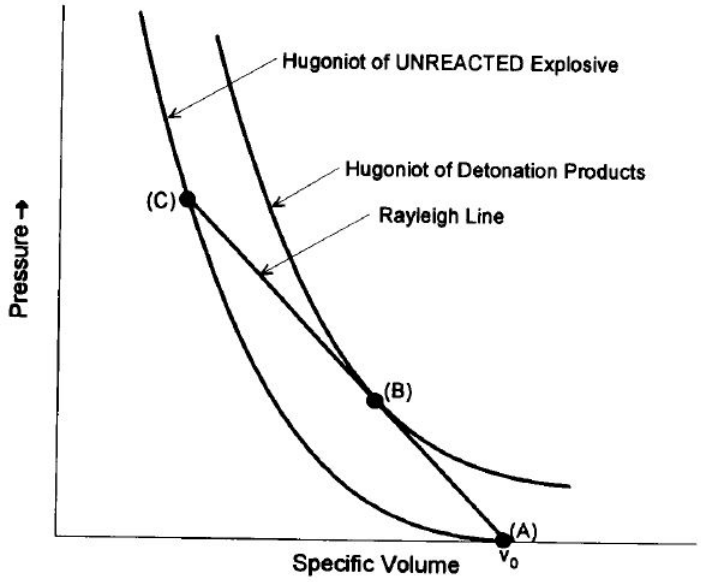

Figure 2.4 Graph depicting the pressure versus specific volume graph showing Hugoniots and Rayleigh line. [13].

The Hugoniot line shown in Figure 2.4, indicates the two materials (the unreacted explosive material and the reacted gas products) in a denotation jump condition.

Zeldovich [22], Von Neumann [23] and Doring [24] also proposed other ideal theories referred to as the ZND theory [13] or the simple theory. In the ZND model, the shock wave has no thickness and acts purely as an interface between the reacted and unreacted explosives, while the gas flow after the reaction zone follows the same assumptions as the CJ model.

2.2.3.2 Non-Ideal theory

Explosives tend to have a lower energy density than ideal theories propose, a finite time of energy release and need confinement to trigger an explosion. While explosive are idealised as spherical, this rarely happens in real life scenarios as explosives come in different shapes [25]. Hills *et al.* [26] showed that real detonations usually have a curved shock front, which differs from ideal shock theories. The curvature is also strongly influenced by the detonation properties.

The Detonation Shock Dynamics (DSD) theory is a non-ideal model, developed by Bdzil and Stewart [27, 28] which was further extended by Aslam *et al.* [29]. The detonation propagation is described by an analytical expression for the detonation speed, D_n, that depends on only front-related variables. DSD was found to produce accurate shock wave propagation results compared to other numerical simulations. The DSD method for modelling propagation is based on three elements [30], namely:

1. A sub-scale theory of multi-dimensional detonation where the dynamics depend only on metrics of the front of the wave.
2. High-resolution, direct numerical simulation of the detonation using Euler description models (which describes fluid flow through an area or cell).
3. Physical experiments to measure and characterise propagation in real explosives and to provide data to validate and calibrate DSD front models against.

Bdzil *et al.* [28] and Stewart *et al.* [27] further assumed that the shock wave has a curved detonation front as a result of lateral expansion. Within the reaction area the local shock speed can be described mathematically as shown in Equation 2.4.

$$u + c \approx D_n \tag{2.4}$$

Where D_n is the local shock speed and u is the particle velocity. The shock wave speed D_n for an uncased charge is given as,

$$D_n = Dcos(\theta_M) \tag{2.5}$$

where θ_M is the angle between the normal of the shock to the direction of the shock wave propagation.

Chiquete *et al.* [31] developed a theory to include a surface evolution model for the detonation propagation dynamics of a conventional high explosive. The theory was based on the concept of DSD and related to the speed of the shock wave, D_n, and the curvature of the wave, k. Figure 2.5 shows the typical nature of the curved front assumed in the DSD model. Where ϕ represents the angle between the normal of the shock to the direction of the shock wave propagation rather than θ_M previously.

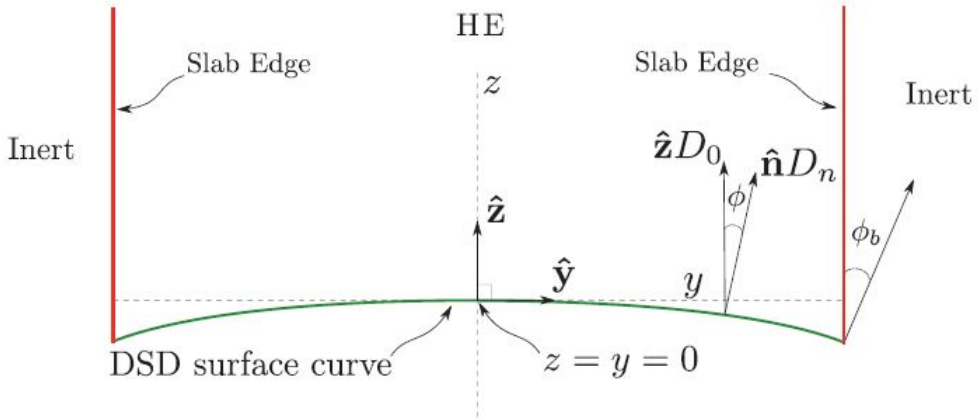

Figure 2.5 Schematic highlighting the 2D system and geometry for the DSD calibration of a curved blast front [31].

2.2.4 Blast Scaling

An important factor in analysing blasts waves and their features is the stand-off distance (SOD). The SOD is the distance from the charge to the target or point of interest. A well cited scaling law referred to as the Hopkinson Law[32], where the scaled distance (Z) is represented a single equation by both the distances to the source of the blast (R) and the equivalent TNT mass of charge (W_{TNT}) and expressed mathematically (Equation 2.6) to simplify the effects of scaling.

$$Z = \frac{R}{W_{TNT}^{\frac{1}{3}}} \tag{2.6}$$

Hopkinson[32] showed that when the same explosives of similar shape but with different masses were detonated at the same scaled distance, similar blast waves profiles were produced. The Hopkinson scaling law was also used to scale time (Equation 2.7) and impulse (Equation 2.8).

$$\tau* = \frac{\tau}{W_{TNT}^{\frac{1}{3}}} \tag{2.7}$$

$$\zeta = \frac{I}{W_{TNT}^{\frac{1}{3}}} \tag{2.8}$$

Where $\tau*$ is the scaled time and ζ is the scaled impulse. Both equations 2.7 and 2.8 are scaled in terms of W.

2.2.5 Explosive Charge Geometry

The shape of a charge affects the blast wave propagation. For example, spherical charges will have different blast wave patterns to cylindrical charges. While the blast wave is circular from spherical charges, blast waves from cylindrical charges tend to be more complex with overlapping points in the wave fronts which leads to wave summation as depicted in Figure 2.6.

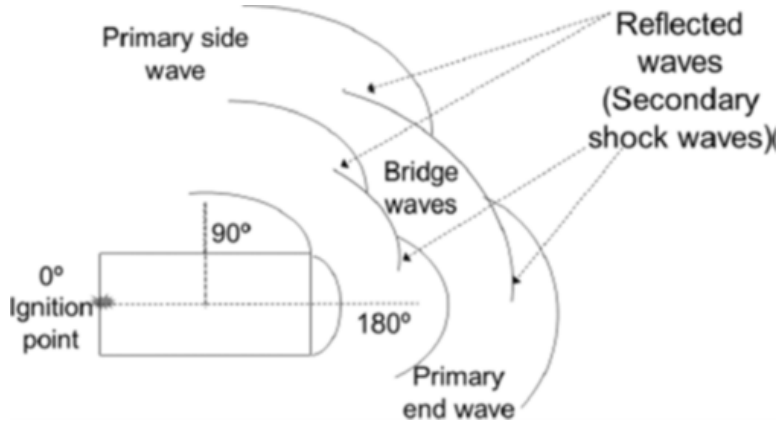

Figure 2.6 Schematic illustrating the development of shock waves from a cylindrical charge [33].

Knock *et al.* [33] performed a study to predict the primary peak overpressure from a cylindrical charge along the axial direction at all distances with charges that have a constant diameter-to-length ratio. The peak pressure of the bare cylindrical charges of the explosive PE4 with a diameter-to-length ratio of 4:1 was found to empirically expressed as Equation 2.9. The experiments were conducted to study the shock waves produced in the axial direction of an explosive charge. With the use of a high-speed camera and pressure gauges, it was possible to observe the formation of side and end shock waves.

$$P = 3075Z^{-3} - 1732Z^{-2} - 205Z^{-1} \tag{2.9}$$

The total impulse transferred was expressed as Equation 2.10.

$$I = K_{11}(\frac{M^{\frac{2}{3}}}{R})^3 - K_{12}(\frac{M^{\frac{2}{3}}}{R})^2 + K_{13}(\frac{M^{\frac{2}{3}}}{R}) \tag{2.10}$$

This was due to the fact that the secondary shock wave was moving at an angle to the gauges. The primary peak overpressure at all distances was expressed empirically as shown in Equation 2.11.

$$P = C_1'Z^{-3} - C_2'Z^{-2} - C_3'Z^{-1} \tag{2.11}$$

Where Z is given by Hopkinson Scaled law [32] (shown in Equation 2.6). Knock and Davies [34] conducted further studies in which the blast waves from the curved surface of a cylindrical charge were observed. Evidence showed that it was possible to predict the overpressure (using Equation 2.12),

$$P = \frac{K_p M (\frac{L}{D})^{\frac{1}{3}}}{R^3} \tag{2.12}$$

for any length-to-diameter ratio from the curved side of a cylindrical charge where M is the mass of the explosive, R is the distance from the charge, K_P is an explosive-dependent constant and L and D are the length and diameter of the charge.

When the point where the pressure was measured was placed at a greater distance from the charge, it would conform to a pressure front that was consistent with that of a spherical charge as the blast wave had become more spherical in nature. The pressure can be expressed as Equation 2.13.

$$P = C_1(Z')^{-3} + C_2(Z')^{-2} + C_3(Z')^{-1} \tag{2.13}$$

Where

$$Z' = \frac{M^{\frac{1}{3}} (\frac{L}{D})^{\frac{1}{9}}}{R} \tag{2.14}$$

And C_1, C_2 and C_3 are explosive constants.

2.2.6 Effective Charge Mass

In a review of the Gurney method (discussed in section 2.5.1), Kennedy [35] reported that cylindrical charges were affected by 'side losses'. It was reported that any explosive mass that lies outside of the 60° conical shape that is situated at the opposite end of the cylindrical charge to the detonation point, as demonstrated in Figure 2.7, would not contribute to the forward axial impulse from the charge.

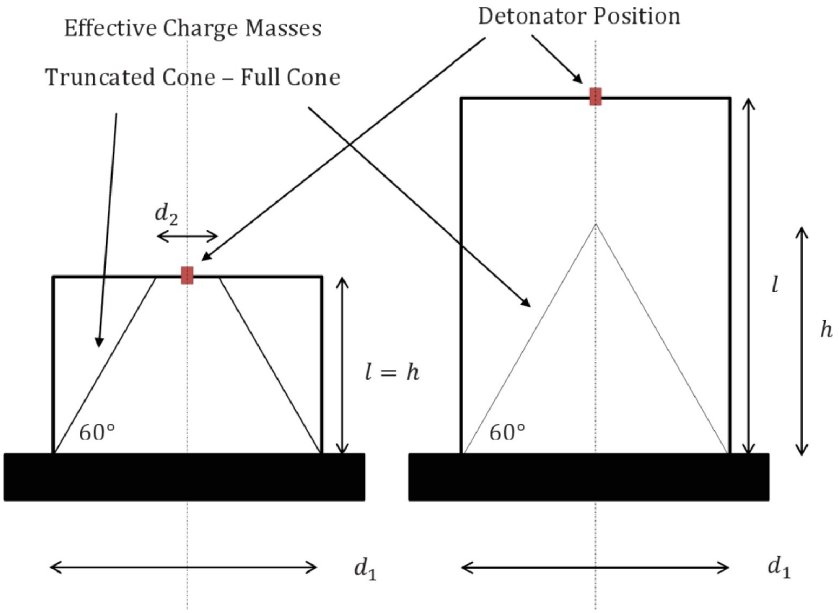

(a) Low aspect ratio (b) High aspect ratio

Figure 2.7 Schematic showing the region of effective or critical charge mass for axial impulse [36].

Figure 2.7 (a) depicts a scenario when the charge height (h) is shorter than the effective charge height (l). In this case,

$$h = l \tag{2.15}$$

The effective mass becomes a truncated cone in shape,

$$mass_{effective} = \rho\tfrac{\pi}{12}(d_1^2 + d_1 d_2 + d_2^2)h \tag{2.16}$$

For charges when $l > h$, as illustrated in Figure 2.7 (b), the effective mass is a cone where the mass is expressed mathematically by Equation 2.17.

$$mass_{effective} = \rho\tfrac{d_1^2 \pi h}{12} \tag{2.17}$$

2.2.7 Equation of State to Calculate the Expansion of Detonation Reaction Products

The Jones-Wilkins-Lee Equation of State (JWL)[37] is one of the most common and widely used equations of states (EOS) used to calculate the expansion of the detonation reaction products from chemical equilibrium. The EOS is based on experimental data gathered by conducting explosive experiments on different shaped metal cylinders to determine the adiabatic expansions caused by the pressure front from explosives. The EOS has been used in explosives to model the pressure-volume-energy relationship and the adiabatic expansion of the detonation products [38]. The first EOS, initially proposed by Jones and Miller [39], was further developed by Wilkins *et al.* [40] and refined by Lee *et al.* [37]. The equation for the JWL equation of state is described by Equation 2.18.

$$P = A(1 - \frac{w}{R_1 V})e^{-R_1 V} + B(1 - \frac{w}{R_2 V})e^{-R_2 V} + \frac{wE}{V} \tag{2.18}$$

Where V is the relative volume with V_O being the initial volume. V_O is calculated using the initial density of the explosive. A, B, R_1, R_2 are parameters based on which explosive is being used. The parameter w forms a fraction of the energy (E) that contributes to pressure [41].

2.2.8 Loading Confinement

Structures can affect the blast loading and the resultant pressure waves depending on the presence of other structures around the source of the blast. Consequently, a blast can be defined as either confined, which has structures present around the source of the blast, or unconfined (in open space and only affected by the height and stand-off distance)[42, 43]. As in the UFC 3-340-02 design manual [43], these 2 classifications divide into 3 more subcategories based on the degree of structures present around the blast source. The varying level of confinements, described in Table 2.2 and illustrated in Figure 2.8, can overlap depending on the height of the detonation and SOD.

Table 2.2 *Table listing the different classifications of confinement for a blast according to the UFC 3-340-02 design manual[43].*

Free Air Burst:	**Air Burst:**	**Surface Blast:**
Charge is detonated a distance from the target.	Detonation is at a distance from and above the target surface.	Charge is detonated close to reflective surface.
Blast wave reaches target without prior disruption.	Reflection of incident wave occurs before impacting the target surface.	The incident wave is reflected and amplified at the point of detonation.

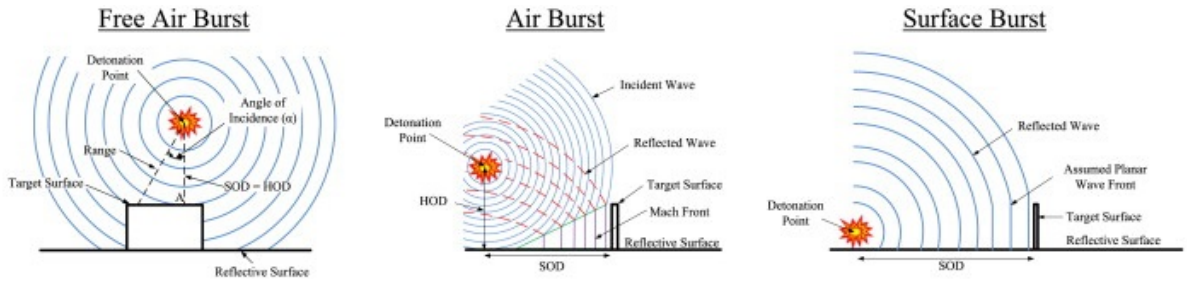

Figure 2.8 Illustration depicting the varying levels of unconfined blasts. [44].

2.2.8.1 Confined Blast Loading

A confined blast refers to an explosion that occurs within a fully or partially enclosed structure [42, 43]. Edri *et al.* [45] established that confined blasts resulted in more damage to a target structure than an unconfined blast of the same mass of explosive. Various geometrical parameters of the container such as the shape and size of the container, the vents present and the charge location and size will affect the magnitude of the resulting blast wave [43, 42, 45].

For partially confined blasts, limited size openings are available with the detonation enclosed. The initial wave, amplified by the pressure waves reflecting off structure, can be vented to the atmosphere after a period of time. The products of the detonation are also able to escape after a period of time. A quasi-static pressure is built up after the blast due to the presence of the detonation products, namely the high temperatures and gaseous products. This pressure has a long duration in comparison to the pressure provided by the initial blast wave[43].

For fully confined blasts, the explosion is either totally or at near total confinement. The blast load will consist of an un-vented shock load with a very long-duration gas pressure load which are a function of the containment. Very little pressure from the blast wave will escape the containment vessel [43]. Varying levels of confinement have been defined and described in Figure 2.9 and Table 2.3.

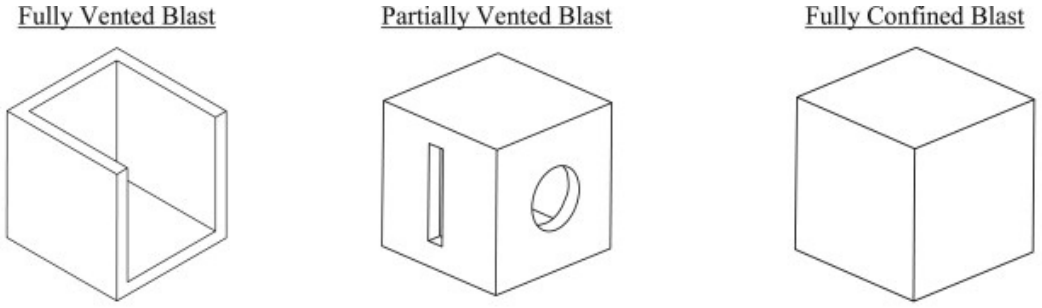

Figure 2.9 Illustration depicting the varying levels of confined blasts. [44].

Table 2.3 *Table listing the varying levels of confinement [44].*

Fully Vented Blast	**Partially Vented Blast**	**Fully Confined Balst**
Detonation points occurs next to some form of barrier or in a structure that has one or more sides open to the atmosphere.	Detonation occurs in a structure with limited openings/vents.	Detonation occurs within a structure that fully or nearly fully contains the effects of the explosion.
The structure is unable to contain the gas pressure.	The duration of the gas pressure is finite and is proportional to the size/area of the vents.	The blast loading comprises of repetitive shock loads and a long duration pressure loading due to the interaction of the blast waves at the boundaries and joint interfaces.

Karpp *et al.*[46] studied the response of thin walled containment vessels to blast loading experimentally, computationally and analytically. The waves reflective behaviour off the containment vessels was shown to interact with other waves. Figure 2.10, [46], shows the arrival of the second major loading pulse on the pressure vessel, as well as subsequent pressure peaks. Within each pulse, a double peak pressure is apparent. This is caused by the wave reflections from the vessel walls. The shock wave causes the second pulse to

rebound between the interface and the wall but the additional pressure pulses caused by the reflections after this are negligible.

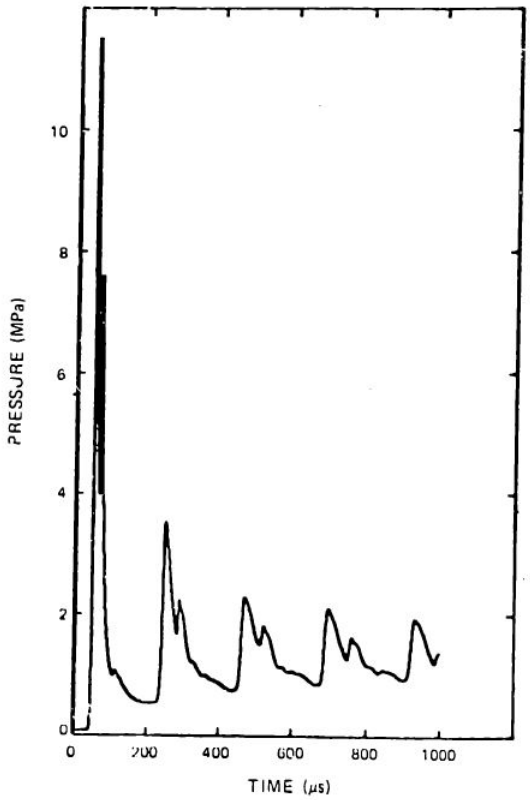

Figure 2.10 Graph showing the initial pressure wave peak with a reflective wave against the container wall [46].

2.3 The response of metal targets to blast loading

Numerous studies have been performed to examine the response of steel plates to blast loading. Aspects of past research will be discussed, including the deformation of target plates, materials used as well as charge shape and size.

Plastic deformation of target plates from air blast and impulsive loads has received a lot of attention in previous years [47, 48, 49]. Teeling-Smith and Nurick [50] were the first to document the deflection failure modes in circular plates exposed to uniform blast loads. Mode I was defined as large plastic deformation, mode II as tensile tearing at the boundary and mode III as transverse shear failure at the boundary. Jacobs *et al.* [51] investigated the effects of stand-off distance on failure of fully clamped circular

plates in partially confined structures. It was reported that as the stand off distance changed, the characteristics of the deformed plate profile changed as well. For greater stand of distances, the plate profile resembled a uniform dome as displayed in Figure 2.11, characterised by a global uniform dome as reported by Teeling-Smith and Nurick [50].

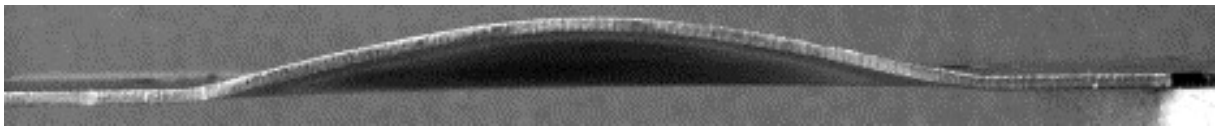

Figure 2.11 Photograph showing the blast profile of a target plate when exposed to a uniform blast load [51].

For closer stand-off distances, the plate profile is characterised by a smaller dome atop a global dome, as displayed in 2.12. Typical of localized loading conditions at the centre of the plate.

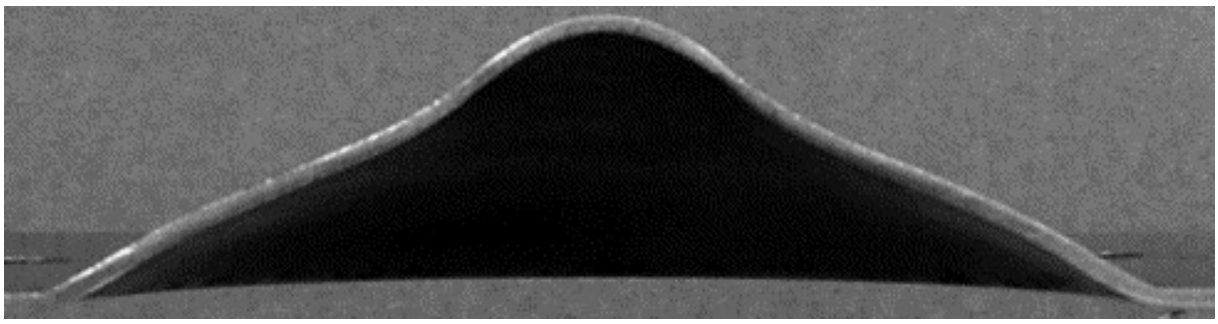

Figure 2.12 Photograph showing the blast profile of a target plate when exposed to a localised blast load [51].

Nurick *et al.* [52] also conducted an experimental study to investigate the onset of necking and subsequent tearing at the boundary of a clamped circular plate. The results indicated that the occurrence of thinning and rupture was highly dependent on the boundary conditions. For sharp edges at the boundary conditions, the plate at the boundary took on a sharp indent due to the clamp, before stretching and thinning occurred. The necking for curved edge boundaries presented necking similar to that in uni-axial tensile tests.

A non-dimensional investigative approach used by Nurick and Martin [53] to determine an empirical formula for displacement ratio vs non-dimensional impulse for plates

subjected to impulsive loading, is demonstrated in Figure 2.13. This was later revisited and validated by Chung Kim Yuen *et al.* [54] who performed a review of several papers on the deformation of thin steel plates subjected to impulsive air-blast loading. The data from the experiments was compared on a graph where the midpoint deflection thickness ratio for circular plates, δ/t, was compared to a dimensionless impulse, ϕ_{cs} as can be observed in Figure 2.13 and is described mathematically in Equation 2.19. The non-dimensional quantities allowed for analysis of many shaped target plates and charges sizes to be compared.

$$\delta/t = 0.427\phi_{cs} + 0.298 \tag{2.19}$$

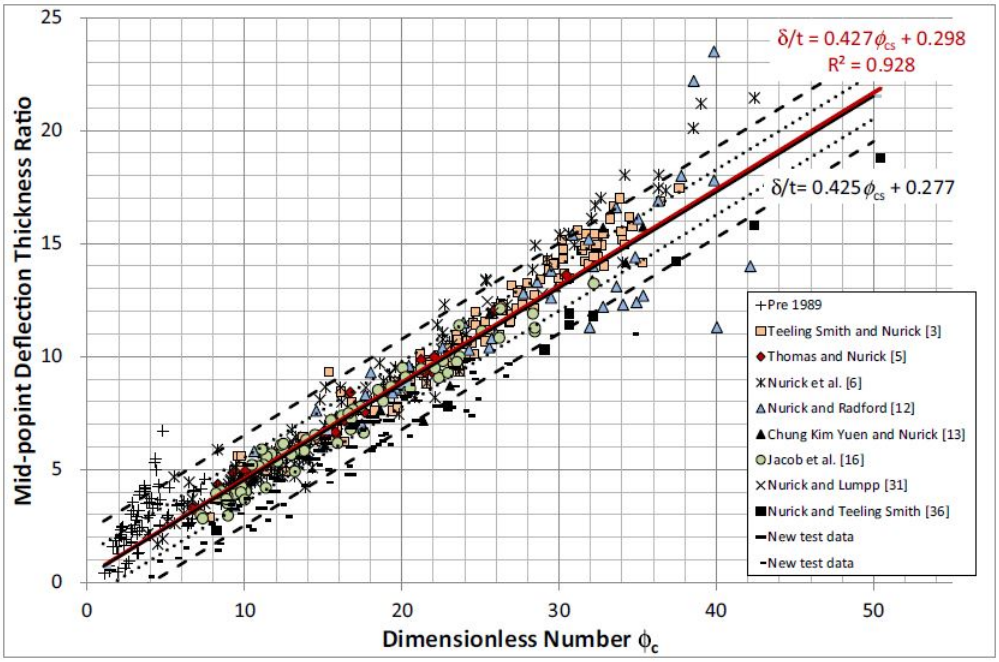

Figure 2.13 Graph highlighting the displacement ratio vs non-dimensional impulse for circular plates [54].

Mehreganian *et al.* [55] studied the response of mild and armour steel and recorded the response of the steel to air blasting. The steel panels were exposed to an air blast loading induced via the detonation of a circular disk of PE4 plastic explosive at a predetermined stand-off distance. The PE4 was detonated in the middle of the panel and was held in place with a polystyrene bridge arrangement. Both steel-type plates underwent rupture with

similar charge sizes and stand-off distances. The stronger armour plating did experience less deflection. Mehreganian *et al.* [55] also reported that an increase in the thickness of the plate increases the ratio of the transmitted impulse to the total impulse on a rigid target.

Nurick *et al.*[56, 57, 58] investigated the response of metal plates to cylindrical charges. From the experiments, the impulse versus charge mass for cylindrical charges with varying dimensions was recorded and is presented in Figure 2.14. A strong linear relation between charge mass and impulse delivered from a blast was also observed.

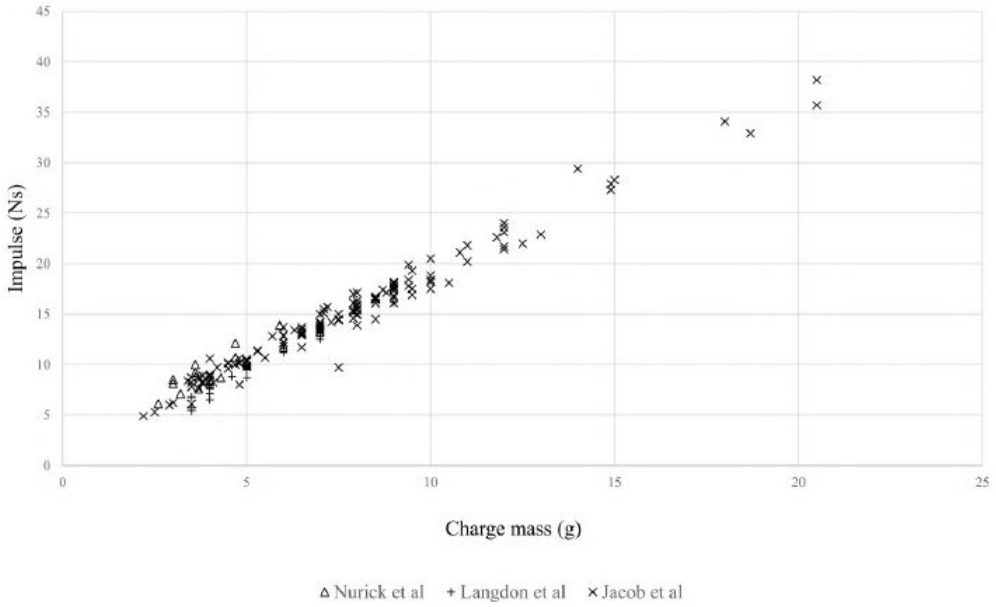

Figure 2.14 Graph of axial impulse versus charge mass via the use of a ballistic pendulum. Data captured by [56, 57, 58].

Nurick *et al.* [58] also studied the relation between the charge diameter to length ratio against impulse. The effect of the shape of the explosive is illustrated in Figure 2.15. As shown by the data, charges of the same mass but with a wider diameter produced a larger blast impulse.

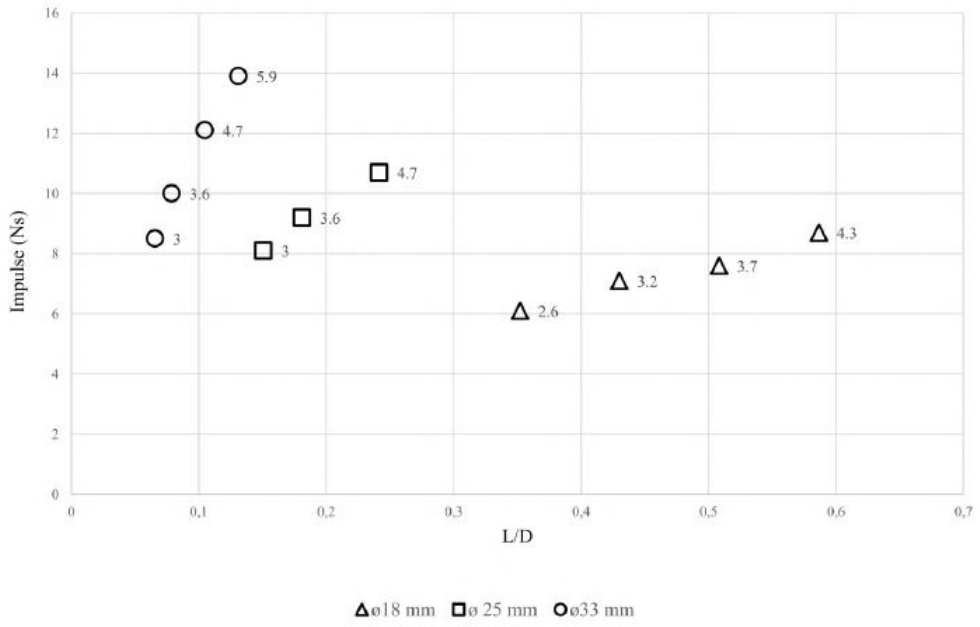

Figure 2.15 Graph showing the impulse delivered from charges with varying aspect ratios. Data captured by Nurick *et al.*[58].

The findings by Nurick *et al.* [58] related to the wave propagation within the explosive charge. Nurick *et al.* [58] used the ZND one-dimensional model to investigate the pressure profile with varying charge geometries including the charge shapes. The shapes used were cylindrical charges (CY) , inverted truncated cone charges (ITC) and truncated cone charges (TC) . A spherical shock wave was assumed, rather than a plane wave, to realistically predict the loading distribution and the profile of the pressure wave. Figure 2.16 shows a schematic of the detonation process in the cylindrical shape, and the blast wave propagation through the charge, with the initial wave staring at a point and the wave spreading through the charge in a circular nature away from the detonation point with time. Due to the circular wave front, the wave reached the edge of the charge where the distance was shortest first. The nature of the blast front detonation meant the corners of the cylindrical charge would detonate last and not in a uniform form.

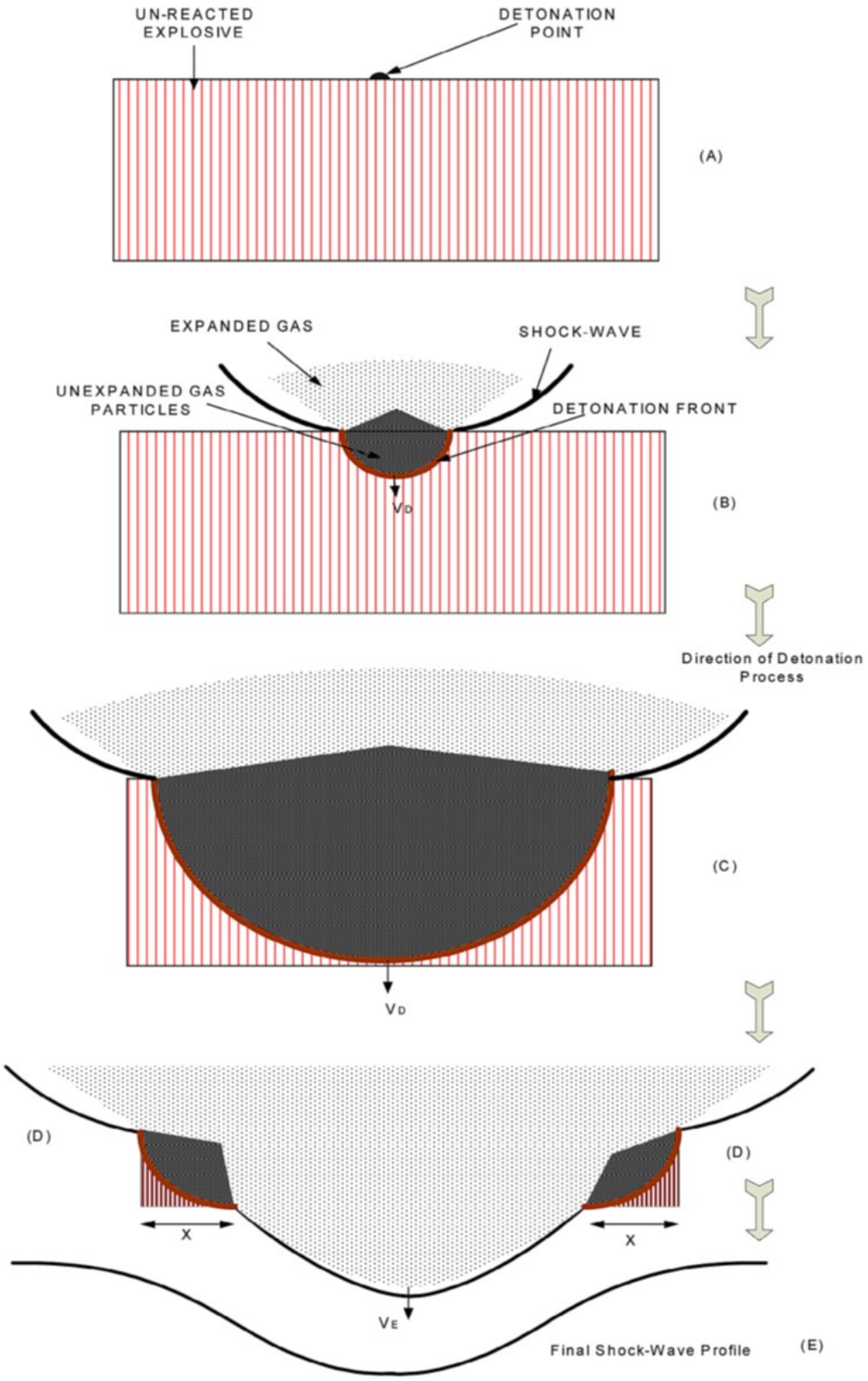

Figure 2.16 Schematic of the detonation process in CY shape explosive, according to the ZND model *et al.*[58].

2.3.1 Numerical Solvers used to Model Blast Loading

The numerical simulation approach and various different models created are reviewed in this section.

2.3.1.1 Solvers used within Numerical Investigations

Two solvers commonly used in numerical investigations are the Lagrangian and Eulerian solvers. Both solvers have an initially defined grid placed over the domain, mapping geometry and defining material properties in each grid. But material motion and grid evolution is handled differently for the Lagrangian or Eulerian approach.

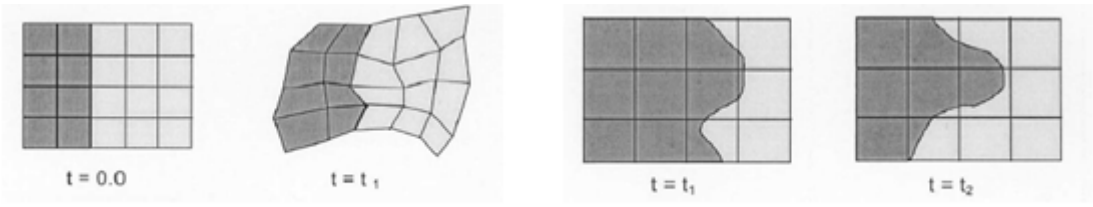

Figure 2.17 Schematic illustrating the different solvers in AUTODYN. The left-hand side is the Lagrangian solver, and the right-hand side is the Eulerian solver [59].

With the Lagrangian solver, the numerical mesh that is placed over the material moves with the material flow velocity and distortions. The material does not transport from one element within the mesh to the other [59, 60]. The disadvantage of the Lagrangian system is that the mesh distorts substantially with large material movements. Euler representations allow materials to flow from cell to cell while the mesh is fixed. Euler is useful to model gases, fluids and large structural deformations [60, 59]. For Euler-Lagrangian, finite-difference equations are solved in a two-step numerical procedure. The first step is the Lagrangian step, where the mesh follows the material. The second step is when the solution is mapped from the deformed mesh back onto the initial mesh, which is spatially fixed [59]. Both solvers are represented in Figure 2.17.

2.3.1.2 Brief Review of the Various Solvers and Models used in the Previous Studies

The response of metal targets to blast loading in numerical simulations has been extensively reported, for example [55, 61, 62, 63, 64, 65]. Flis [62] modelled the acceleration of metal linings using a Lagrangian approach. Fairlie [63] described how two and three-dimensional numerical analysis tools were applied to the simulations of high explosives while using hydro code in AUTODYN modelling software. Both Lagrangian and Eulerian solvers were incorporated into an Arbitrary Lagrange Euler (ALE) processor . Slavik [64] used another modelling software, LS-DYNA, to present the coupling of Empirical Explosive Blast Loads to ALE Air Domains in the respective software. Tabatabaei and Volz[65] used LS-DYNA to compare the three different blast methods present in the software, namely the Load Blast Enhanced (LBE) method, Multi-Material-Arbitrary Lagrange Euler, (MM-ALE) and coupling of the LBE and MM-ALE methods. The computational work conducted by Fairlie [63] described previous case studies successfully and reported that the numerical work is best used when conducted with experimental work. Tabatabaei and Volz[65] reported that the coupled method produced similar results to the ALE while using less simulation time.

2.3.2 AUTODYN

AUTODYN is a computer simulation tool that is suited for modelling explosion, penetration and impact events by simultaneously solving the conservation of mass, momentum and energy equations on couples Eulerian and Lagrangian meshes [66]. The numerical model was developed using AUTODYN, to predict how shrapnel, modelled as a ball bearing would interact with a target plate when placed at different depths within a cylindrical charge. The effects of charge mass were also investigated.

2.3.2.1 Equations needed for modelling the detonation

Explosions are numerically described by a system of differential equations. These consist of the fundamental laws of conservation of mass, momentum and energy, as well as other

supplementary equations of modelling [59]. Tables of the equations that were used in AUTODYN are shown in Table 2.4 and Table 2.5, with equations for both Lagrangian and Eulerian listed.

Table 2.4 *Table listing the supplementary Equations for Conservation for AUTODYN. Source adapted from [59].*

Law of Conservation	**LaGrangian**	**Eulerian**
Mass	$\frac{d\rho}{dt} + \rho\frac{\delta v_i}{\delta x_i} = 0$	$\frac{\delta\rho}{\delta t} + \frac{\delta(\rho v_i)}{\delta x_i} = 0$
Momentum	$\frac{dv_i}{dt} = f_i + \frac{1}{\rho}\frac{\delta\sigma_{ij}}{\delta x_j}$	$\frac{dv_i}{dt} + v_j\frac{\delta v_i}{x_j} = f_i + \frac{1}{\rho}\frac{\delta\sigma_{ij}}{\delta x_j}$
Energy	$\frac{dE}{dt} = -\frac{p}{\rho}\frac{\delta v_i}{\delta x_i} + \frac{1}{\rho}s_{ij}\varepsilon_{ij}$	$\frac{\delta E}{\delta t} + v_j\frac{\delta E}{\delta x_i} =$ $-\frac{p}{\rho^2}(\frac{\delta v_i}{\delta x_i} + v_i\frac{\delta\rho}{\delta x_j}) + \frac{1}{\rho}s_{ij}\varepsilon_{ij}$

Table 2.5 *Table listing the supplementary Equations for Modelling for AUTODYN. Source adapted from [59].*

Stress Tensor	$\sigma_{ij} = -(p+q) + s_{ij}$
Equation of State	$p = f(\rho, e)$
Constitutive Model	$\sigma_{ij} = g(\varepsilon_{ij}, \dot{\varepsilon_{ij}}, E, D)$
Explosion	$h(p, \rho, v, T, x, t) = 0$

Where ρ is density, t is time, v is velocity, x is displacement, σ is stress, E is internal energy, p is hydrostatic pressure, s is deviatoric stress, ε is strain and q is pseudo-viscous pressure.

Building on these basic equations that define interactions, the equations that determine the materials response are modelled. The aspects the equations describe are the equation of state, the strength of the material and the failure model. The failure model is included to account for the material if the stresses exceeds the materials strength limit. Other features such as boundary conditions, gauges and interaction points were also added [59].

2.4 Response of metal targets to projectiles

The response of targets to projectile impacts has been studied extensively. The first 150 years focused on the degree of penetration of targets struck under different conditions and different initial velocities as reported by Robins and Euler [67, 68].

2.4.1 Ideal projectile impacts

The ideal collision conditions of a normal impact of a purely translating projectile against a stationary object have been assumed in many investigations [69]. A summary of the subject up to 1977 was presented by Backman and Goldsmith *et al.* [70]. Many terms and definitions, such as the target classification and velocity range classifications, shown in Tables 2.6 and 2.7, were defined in this paper.

Table 2.6 *Table listing the Target plate classification [70].*

Target plate classification.	
Name	**Target classification**
Thin	$h/D < 1$
Intermediate	$1 < h/D < 10$
Semi-infinite	$10 < h/D$

Table 2.7 *Table listing the velocity range classifications [70].*

Velocity range classifications	
Name	**Velocity Classification**
Subordnance	$v_o < 500m/s$
Ordnance	$500m/s < v_o < 1500m/s$
Ultraordnance	$1500m/s < v_o < 3000m/s$
Hypervelocity	$3000m/s < v_o$

Where h is the target thickness, D is the shank diameter and v_o is the initial velocity of the projectile.

These ideal impacts only occur in a laboratory. In a real-life application, targets are very seldom at a normal to the projectile trajectory, the target is often moving and the projectile might be fired from a moving source [69].

Nishida *et al.* [71] examined the effects of the crater diameter and impact velocity on length distribution of fragments. A spherical projectile made of aluminum alloy 2017-T4 with varying diameters was fired at thick targets made of aluminium alloy 6061-T6 at varying velocities. It was reported that the craters were almost spherical in shape and that crater volume was directly proportional to the kinetic energy of projectiles when the spherical projectiles struck with high enough velocities. The typical crater deformation is illustrated in Figure 2.18.

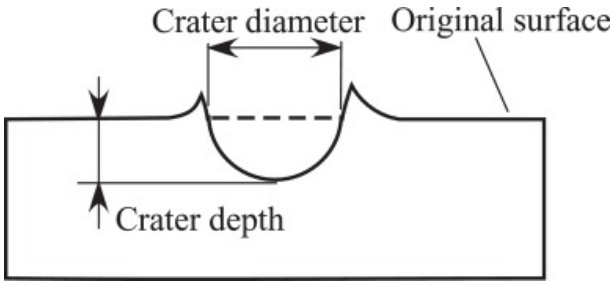

Figure 2.18 Schematic illustrating the typical deflection observed when firing a spherical projectile at a target plate. [71].

2.5 Response of metal plates to combined blast and fragment loading

The response of a structure to a combined blast and fragment load is complicated as discussed by Nystrom *et al.* [72]. For combined loading events, it is difficult to analyse the combination of the different loading events. Nystrom and Gylltoft [72] used a numerical simulation tool, supported by experimental data, to further study the combined blast and fragment loading effect on of reinforced concrete walls exposed to blast loading from a bomb (50% TNT by weight) and spherical fragments of the same size. The damage caused

by combined loading was greater than the sum of the loads when acting separately. This was determined by measuring the maximum deflection experienced by the concrete wall, modelled as a concrete strip, in the numerical model. This is illustrated in Figure 2.19, as shown by Nystrom *et al.* [72] and Marchand *et al.* [73].

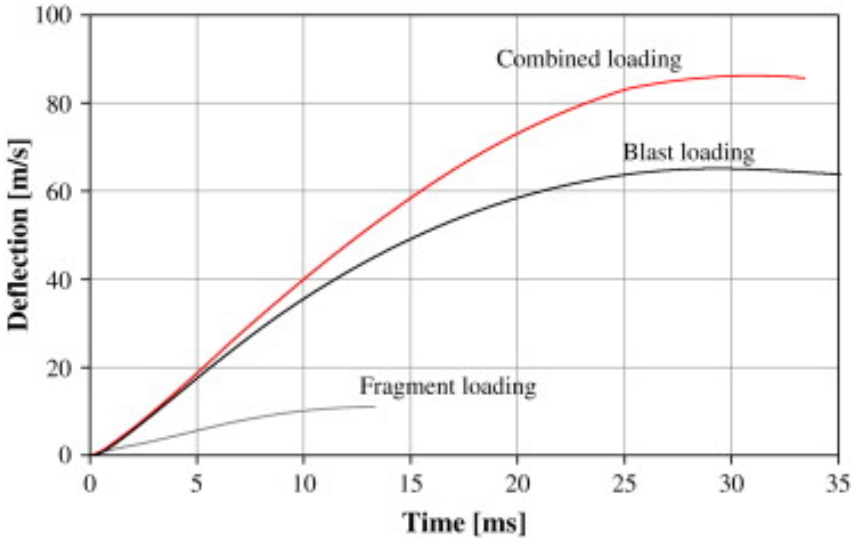

Figure 2.19 Graph depicting the difference in the deflection of a target between coupled and uncoupled loading in blast events. [72].

Qi *et al.* [61] investigated the influence of charge geometry on the velocity of a ball bearing placed at the front face of a cylindrical explosive charge. It was found that for a constant charge diameter, the ball bearing velocity increased in a near logarithmic manner until a critical length of the charge ($\frac{\sqrt{3}}{2}$ larger than the diameter). Beyond this critical length there was no significant change observed in the impact velocity of the ball bearing. Qi *et al.* [61] also reported that for a constant charge mass, the ball bearing velocity decreased as the charge diameter increased.

Kang [21] carried out a study investigating the crater distribution and resulting crater depth caused by detonating a cylindrical charge surrounded by ball bearing in a cylindrical container. The findings indicated that the maximum ball bearing velocity occurred when the ball bearing was placed just beneath the surface of the charge. Little emphasis was made to identify a relationship between the deflection of a target plate to the depth of a ball bearing within a charge.

2.5.1 The velocity of explosive propelled foreign objects

IEDs commonly have foreign objects placed in the explosive to increase harm and injury to civilians and military personnel nearby. One of the most common foreign objects used would be a form of shrapnel, be that ball bearings, nails or glass [2].

Gurney [74] also developed an equation to define the velocity of an object driven from a blast. Gurney developed a one-dimensional model that estimated the initial velocity of fragments that were propelled from a blast. For metal expelled from a cylindrical charge, the initial velocity was expressed as,

$$V = \sqrt{2E}(\frac{C}{M + \frac{C}{2}})^{\frac{1}{2}} \tag{2.20}$$

Where C is the mass of the explosive, M is the mass of the plate, $\sqrt{2E}$ is Gurney's velocity and was found using standardised cylinder tests.

Held [75] reported that a charge configuration shaped like a disc with annular confinement produced repeatable fragment velocities. Choudha *et al.* [76] used the model developed by Held [75] to perform a parametric study on a single confined fragment launch device, depicted in Figure 2.20, to determine an empirical relationship between the effect of fragment size, charge size, and casing thickness on fragment velocity. When increasing the confinement thickness and charge quantity and decreasing the fragment height, the fragment velocity increased. The charge-to-metal mass ratio under the fragment significantly affected the velocity of the fragments. Choudha *et al.* [76] found an empirical formula based on fragment size, charge size and confinement thickness as shown in Equation 2.21.

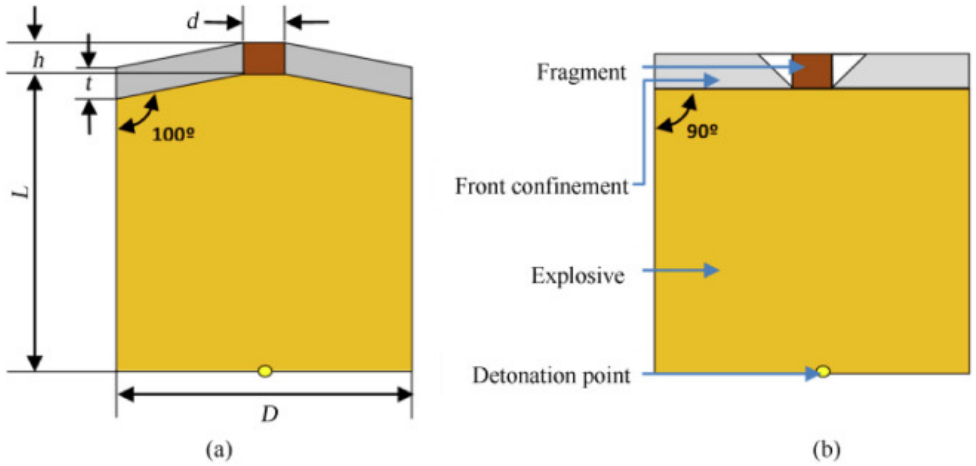

Figure 2.20 Schematic showing a simplified single confined fragment launch device for the parametric study. [76].

$$V = b_1 + b_2(\frac{L}{D}) + b_3(\frac{h}{d}) + b_4 R_f + b_5 e^{\frac{L}{D}} + b_6 e^{\frac{h}{d}} + b_7 e^{-R_f} + b_8 R_c(\sqrt{\frac{d}{h}}) + b_9 e^{-R_c} \quad (2.21)$$

Where V is velocity, b_1 = 774.925, b_2 = -383.477, b_3 = 78.474, b_4 = 322.797, b_5 = 690.826, b_6 = 490.180, b_7 = -1383.163, b_8 = -33.963, b_9 = 0.000187, $R_f = (\frac{h}{L})(\frac{p_f}{p_e})$ and $R_c = (\frac{t}{L})(\frac{p_f}{p_e})$, L is the charge length in mm, D is the charge diameter in mm, h is the fragment height in mm, d is the fragment diameter in mm, t is the confinement thickness, p_f is the fragment density and p_e is the explosive density.

Grisaro and Dancygier [77] performed a numerical study that showed the Gurney formula for a cylindrical charge predicted the velocity to a higher degree of accuracy when the charges had a high length-to-diameter ratio. Charges that had a ratio of ten achieved the predicted Gurney velocity, while charges that had a ratio of 0.5 only achieved a velocity that was 67% of the Gurney velocity. This can be observed in Figure 2.21, where the greater the length-to-diameter ratio, the closer the ratio of casing velocity gets to achieving 100% of the Gurney velocity.

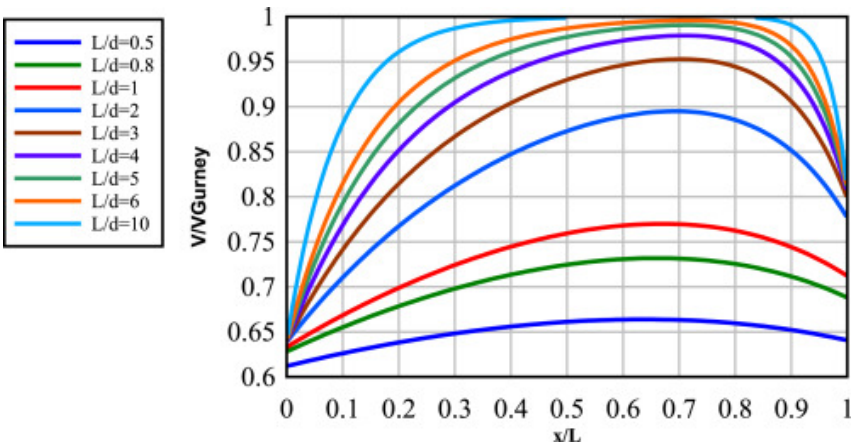

Figure 2.21 Graph illustrating the casing velocity to Gurney velocity, dependent on the length-to-diameter ratio of the cylindrical charge [77].

2.5.2 Time of arrival

For combined blast and fragment load on a structure, the time of arrival of the pressure wave and fragment affects the response of the structure. The difference in time of arrival of the blast and fragment can be significant. Grisaro and Dancygier [78] stated that a blast wave can have an initial velocity in the range from 2-10km/s while the initial velocity of the fragment can vary from 1.5-2.5km/s for the same set-up. The deceleration of a blast wave was also found to be greater when compared to the fragments deceleration implying that within a short distance, the blast wave would impact the target before the fragment. However, as the distance increased the fragment was more likely to impact the target before the blast wave as illustrated graphically in Figure 2.22. Figure 2.22 illustrates an example to compare the arrival time of a blast wave compared to a fragment for various distances calculated according to the CONWEP [79] for a 250kg general purpose bomb with 50 weight per cent TNT. From Figure 2.22, it is suggested that the blast and fragments arrived at the same time at approximately 5m from the source.

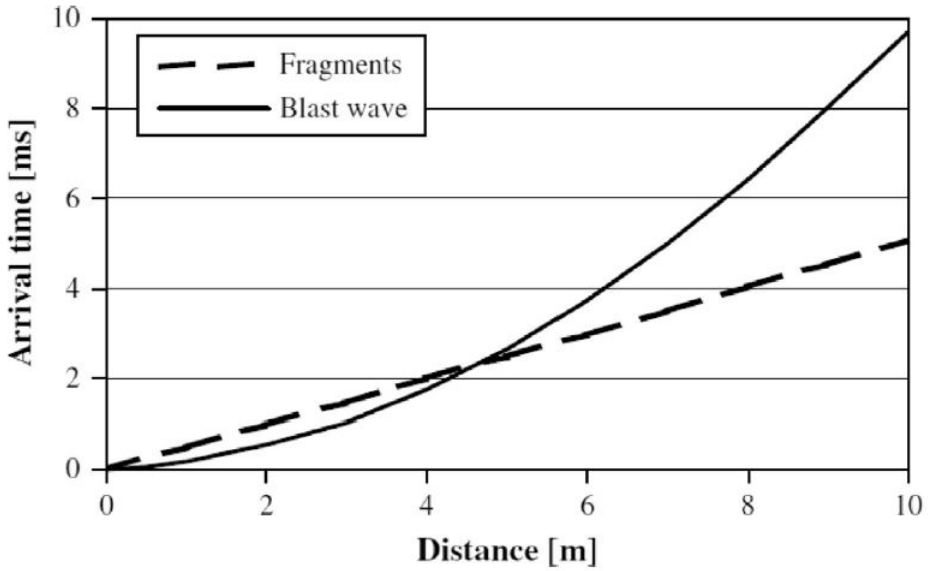

Figure 2.22 Graph comparing the arrival times of blast and fragments for 250-kg charge filled with 50% TNT [80].

2.5.3 Outcome of Literature Review

Based on previous literature on blast pressure waves and theories, it was reported that explosive charge geometry played an important role in blast pressure magnitude and wave front over short stand-off distances. When a blast was confined, the reflected pressure could cause greater pressure to be experienced by the target plate, along with a double wave feature in the pressure to time history profile.

For blast driven projectiles, the Gurney equation had a higher degree of accuracy when the length-to-diameter ratio was greater, but were only accurate in simple detonation theory research projects. For combined loading events held at short distances, or when the target plate experienced localised loading, the blast wave would arrive at the target before the blast driven fragment.

In previous literature, little emphasis was made to identify a relationship between the deflection of a target plate to the depth of a ball bearing within a cylindrical charge. This dissertation presents the results of a study that investigated the influence of the placement of a ball bearing along the axis within a rear-detonated cylindrical charge by decoupling the loading to understand the contribution of each loading condition from an overall response perspective.

Chapter 3

Experimental Procedure

The experimental set up as well as the experimental procedure used for this project are presented in this chapter. Three different kind of experiments were carried out to unpack the contribution of the fragment and blast load to the deflection of the target plate. Projectile impact tests using a two stage gas gun were performed to relate impact velocity and the resulting target plate deflection. Blast tests were performed to examine the effects of blast loading on a target plate. The tests were carried out to examine the effect of two uncoupled contributions of combined blast and fragment loading. Blast tests using embedded ball bearings along the cylindrical axis of the charge were performed to investigate the combined loading effect.

3.1 Material Used (Domex 700)

Domex 700, a hot rolled, high strength, cold forming steel was used as the material for the different target plates. Dog bone specimens were cut from the same two sheets that the target plates were cut from. The drawings of the specimens can be viewed in Appendix C. The specimens were exposed to three cross head speeds in a tensile tester, namely $2mm/min$ ($0.0004s^{-}1$), $20mm/min$ ($0.0044s^{-}1$) and $200mm/min$ ($0.0444s^{-}1$). Three samples from each sheet were used for each speed to ensure repeatability. From these tests, the material properties were determined.

3.1.1 Tensile Test Results

The tensile tests conducted to determine the material properties of Domex 700 were consistent with each other and favourable when compared to previous studies [81]. Figure 3.1 illustrates the typical stress strain graphs for the various cross head speeds.

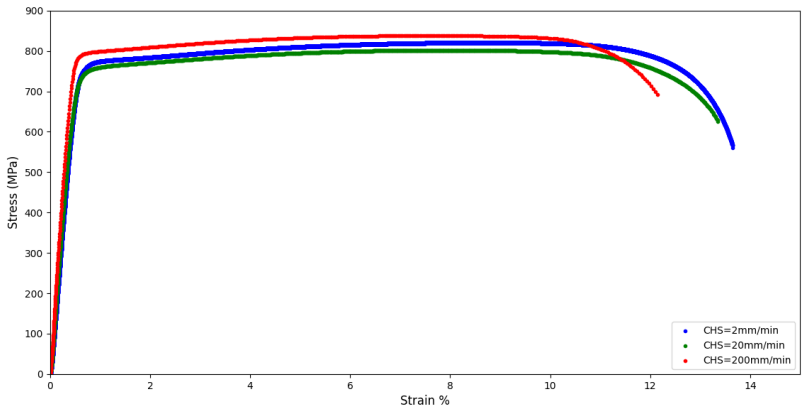

Figure 3.1 Graph of the results from three of the tensile tests for three different cross head speeds.

From the tensile tests, the material properties were determined. The values are listed in Table 3.1.

Name	Value	Units
Yield Stress	746	MPa
Ultimate Tensile Stress	807	MPa
Strain at Failure	12.7	%

Table 3.1 *Table listing the mechanical properties of Domex 700 gathered from the tensile tests.*

The thermal properties of m and t_{melt} are approximated to those of hardened Steel 4340 as done by Chung Kim Yuen et al. [82] and Pickering [81].

3.2 Projectile Impact Test using a Ball bearing

Projectile impact tests were carried out using a two stage gun, with air for all stages, with a $5mm$ martensitic stainless steel AISI 420C (X46Cr13) ball bearing to relate impact velocities with resulting target plate deflections. The experimental arrangement used for the impact test is depicted in Figure 3.3. The projectile tests were performed within a box made out of steel plates that had 2 side wall windows covered with polycarbonate to allow for the capture of the flight of the projectile. A large tube filled with wax was placed at the back to catch the ball bearing should it penetrate the target plate. The barrel of the two-stage gas gun protruded through the front wall of the box with a tight fitting 3D printed casing to ensure no projectiles rebounded out the box.

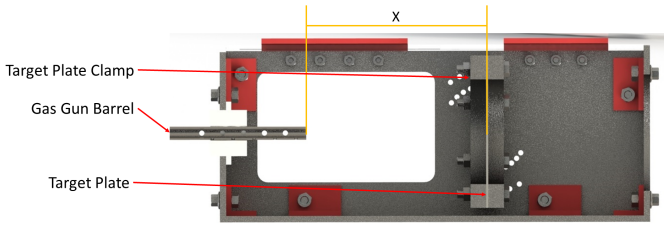

(a) CAD sectional model of the general set up used to conduct impact testing.

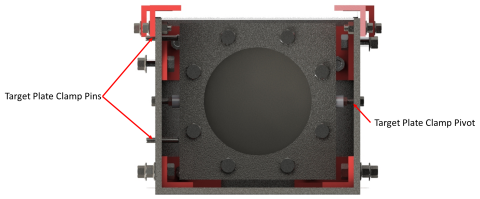

(b) CAD sectional model showing the clamp mounting design.

Figure 3.2 CAD sectional views of the assembly box used for the projectile tests.

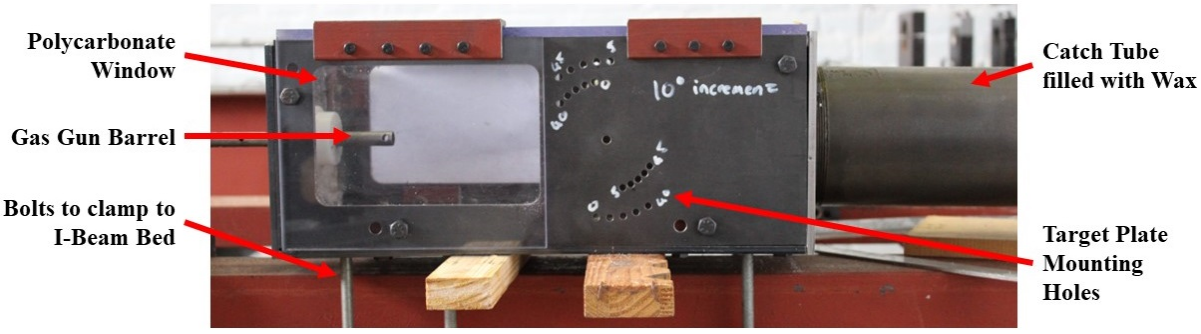

Figure 3.3 Photograph depicting the various components in the projectile box assembly.

The target plates were cut from DOMEX 700 steel sheets. The target plate, as displayed in Figure 3.4a, was square in shape with a circular exposed area when clamped as depicted in Figure 3.4b. The clamped target plate was then mounted onto the box with pins so that it was vertical to allow for a projectile to strike the target plate in the normal direction, as displayed in Figure 3.2. The mounting method can be viewed graphically in Figure 3.2b, and a sectional view of the full box assembly can be viewed in 3.2a.

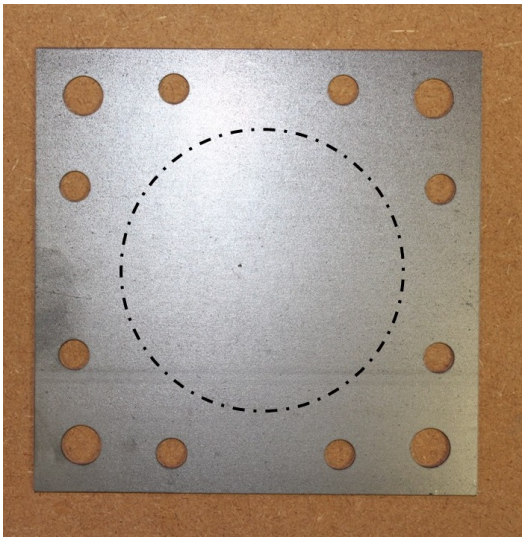

(a) Photograph of the Domex 700 target plate with the exposed area circled.

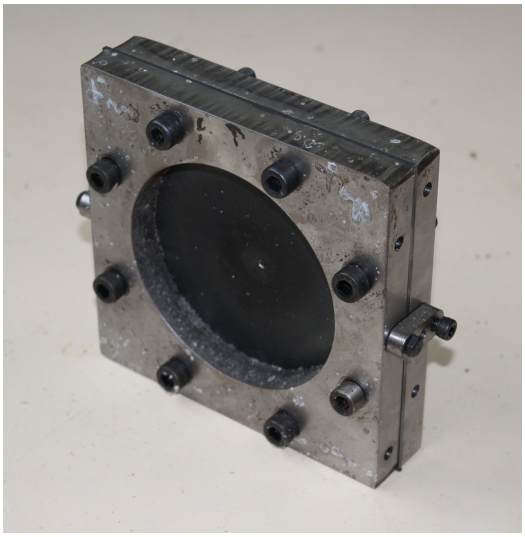

(b) Photograph of the steel clamps used to hold the target plate.

Figure 3.4 Photographs of the clamp and plate used to capture the deflection from only a ball bearing impact load.

The full assembly test box was placed onto an I-Beam aligned with the two-stage gas gun. Both the gas gun and box were fastened to the bed to ensure minimal movement when firing took place. A Phantom VEO 710L with a 1 MP sensor high speed camera, used to determine the impact velocity of the projectile, was placed to the side of the box with lighting on either side. The high speed camera captured the impact tests at a frame rate of 63000 frames per second.

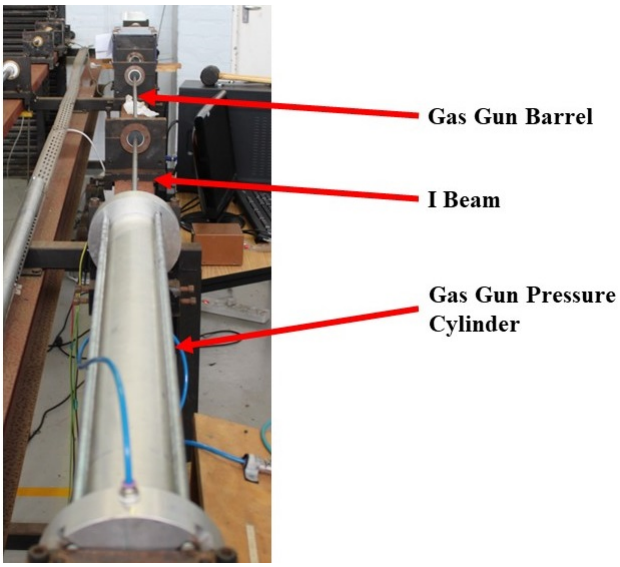

Figure 3.5 Photograph showing the two stage gas gun and projectile box on the I beam.

A wax sabot, as depicted in Figure 3.6, was used to locate the ball bearing and to ensure a tight fit in the barrel allowing for a greater build up of pressure, and therefore a higher impact velocity. The sabots with the mounted ball bearing, were placed down the barrel. Once the appropriate pressure was reached, the gas gun was fired. As the sabot travelled down the length of the barrel, the sabot experienced a greater friction and consequently allowing the ball bearing to separate from the wax sabot before impacting the target plate. Thus allowing only the ball bearing to impact the target plate.

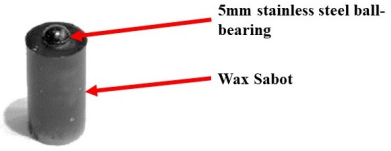

Figure 3.6 Photograph of the wax sabot, highlighting the location of the ball bearing in wax cylinder.

Prior to testing, the camera pixel-to-distance ratio was calibrated by placing a ruler on the barrel in the focal plane of the camera (the plane in which the bearing travelled)

Figure 3.7. The relationship between pixel and distance could be determined in the camera software, Figure 3.7, and used to track the ball bearings impact velocity.

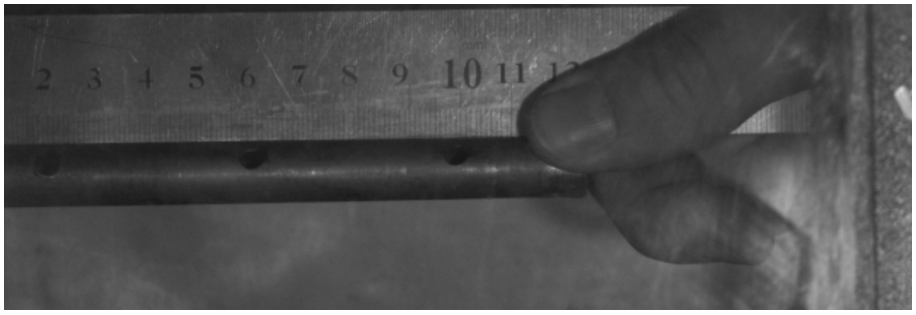

Figure 3.7 Photograph taken when calibrating the pixel-to-distance ratio on the high-speed camera.

Stills were taken from the high-speed camera footage to track the location of the ball bearing during testing. A black circle of best fit was placed around the ball bearing, as shown in Figure 3.8 to track the location of the ball bearing. The circle allowed for a more accurate reading of the location of the ball bearing.

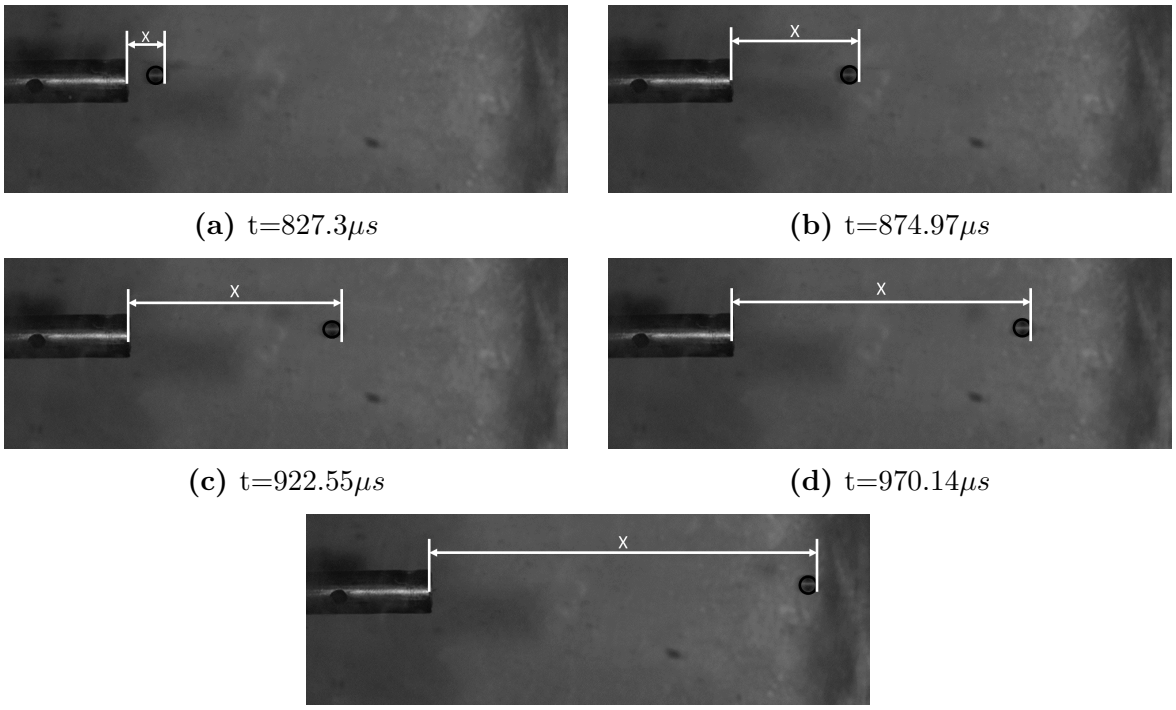

(a) t=827.3μs **(b)** t=874.97μs

(c) t=922.55μs **(d)** t=970.14μs

(e) t=1017.7μs

Figure 3.8 Photographs from the high speed camera capturing the flight of the ball bearing from experiment 7.29.3.

The average velocity for the ball bearing was calculated using the displacement and time relationship in Equation 3.1.

$$v = \frac{x_2 - x_1}{t_2 - t_1} \tag{3.1}$$

Where x_2 and t_2 is the current frames displacement and time respectively and x_1 and t_1 is the previous frames displacement and time respectively. There was no significant change in the velocity of the ball bearing irrespective of which frames were used to measure the ball bearing velocity, indicating the velocity of the ball bearing was constant and that the velocity measured from the high speed camera was the impact velocity the target plate experienced.

3.3 Blast Loading Experiments

Four series of blast loading tests were conducted. These were:

- Blast loading on complete specimen.
- Blast loading on Pre-cut target plate.
- Combined loading (charge with embedded ball bearing)
- Blast driven ball bearing average velocity tests

The Domex 700 target plates were placed in a blast rig on a pendulum and exposed to the different blast loading conditions to determine how the various loads and charge affected the response of the plate. The charges were made from Plastic Explosive 4 (PE4) that were consistently cylindrical in shape with a $20mm$ diameter.

3.3.1 The General Arrangement for Blast Loading Tests

The experimental blast rig, shown in Figure 3.9, consisted of a target plate, shown in Figure 3.10, clamped between two steel plates with 8 bolts. The target plate was $350mm$ x $350mm$, and $2mm$ thick. The blast plate had a circular area with a diameter of $200mm$ exposed to the blast. A blast tube was used to guide the blast wave and to create a set stand off distance of $150mm$.

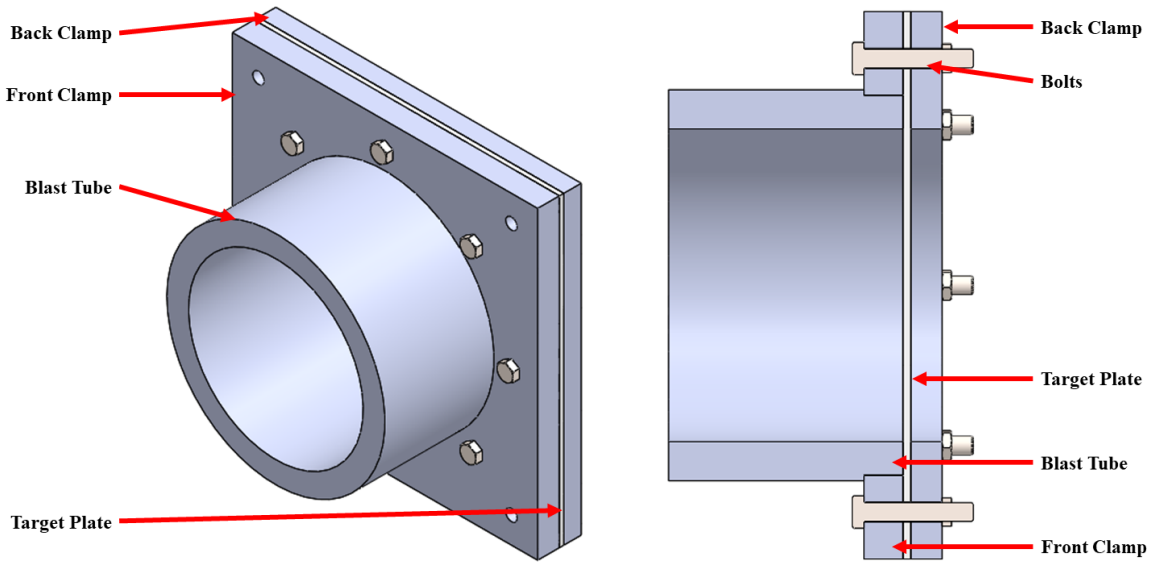

(a) Isometric CAD model view of the clamp designed to hold the target plate in place.

(b) Sectional CAD view of the clamp designed to hold the target plate in place.

Figure 3.9 CAD model views of the clamp designed to hold the target plate in place.

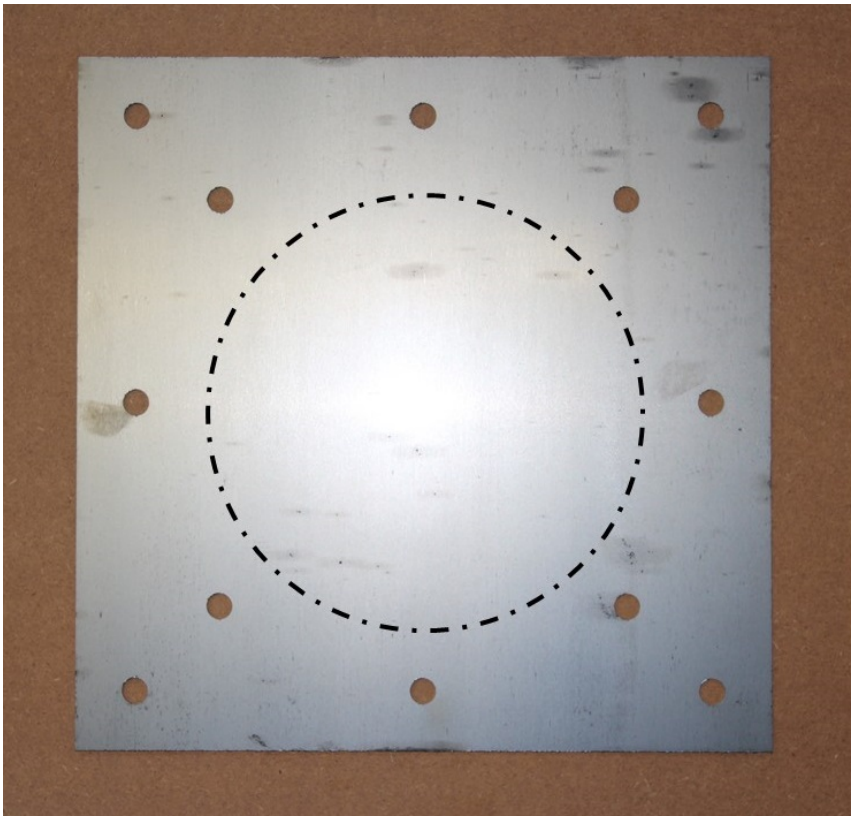

Figure 3.10 Photograph of a blast plate before testing. The circle highlights the exposed to the blast load.

The clamped specimen was placed onto a ballistic pendulum, similar to the one used by Nurick *et al.* [56, 57, 58]. A schematic of the ballistic pendulum is illustrated in Figure 3.11. Counter masses were added to the back of the pendulum to counter balance the mass of the clamping rig. Extra masses were added to the centre of the pendulum to ensure a small swing and a small horizontal displacement so that it would not strike the laser sensor and validate the linearised equations of motion used to determine the impulse on the target plate. The overall set up with the location of the added masses is shown in Figure 3.12.

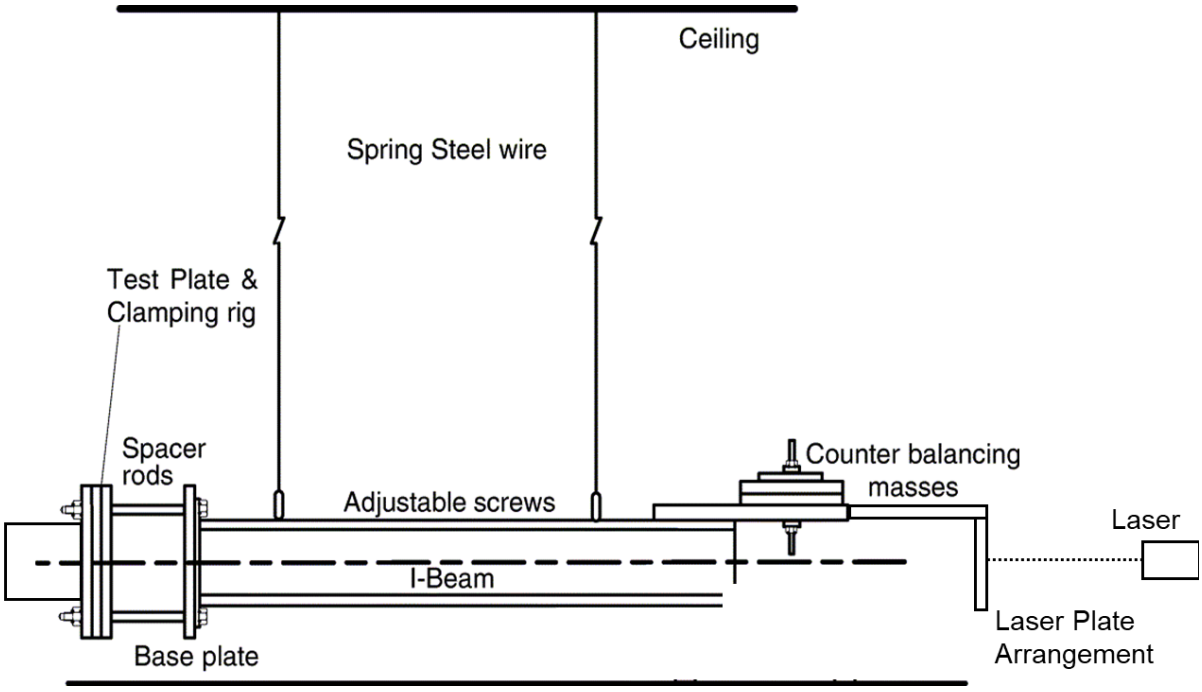

Figure 3.11 Schematic of the ballistic pendulum used in the blast experiments [56].

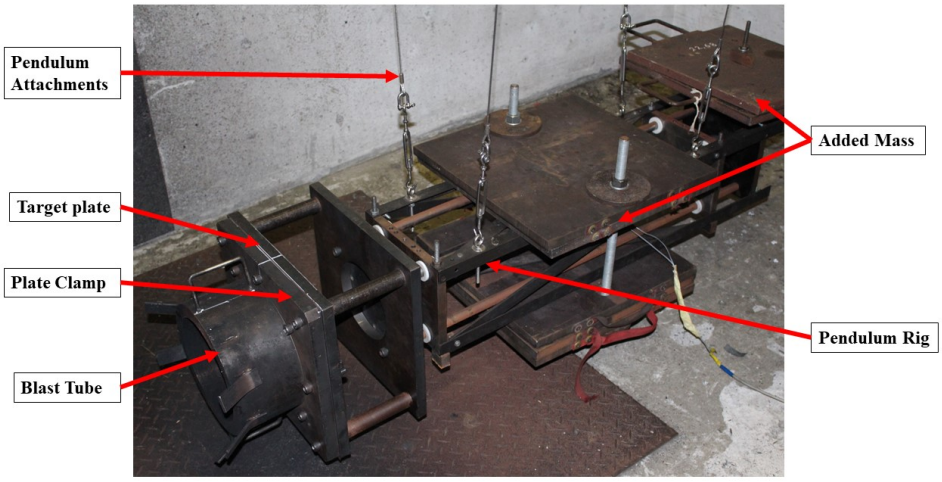

Figure 3.12 Photograph illustrating the set up of the blast rig placed on the pendulum.

The breakdown of the masses of the pendulum is shown in Table 3.2. The "Counter Masses" in the table represent the masses that were added to the back of the pendulum. The "Added Masses" in the table represent the mass added to the centre of the pendulum to limit the swing of the pendulum.

Table 3.2 *Table listing the mass breakdown of the blast pendulum with all the components.*

Part	**Mass (kg)**
Pendulum	54.87
Blast Clamp with extender plates and bolts	66.01
Laser Plate Arrangement	4.02
Counter Masses	70.50
Added Masses	165.16
Domex Target Plate	1.92
Spacers, Nuts and Bolts	4.32
Total	**366.80**

3.3.2 Axial Alignment of the Charge and Ball Bearing

Achieving correct alignment of the charge and ball bearing in the charge was challenging. The overpressure created by a charge is greatly influenced by the shape of the charge in the near and mid field region [83]. A charge mould was designed to ensure consistent shape of the charge and placement of the ball bearing, and a polystyrene wheel was cut by a CNC machine to ensure the placement of the charge with regards to the blast tube was concentric.

3.3.2.1 Charge Shape and Placement of Ball Bearing within the Charge

A cylindrical charge, $20mm$ in diameter, was used for all blast experiments, with the mass of the charge varied in the experiments.

A mould was designed then Resin SLA 3 printed to help shape the charge, and to ensure accurate placement of the ball bearing within the charge. The mould could be opened up horizontally to remove the shaped charge with ease and had two different presses designed, depending on where the ball bearing was placed within the charge. The ball bearing placement varied by percentage mass based on the mass of the relevant charge. Three lining wedges on the bottom casing, with corresponding lining holes present on the top casing, ensured accurate plate of the casings with respect to each other. The bottom of the mould had holes to allow air to escape. A model of the mould is presented in Figure 3.13.

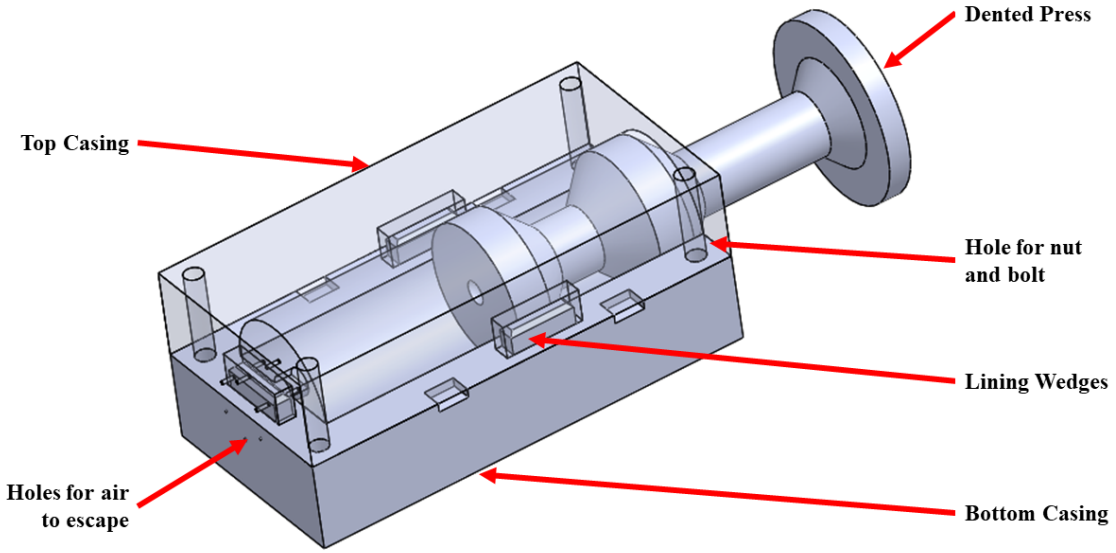

Figure 3.13 Isometric CAD view of the mould used to shape the charge, with the top casing made transparent so the internal cylinder can be viewed.

3.3.2.1.1 No Ball Bearing Placed within the Charge.

If no ball bearing was required for the experimental set up, the required mass was measured on a scale and then placed into the mould. The mould was bolted tight using four wing nuts in the corner holes, with a flat press used to compress the charge into shape. The different presses used can be viewed in Figure 3.14. The mould was then opened up and the charge was removed for testing.

(a) CAD model showing the press with the flat face used to compress the PE4 into place.

(b) CAD model of the press with the spherical cut out used to place the ball bearing in the PE4 if required.

Figure 3.14 CAD model of the two different presses used to shape the charge.

3.3.2.1.2 Ball Bearing Placed at Various Depths.

If a ball bearing was required in the charge for testing, the mass behind and in front of the ball bearing, based on its required position, was calculated. The mass behind the charge was placed into the mould and compressed into shape by the flat press. The flat press was removed and a ball bearing was placed into the dented press. The dented press, with the ball bearing placed in the cut out, was compressed into the first mass and the ball bearing was deposited onto the charge face. This method ensured the ball bearing was placed on the axis of the charge and that the ball bearing was half buried in the charge. The ball bearing being half buried, ensured the ball did not move when the remaining mass was placed. The remaining mass was measured and placed in the mould and compressed against the first mass and ball bearing, placing the ball bearing at the required depth. If the ball bearing was placed right at the end of the charge, no second mass was placed after the ball bearing was placed in the charge. Once the charge was prepared, it was removed from the mould and used on the blast experiments.

3.3.2.2 Charge Location

For consistency between tests, the placement of the charge had to be located in the same position and orientation for every detonation. The consistent location of the charge was ensured by the use of a polystyrene wheel, which was designed to hold the cylindrical charge in the centre of the blast tube as illustrated in Figure 3.15.

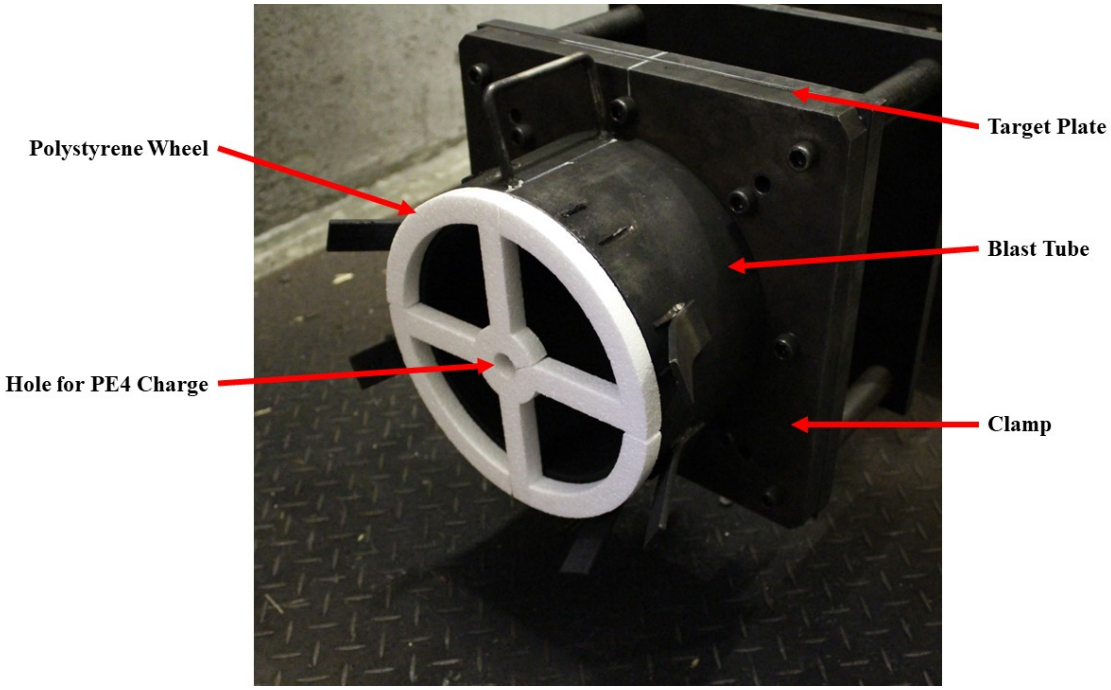

Figure 3.15 Photograph of the polystyrene wheel placed on the blast tube.

The wheel had the same outer diameter as the blast tube to allow for easy orientation when lining up the blast tube and polystyrene wheel, as the two circles had to be concentric. Double sided tape held the polystyrene wheel in place when placed on the tube. The polystyrene wheel was cut using a CNC (Computer numerical control) machine for consistency. The charge was placed in the hole in the polystyrene. If necessary, a small polystyrene triangle was attached under the charge on the outside of the wheel to support the hanging PE4 mass for the longer charges.

3.3.3 Blast Experiments

3.3.3.1 Blast Loading with Bare Charges

In these blast tests, two series of experiments were carried out with two different target plates; a complete target plate and the Pre-cut target plate. These series were conducted to determine the effects of a blast wave on complete plate with no ball bearing using the complete target plate, and to investigate the effects for situations when the ball bearing penetrated the plate before the blast wave arrived, using the Pre-cut target plate. The charge was set up without any ball bearing to examine the effects of the blast load acting on the different target plates. This series consisted of detonating 3 charges with masses of $10g$, $20g$ and $30g$. The target plates were made from DOMEX 700 steel and were $350mm$ x $350mm$ x $2mm$ in size.

The Pre-cut target plates had a small $5mm$ diameter hole, the same size as the ball bearing, cut in the centre of the plate. These holes were placed to determine the effects of the blast loads onto a perforated plate (penetrated by the projectile). This would happen when the IED is placed further away from the target [78].

3.3.3.2 Combined Blast Loading

In these blast tests, the charge was set up with the ball bearing placed in various locations along the cylindrical axis of the charge. These experiments were conducted to study the combined effect of blast and projectile loading in the same event. For theses experimental loads, several locations, listed in Table 3.3, were considered for the ball bearing placement in the cylindrical charge.

Table 3.3 *Table depicting the percentage depth of the ball bearing for each numerical simulation.*

Placement						
Number	1	2	3	4	5	6
Depth	$0mm$	$2.5mm$	20%	30%	40%	50%

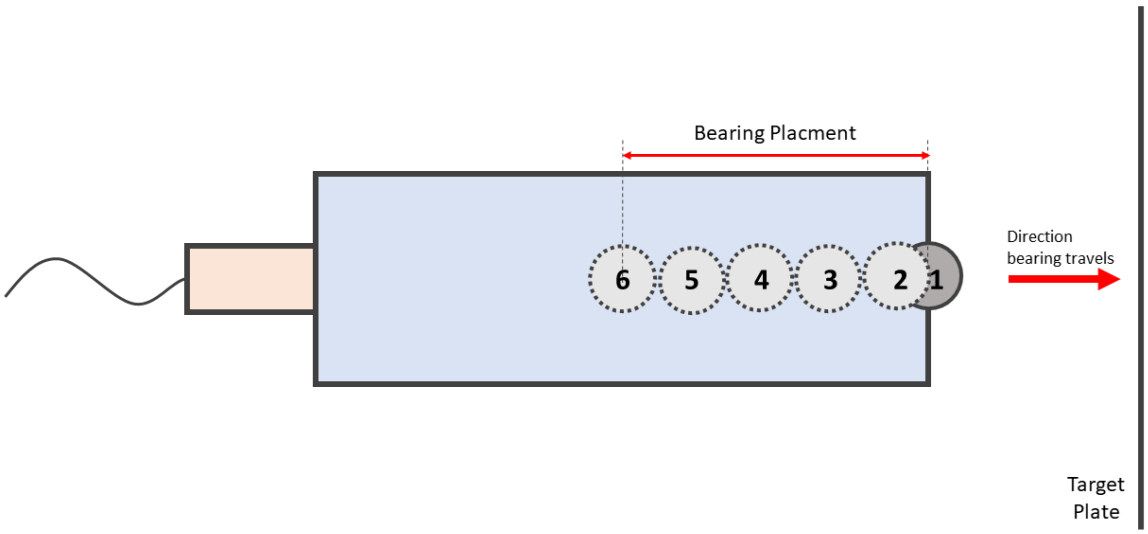

Figure 3.16 Sketch showing the different placements for each ball bearing for each charge. For ball bearing placement calculations, refer to Table 3.3.

The first two placements are based on the size of the $5mm$ ball bearing, with placement 1 being half buried in the charge and placement 2 being $2.5mm$ into the charge, measured from the centre of the ball bearing to the circular face of the charge facing the target plate. This is illustrated in Figure 3.16. The remaining 4 placements were positioned based on percentage mass in front of the charge. So a ball bearing that was 20% deep, had 20% mass in front of the ball bearing and 80% mass behind it.

This series consisted of detonating 3 charges with masses of $10g$, $20g$ and $30g$. The target plates were made from DOMEX 700 steel and were $350mm$ x $350mm$ x $2mm$ in size. When the ball bearing was placed in placements 4 and higher, the impact of the ball bearing on the target plate was, in most cases, not central. This decreased consistency between experiment types and prevented the measuring of true accurate deflection as the maximum deflections from the separate loads would not be directly added to each other if the bearing impacted off centre. For this reason, only placements were 1 through to 3 were used for the experiments.

3.3.4 Blast Driven Ball Bearing Average Velocity Tests

The set-up used was similar to that used by Qi *et al.*[61]. The ball bearing arrival time was measured using a Hopkinson Pressure Bar (HPB). The HPB consisted of a $20mm$ diameter silver steel bar with a pair of axial strain gauges mounted $300mm$ from the impact face. The strain gauges were connected to a strain gauge amplifier and the signals recorded using a Picoscope. The bar had an aluminium cap placed on the front end of the bar to act as a witness plate to minimise damage to the Hopkinson bar. The bar and aluminium cap were incorporated into the design of the blast pendulum by Qi *et al.* [61] and adapted for this study. The full assembly of the pendulum is shown in Figure 3.18. The bar was placed in the centre of the rig and could slide in line with the target plate. For these experiments, the target plates, shown in Figure 3.19, were made from DOMEX 700 steel and were $350mm$ x $350mm$ x $5mm$ in size. These plates had a $21mm$ diameter hole cut out in the centre to allow the bar with the aluminium cap to align with the target plate. The arrangement is shown in Figure 3.17. A break wire placed directly under the detonator to trigger the start of the signal capture. When the detonator triggered, the break wire broke causing a change in the voltage of a circuit which started the recording of the picoscope, enabling the impact time to be measured from detonation.

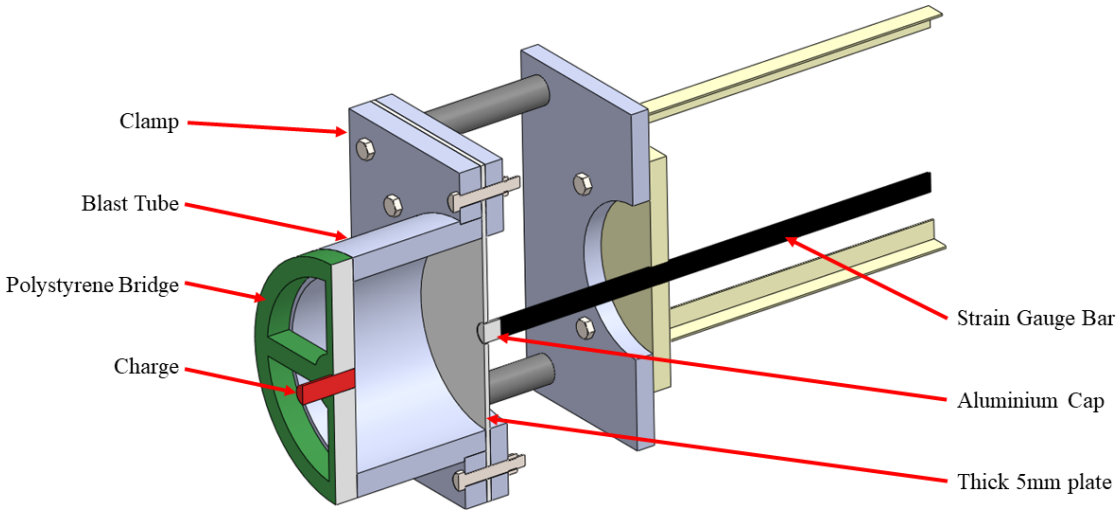

Figure 3.17 3D CAD model showing the internal design of the blast rig.

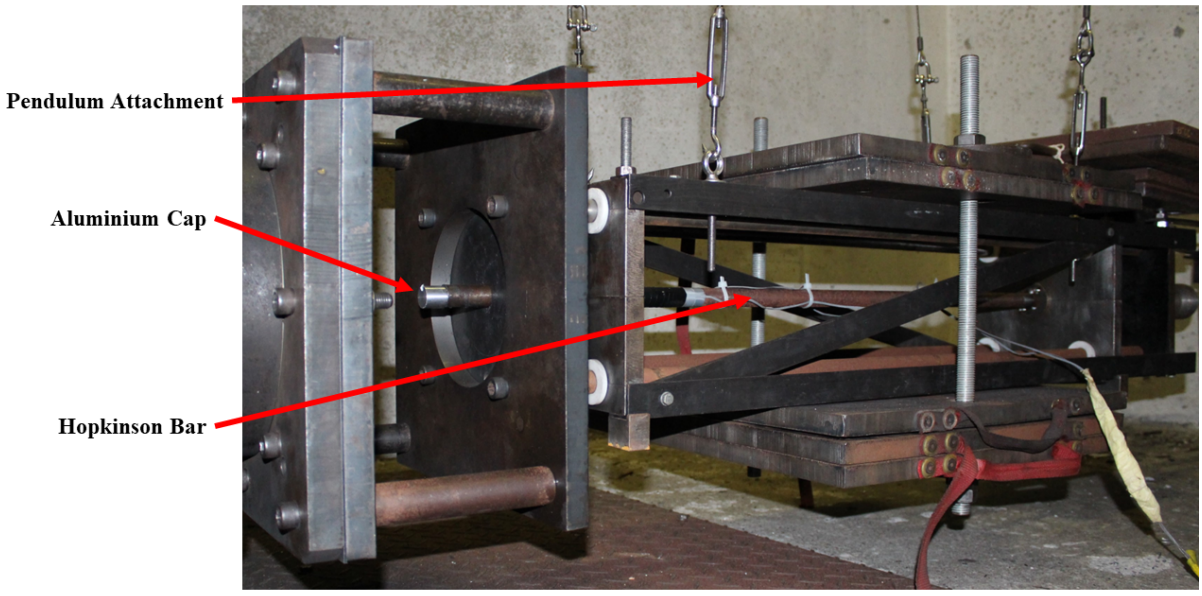

Figure 3.18 Photograph of the clamp rig used to capture the impact time with the Hopkinson bar.

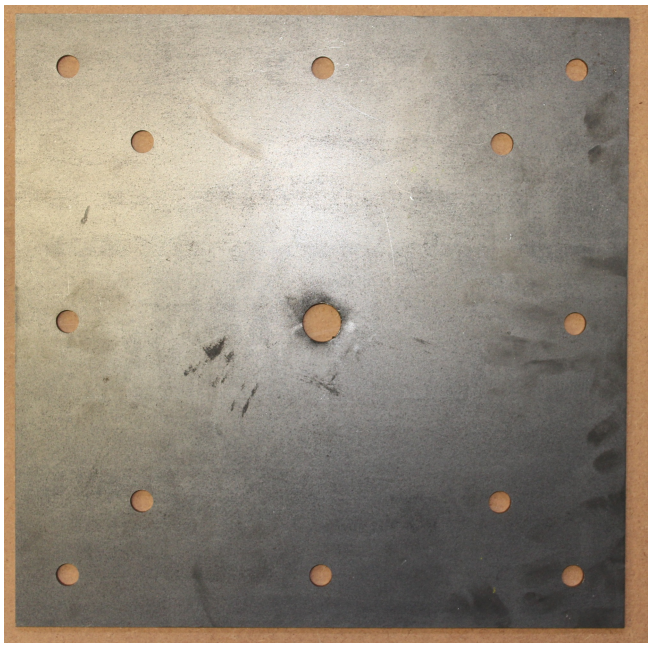

Figure 3.19 Photograph of the $5mm$ thick target plate with hole to allow the aluminium cap to pass through to measure impact of ball bearing.

Chapter 4

Experimental Results

The results obtained from the different series of experiments are presented in this chapter.

4.1 Blast Impulse

4.1.1 Charge Size

From Figure 4.1, it was observed that the increase in charge size increased the maximum impulse delivered to the pendulum and target plate, with the same trend present regardless of the bearing placement.

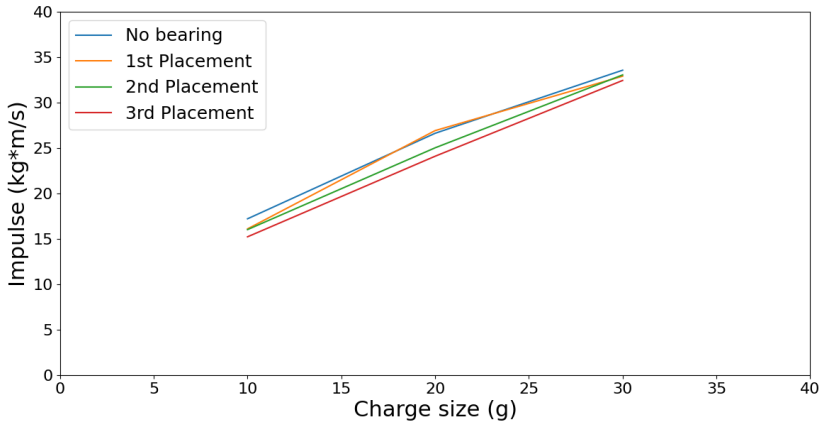

Figure 4.1 Graph comparing the charge size to impulse delivered for the various bearing placements.

4.1.2 Ball Bearing Placement

Figure 4.2 shows three graphs for the various charge sizes that were tested with the ball bearing placement as the independent variable. A slight decrease in impulse delivered to the plate as the ball bearing was placed deeper into the charge along the cylindrical axis was observed. While there was a slight decrease visible, there were only four points per trend. For this reason, these results were not conclusive and more data was required to analyse this further.

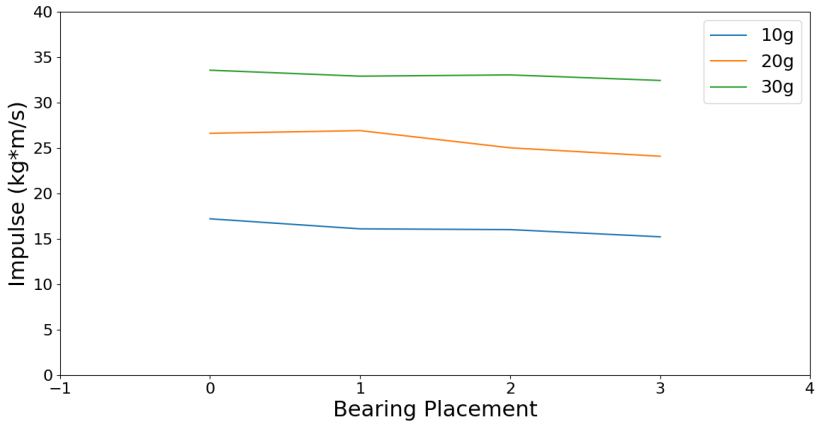

Figure 4.2 Graph comparing the ball bearing placement to impulse.

4.2 Results from the Projectile Impact Velocity Tests

The results from the projectile impact test are listed in Table 4.1. Figure 4.3 shows the typical deflection of a target plate after the impact velocity test. A similar deformation pattern to that reported by Nishida *et al.* [71] with hemispherical craters was observed. The deflection was characterised by a localised crater created by the projectile impact, with no significant global deflection. The typical deflection is shown in Figure 4.4. Measuring crater depth on the impact face would be prone to inaccuracies due to the difficulties locating a depth probe in the very small indentation. The deflection was, therefore, measured at the back of the plate using a height gauge. The ball bearing exhibited signs of compression where it impacted the target plate, along with slight cracks running down the length of the ball bearing, perpendicular to the compressed face of the ball bearing, as shown in Figure 4.5.

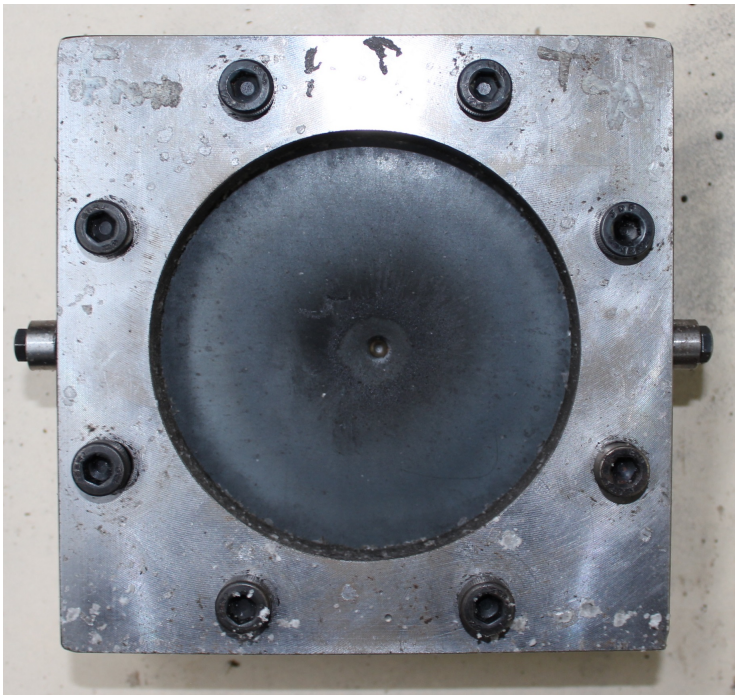

Figure 4.3 Photograph of a Domex 700 projectile impact target plate in the steel clamps after being been exposed to a ball bearing impact loading.

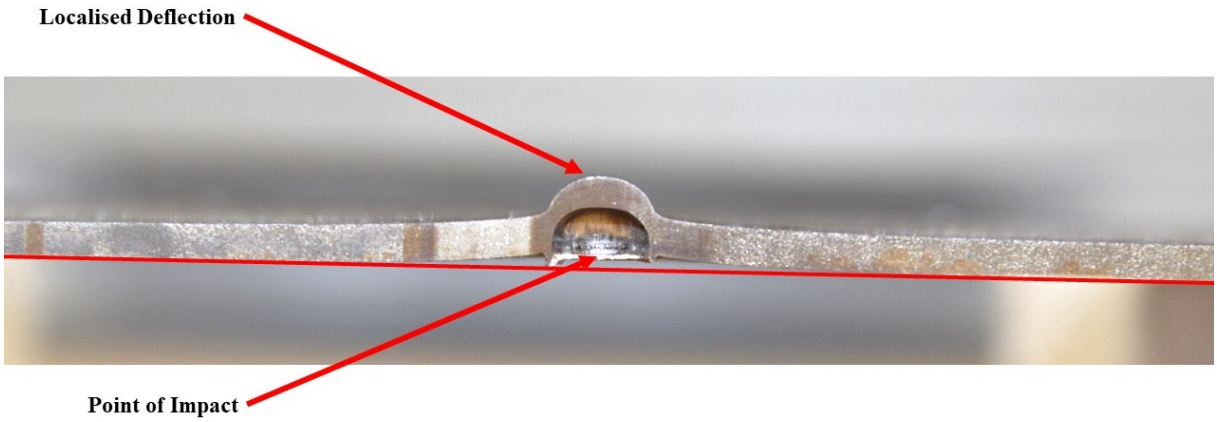

Figure 4.4 Photograph of a Domex 700 target plate from the impact experiments having been exposed to a ball bearing impact loading.

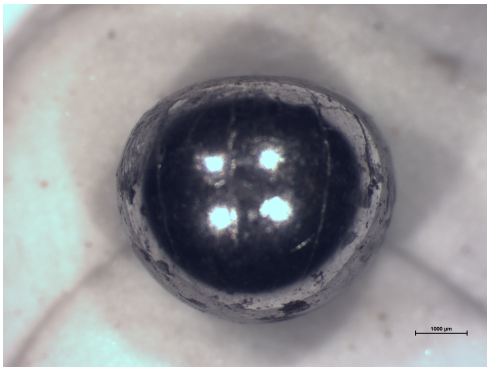

Figure 4.5 Photograph of a $5mm$ ball bearing showing signs of compression after it impacted a target plate during impact testing.

The plate deflection was measured at 5 different locations, shown in Figure 4.6, to ensure regularity in the measuring process using a digital height gauge with a resolution of $0.01mm$. Locations E1, E2, E3 and E4, located on the edge of the plate were used as the 'zero deflection' points. The maximum final deflection was measured at location C1 in the central area of the plate. Table 4.1 lists the deflection a target plate experienced when exposed to ball bearings with the corresponding average velocity in the table. The velocity was achieved using the gas gun firing pressure listed.

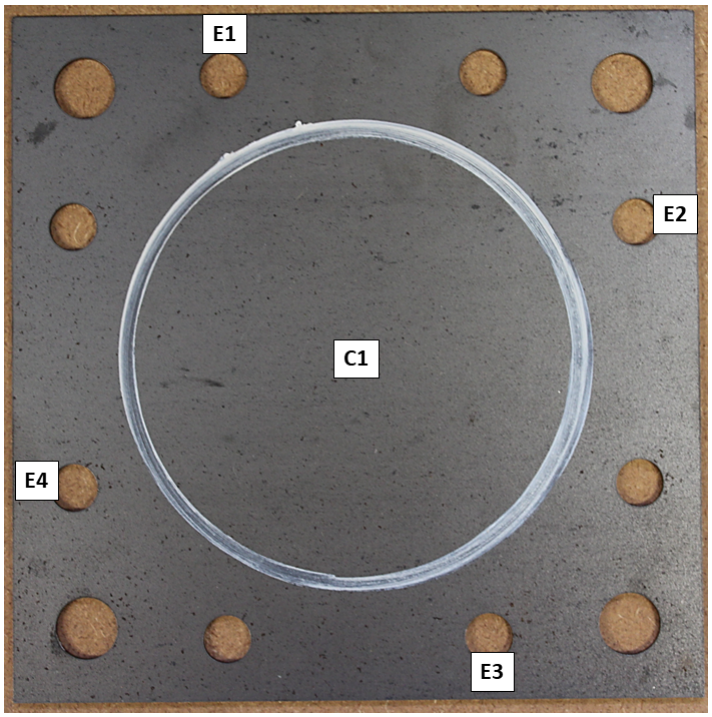

Figure 4.6 Photograph of a Domex 700 target plate showing the points were the height was measured.

Table 4.1 *Table listing the deflections of the Domex 700 target plates after being exposed to a ball bearing impact at varying velocities.*

Experiment Number	**Gas Gun Firing Pressure** (kPa)	**Average Velocity** $m \cdot s^{-1}$	**Deflection** mm
7.26.2	620	397	1.53
7.26.3	990	488	2.37
7.26.4	360	249	0.74
7.29.1	810	136	0.38
7.29.2	992	360	2.12
7.29.3	992	506	2.60
7.29.5	155	82	0
8.23.11	1100	433	2.62

Figure 4.7 depicts the measured deflection vs impact velocity from the experiments. The results show a strong trend of greater deflection with a higher velocity as expected.

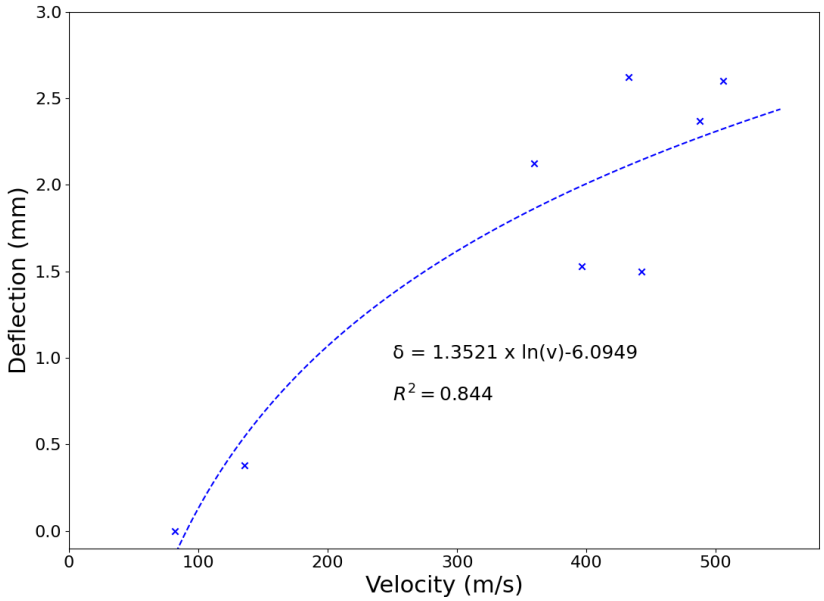

Figure 4.7 Graph showing the deflection vs ball bearing impact velocity.

4.3 Blast Loading Results

4.3.1 Blast Loading with Bare Charges

The target plates experienced a global deflection similar to what was described by Teeling-Smith and Nurrick [50] for uniform blast load over the exposed area. The typical deflection of a target plate after blasting can be seen in Figure 4.8. There was little difference observed between the two target plates after being exposed to charges of the same shape and size.

(a) Typical deflection observed from a complete target plate.

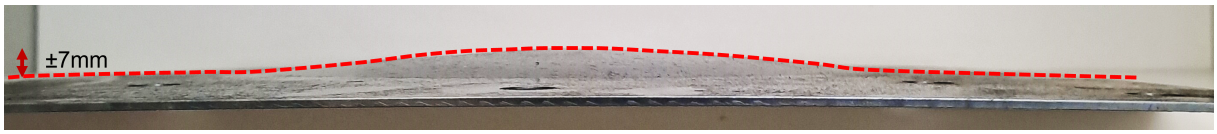

(b) Typical deflection observed from a pre-cut target plate.

Figure 4.8 Typical deflection observed from target plates after bring exposed to blast loading from a $30g$ charge.

The plate deflection was measured at 5 different locations, shown in Figure 4.9, to ensure regularity in the measuring process while using a digital height gauge with a resolution of $0.01mm$. Locations R1, R2, R3 and R4, located on the edge of the blast area were used as the 'zero deflection' points. The maximum final deflection was measured at location C in the central area of the plate.

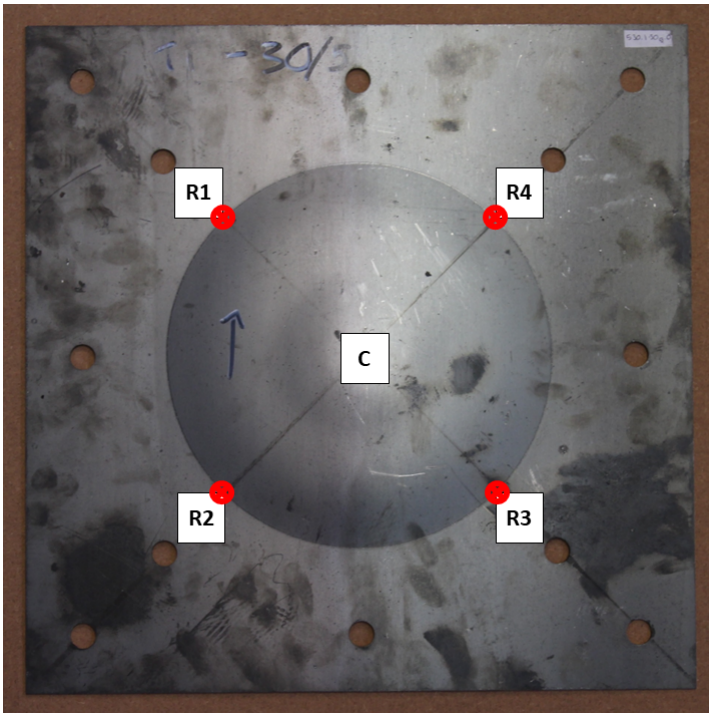

Figure 4.9 Photograph of a target plate highlighting the locations where each plate was measured after blast testing.

Table 4.2 shows the target plate deflections for both complete and pre-cut target plates when exposed to the detonations of various charge masses with no bearing present.

Table 4.2 *Table listing the global deflections of the target plates after they exposed to various charge masses with no ball bearings present in the detonation.*

Experiment Number	**Pre-cut Plate** **(Y/N)**	**Charge Size** (g)	**Deflection** (mm)	**Impulse** $(kg \cdot m \cdot s^{-1})$
6.08.2	N	10	3.07	17.2
5.31.4	N	20	5.30	26.61
5.30.1	N	30	7.33	33.56
6.9.2	Y	10	3.05	15.1
6.9.3	Y	20	5.06	25.4
6.9.4	Y	30	7.33	33.9

Figure 4.10 shows the deflections of the plates, exposed to various charge masses and comparing whether having a $5mm$ hole pre-cut in the plate produced significant differences in the final deflection. As seen from Figure 4.10, there was very little difference between whether the plate had a hole present prior to blasting, with the difference less than the thickness of the plate.

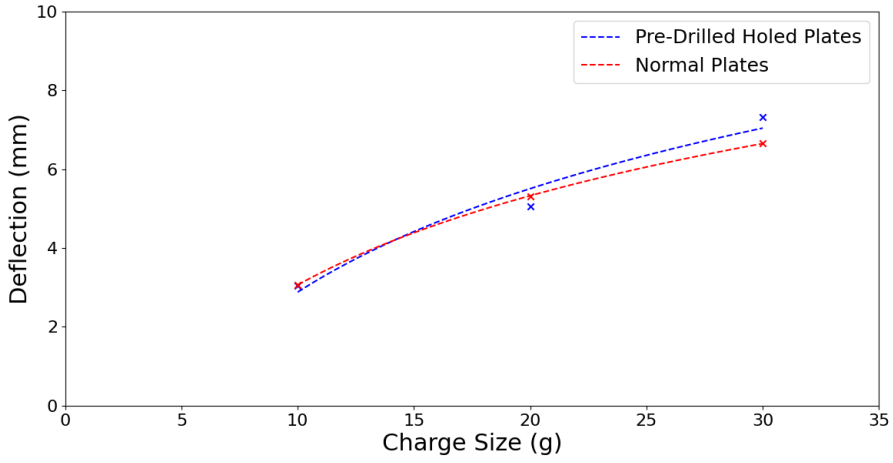

Figure 4.10 Graph comparing the deflection of target plates when exposed to blast loading with no ball bearing present and a pre-cut target plate.

4.3.2 Target Plates Exposed to Combined Loading

All plates subjected to combined loading presented the same features when the bearing did not penetrate the plate. The deformation of the plate was characterised by a global dome present similar to that of the target plates exposed to uniform blast loading. A smaller localised dome was also present on top of the global dome where the ball bearing impacted the target plates as shown in Figure 4.11. Figure 4.11 compares the deflections of three different target plates, all exposed to Placement 2 of the ball bearing location but with varying charge masses, ranging from $10g$ to $30g$. The plates were cut through the maximum deflection to allow for a sectional comparison. The ball bearings after combined loading showed signs of burn and impact damage.

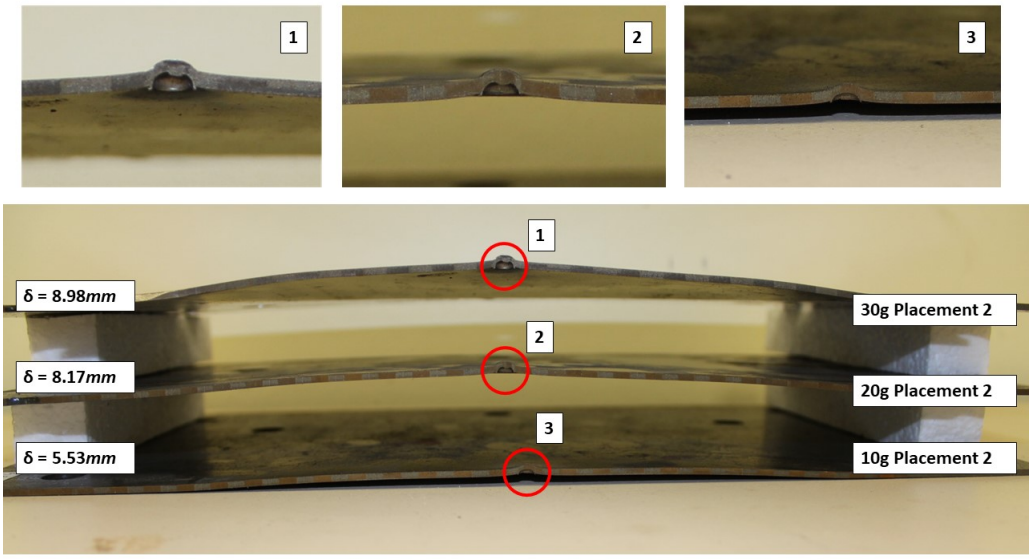

Figure 4.11 Photograph showing the global deflection of plates sectioned through the global deflection point for the Placement 2 (varying charge masses), along with a detailed photo of the localised deflection.

The ball bearing exhibited the same compression feature as the ball bearings from the velocity impact tests. The blast driven ball bearings also had burn marks present on the surface of the ball bearing due to the temperatures from the blast, along permanent deformation around the compressed area. A blast driven ball bearing after testing is shown in Figure 4.12.

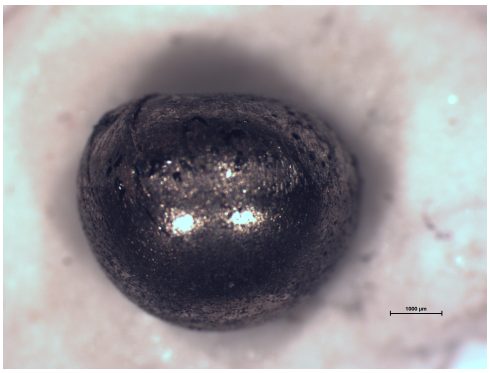

Figure 4.12 Photograph of a $5mm$ ball bearing showing signs of compression and burning after it impacted a target plate during combined load testing.

The characteristics of a deflected target plate subjected to a combined load are depicted in Figure 4.13. The different deflections associated with the different aspects of the combined loads were defined as:

- The global or total deflection is the overall deflection caused by both of the impact and blast loading.
- The 'cap' deflection is defined by the dome shaped impact caused by the ball bearing impacting the plate.
- The blast deflection is measured as the deflection of the plate without the cap deflection.

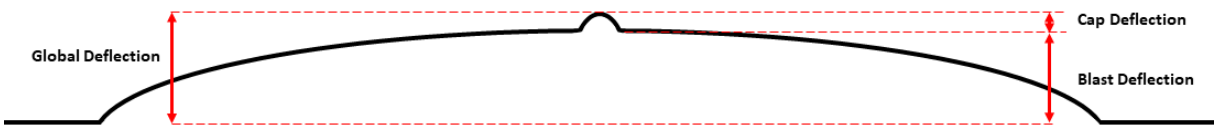

Figure 4.13 Schematic of a deflected target plate explaining the different deflections used in combined loading.

Figure 4.14 gives a brief illustration of the placements to help understand the placements of the ball bearing and the associated deflections. Four points around the cap using a digital height gauge were measured and the average was compared to the global

deflection on the back of the plate. The results are listed in Table 4.3 and presented graphically in Figure 4.15.

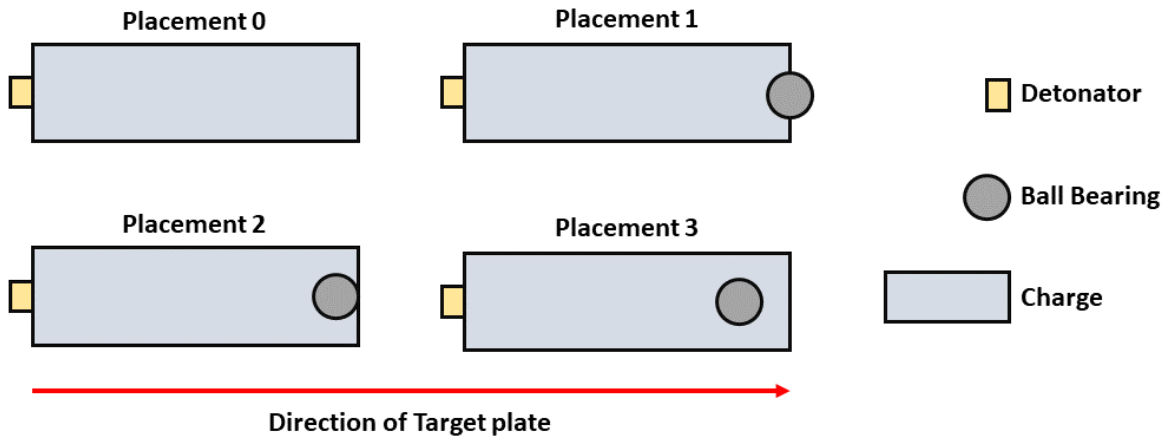

Figure 4.14 Schematic of a charge illustrating each ball bearing placement.

Table 4.3 *Table listing the global and cap deflection of the combined loading deflection. *P shows that the ball bearing penetrated the plate so no cap could be measured.*

Test Number	Charge Mass (g)	Placement	Global Deflection (mm)	Cap Deflection (mm)	Impulse ($kg \cdot m \cdot s^{-1}$)
5.30.2	30	1	7.02	*P	32.9
5.30.3	30	3	6.41	0	32.4
5.30.4	30	3	6.66	0	32.43
5.31.1	30	2	8.98	1.64	33.04
5.31.2	20	1	5.96	*P	26.91
5.31.3	20	2	8.17	1.43	25.01
6.8.1	20	3	5.22	0	24.09
6.8.3	10	1	5.44	1.41	16.09
6.8.4	10	2	5.53	1.18	16.01
6.9.1	10	3	3.56	0.74	15.22

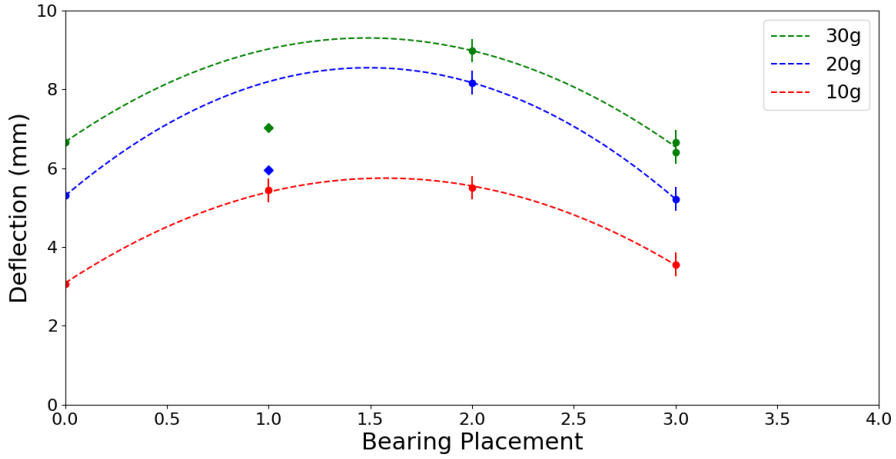

Figure 4.15 Graph comparing the global deflection to ball bearing placement for various charge masses.

From Figure 4.15, it was deduced that the greatest deflection, with relation to the bearing placement, was most likely to occur at Placement 2. The greatest chance of the bearing penetrating the target plate was at Placement 1, with increasing odds of penetration occurring at larger charge sizes. The deflection decreased in magnitude as the bearing was placed further down the axis of the cylindrical charge.

Figure 4.16 shows the deflection of the cap, measured from the combined loading experiments, with the impact velocity inferred from the numerical simulation work [1] . For all deflections measured using the height gauge, an uncertainty of $\pm 0.1mm$ was assumed. This is visible by the error bars in Figure 4.16. The velocity accuracy also has error bars due to the differences between the numerical simulations and experiments, discussed further in section 4.4. It should be noted that the trend lines for the $20g$ and $30g$ charges were assumed from the $10g$ due to the lack of data points. From the impact velocity tests, the cap deflection was deemed to be zero at the threshold velocity of $91.45m \cdot s^{-1}$. All three charges have a point placed at $0mm$ deflection for the threshold velocity.

[1]The ball bearing velocity could not be determined for placements other than Placement 1, so all other velocities were taken from the numerical simulations(Chapter 6).

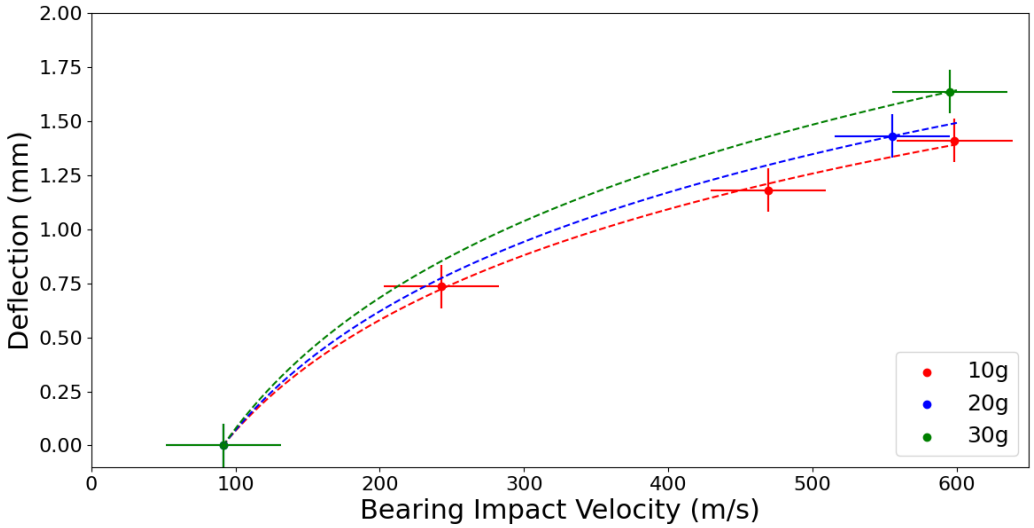

Figure 4.16 Graph showing the cap deflections from the blast experiments grouped for various charge masses.

4.4 Blast Driven Ball Bearing Average Velocity Tests

Table 4.4 lists the results of the experiments performed with varying charge masses and ball bearing placements to determine the impact time of the ball bearing onto a target $150mm$ away from the charge. The $5mm$ thick target plate was selected to protect the Hopkinson bar and the wiring placed behind the target plate on the pendulum. The ball bearings showed similar markings to that of combined loading events, where signs of burning and impact damage were present. From the experiments, there was no visible deflection present on the target plate but there were some burn marks present, as shown in Figure 4.17.

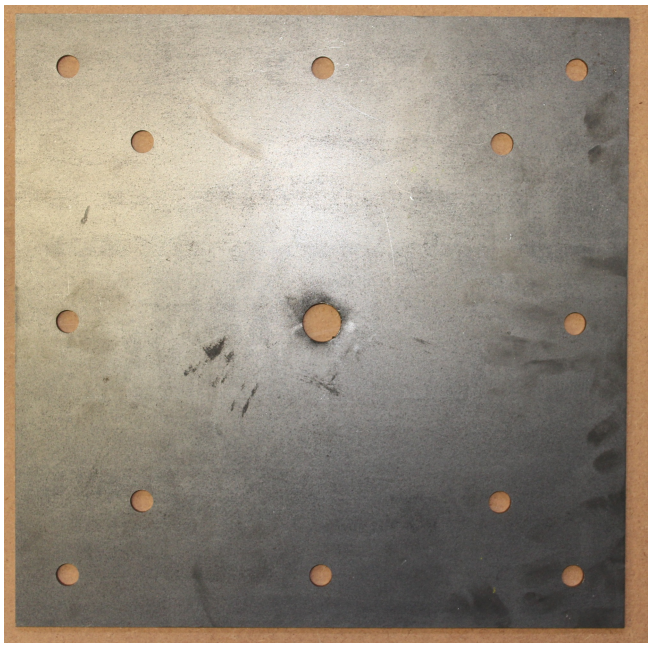

Figure 4.17 Photograph of the $5mm$ thick target plate with hole exhibiting burn marks around the hole.

In some cases, the ball bearing did not impact the aluminium cap. When the ball bearing was placed further inside the length of the charge it was less likely the ball bearing would impact the $20mm$ aluminium cap. Consequently, most experiments were carried out with the ball bearing located at placement 1 using varying charge masses. Throughout this experiment series, there were three type of impacts defined;

- Full impact (when the ball bearing impact crater was fully within the diameter of the aluminium cap)
- Partial impact (when the ball bearing impact crater was partially within the diameter of the aluminium cap)
- No impact (when the ball bearing impact crater was outside the diameter of the aluminium cap)

as shown with photographs in Figure 4.18 and schematically in Figure 4.19.

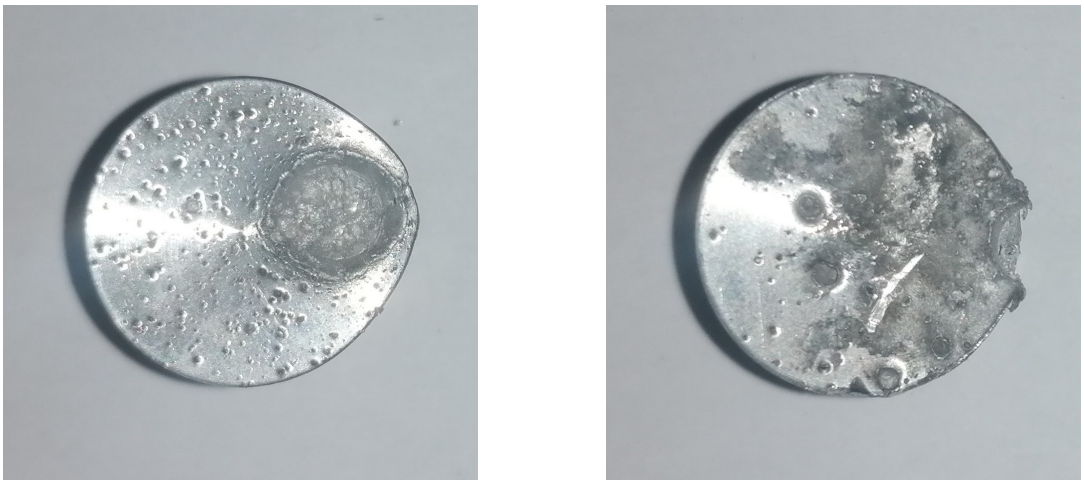

(a) Full Impact **(b)** Partial Impact

Figure 4.18 Photographs showing the types of impact for the ball bearing on the aluminium cap for various experiments, all with a $30g$ charge.

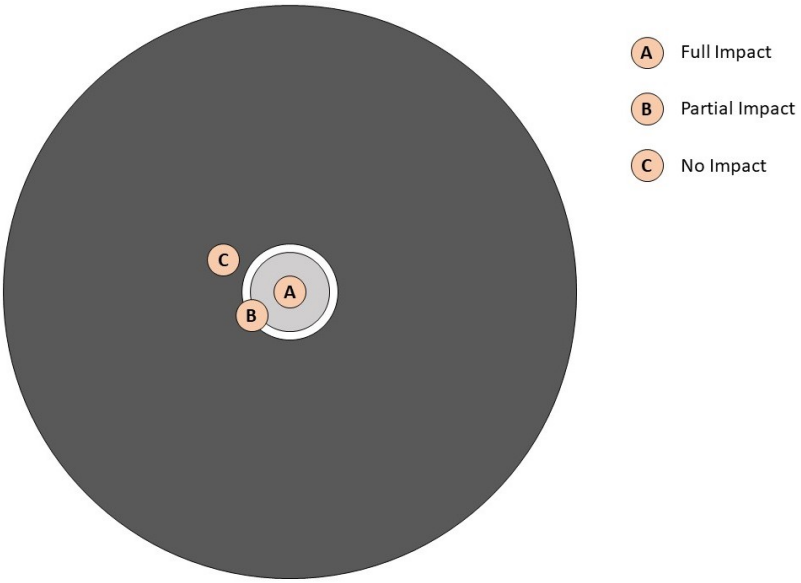

Figure 4.19 Schematic illustrating the type of impacts possible on the aluminium cap and surrounding plate.

Table 4.4 *Table of Results listing the ball bearing impact validation contact type.*

Experiment Number	**Charge Mass** (g)	**Ball Bearing Placement**	**Contact with Aluminium Cap**
4.12.1	30	1	Full
4.13.1	30	2	No
4.13.2	30	2	No
4.13.3	30	4	No
4.13.4	30	1	Partial
4.13.5	30	1	Partial
4.21.1	20	1	Full
4.21.2	20	1	No
5.05.1	20	1	No
5.05.2	20	1	Partial
5.05.3	20	1	No
5.05.4	20	1	Partial
5.23.1	10	1	Full
5.23.2	20	1	No
5.23.3	20	1	Full

The impact time of the ball bearing was determined using the inferred stress wave data captured from the Hopkinson bar. Typical raw data from the oscilloscope is shown in Figure 4.20. The blue graph in Figure 4.20 shows the voltage captured from the Hopkinson bar. The red graph shows the data captured from the break-wire trigger placed in contact with the detonator. Upon detonation, the break wire caused a voltage jump which was used to trigger the oscilloscope recording and provided a consistent reference for the detonation time. The initial spike in the blue graph indicated when the pressure wave reached the strain gauge after impacting the Hopkinson bar. The second spike indicated when the ball bearing impacted the aluminium cap and the compression wave travelled down the Hopkinson bar to the strain gauge.

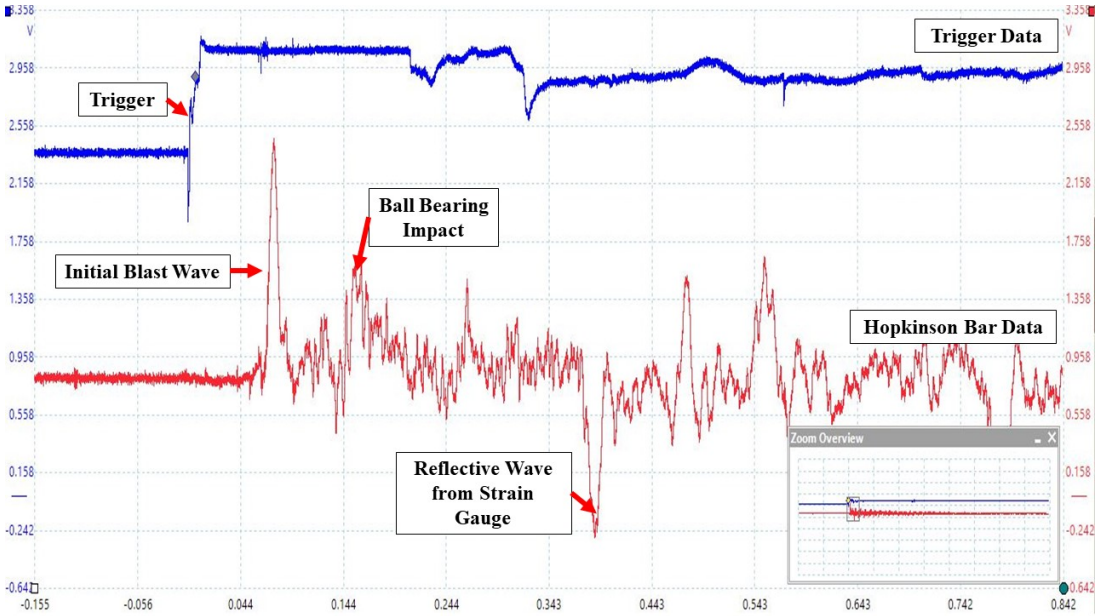

Figure 4.20 Graph showing the raw data captured by the Hopkinson Bar from a 30g charge with the ball bearing at Placement 1 (Exp 4.13.5).

Axial loading from either the blast pressure wave or ball bearing impact would cause a stress wave to travel down the Hopkinson Pressure Bar. The strain gauge on the Hopkinson bar would record the stress wave as a change in voltage. The wave speed was calculated using axial impact tests with a gas gun. The distance from the impact face of the cap to the strain gauge was used along with the wave speed to determine the time delay between loading the impact face and recording the stress wave at the strain gauges. The data from the Hopkinson bar was shifted on time axis, assuming a non-dispersive wave, to account for this time delay, as performed by Qi *et al.*[61]. The typical time corrected data gathered from the Hopkinson bar can be observed in Figure 4.21. The initial peak observed by the Hopkinson bar was the primary pressure wave. The second peak was the secondary blast pressure wave arriving, and the third peak was the ball bearing impact.

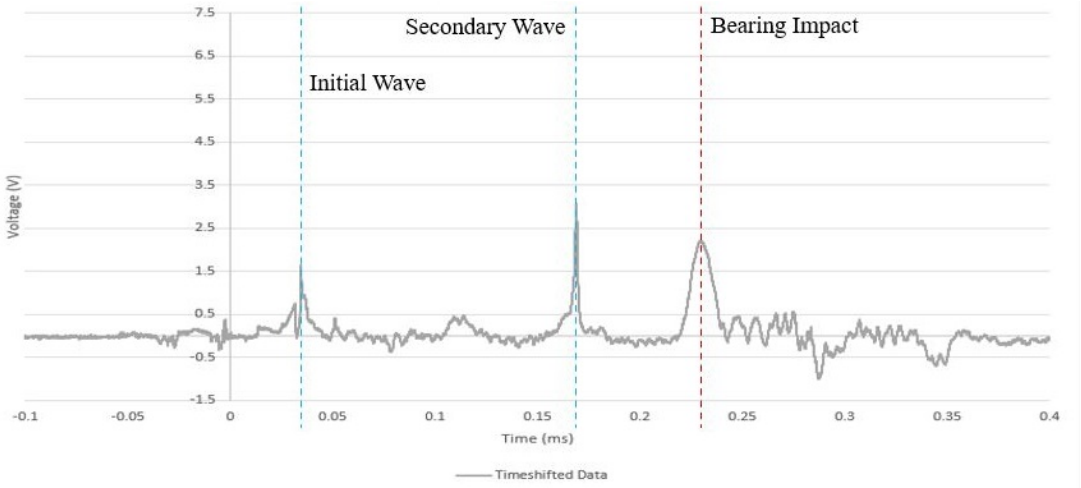

Figure 4.21 Graph illustrating the time corrected data from a $20g$ with the ball bearing at Placement 1 (Exp 4.21.1). The time corrected data accounts for the time taken for the stress wave to travel down the bar.

Figure 4.22 shows the data captured from the Hopkinson bar for three repeated experiments at $30g$ charge mass and Placement 1, listing the impact time on top of each peak after accounting for the time delay. Figure 4.23 indicated that when the ball bearing impacted closer to centre of the aluminium cap, or was a full impact event as defined in Figure 4.19, it allowed for a larger transfer of momentum (Exp 4.12.1). When the ball bearing impacted on the edge of the cap, or was a partial impact event as defined in Figure 4.19, a lower axial momentum transfer was noted as the ball would have a larger radial velocity component after impact so less energy was transferred to the Hopkinson Bar.

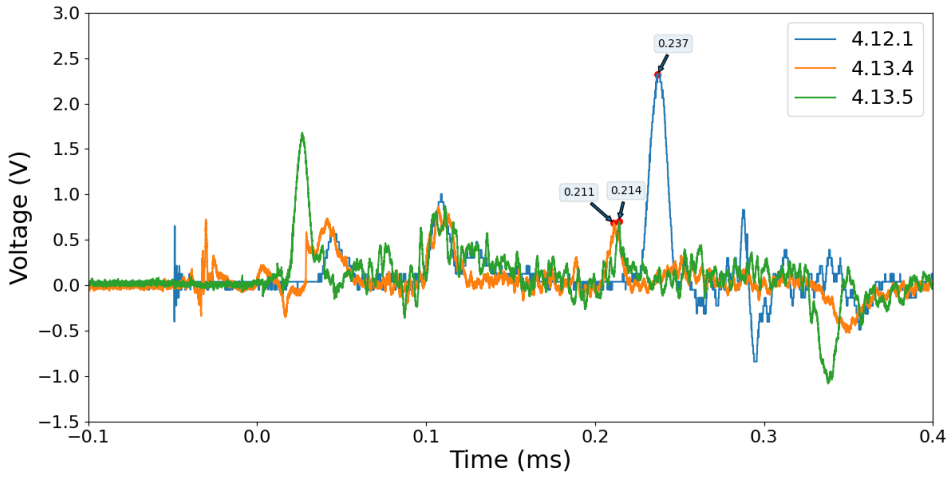

Figure 4.22 Graph showing the data captured from the Hopkinson bar for all the experiments using $30g$ charges with the ball bearing at Placement 1 which captured the ball bearing impact.

(a) Full Impact - Experiment 4.12.1

(b) Partial Impact - Experiment 4.13.4

(c) Partial Impact - Experiment 4.13.5

Figure 4.23 Photographs showing the location of impact for identical ball bearings on the aluminium cap for various experiments.

From Figure 4.22, the data gathered from three separate experiments of identical set up show similar trends and peak locations. The larger ball bearing impact peak for Experiment 4.12.1 provided evidence of a larger momentum transfer due to the impact type. The two initial waves are two pressure waves from the detonation arriving prior to the bearing impact. The bearing impact times were closely grouped. This provided evidence of consistency in the experimental set up.

Table 4.5 shows the impact time from the experimental data where the ball struck the

aluminium cap and produced a distinguishable impact wave. The impact time from these experiments was compared to the time of arrival from numerical simulations, discussed in Chapters 5 and 6. The difference in time was compared and an average time difference was calculated. Figure 4.24 shows the impact time data in a graphical form.

Table 4.5 *Table of results listing the impact time of the experimental data and the numerical simulation data.*

Experiment Number	Ball Bearing Placement	Charge Mass (g)	Experimental Impact Time (ms)	Simulation Impact Time (ms)	Difference (ms)	Error (%)
4.12.1	1	30	0.237	0.227	-0.01	-4.41
4.13.4	1	30	0.211	0.227	0.016	7.05
4.13.5	1	30	0.214	0.227	0.013	5.73
$30g$ Charge Differences					0.006	2.79
4.21.1	1	20	0.23	0.214	-0.016	-7.48
5.05.2	1	20	0.24	0.214	-0.026	-12.15
5.05.4	1	20	0.219	0.214	-0.005	-2.34
5.23.3	1	20	0.225	0.214	-0.011	-5.14
$20g$ Charge Differences					-0.015	-6.78
5.23.1	1	10	0.263	0.239	-0.024	-10.04

The data from the numerical simulations correlated well with the experiments, with an average difference of $6.33\mu s$ for the $30g$ charges, $14.5\mu s$ for the $20g$ charges and $24\mu s$ for the $10g$ charges which lead to a variation of 12% which was deemed acceptable given the complexity of the problem and units of measurement being milliseconds.

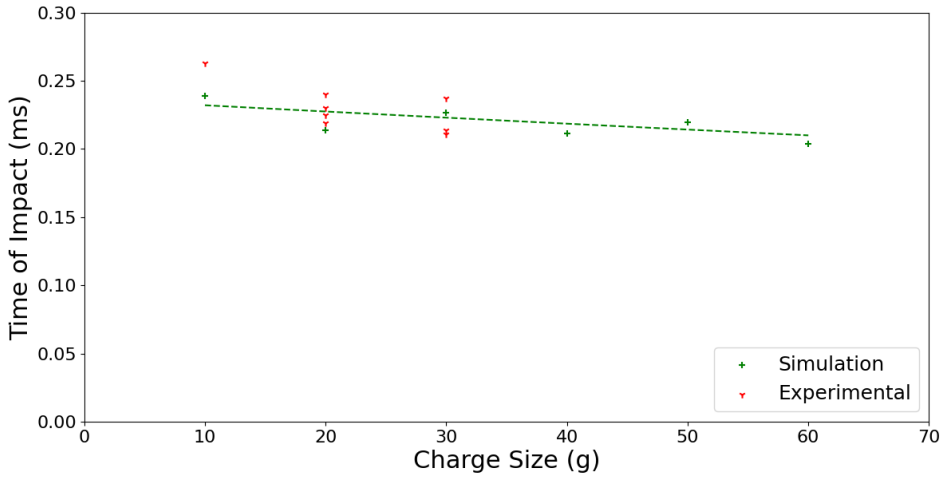

Figure 4.24 Graph comparing the impact time of the simulation to the experimental data.

Chapter 5

Numerical Simulations

The numerical simulations were developed for the examination of plates exposed to blast and combined loading experiments. The ball bearing was embedded at various depths along the cylindrical axis of varying charge sizes. The numerical simulations were used as a way to expand on the experimental work, and to ascertain further trends that could not be captured in the experiments.

5.1 Mesh Convergence Study

Before any simulations were completed, a mesh sensitivity study was carried out to determine appropriate mesh refinement with acceptable accuracy and run times. For this analysis, a wedge set-up, shown in Figure 5.1, was used in every variation. A wedge geometry was chosen as it still utilises a four point cell as the simulation would while drastically reducing simulation time and computing power. Jestin *et al.* [84] also utilised a wedge model to conduct a mesh sensitivity study in a similar nature. The element size was decreased for every iteration of the blast. The results from the varying elements sizes were compared to each other and to a theoretical approach suggested by Kinney and Graham [17].

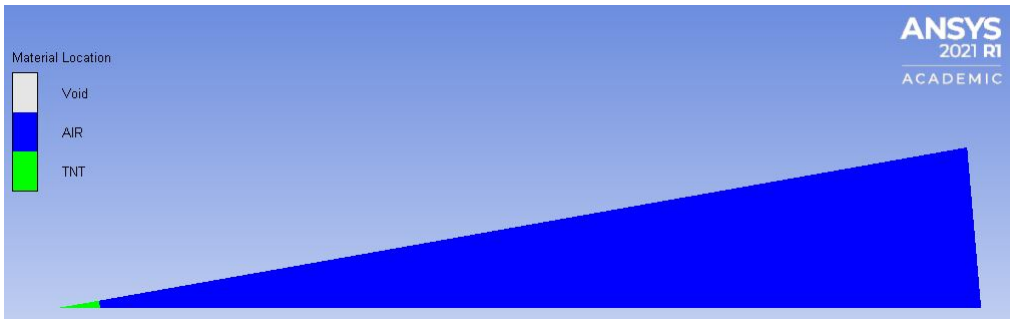

Figure 5.1 Photo from of an axial symmetrical wedge blast set-up that was used to vary the mesh size for the mesh convergence study in AUTODYN.

Figure 5.2 shows that as the mesh was refined, the simulated pressure converged towards the result predicted by Kinney and Graham (Equation 5.1).

$$P(t) = P_{max}(1 - \frac{t}{t_d})e^{\frac{\alpha t}{e^t d}} \tag{5.1}$$

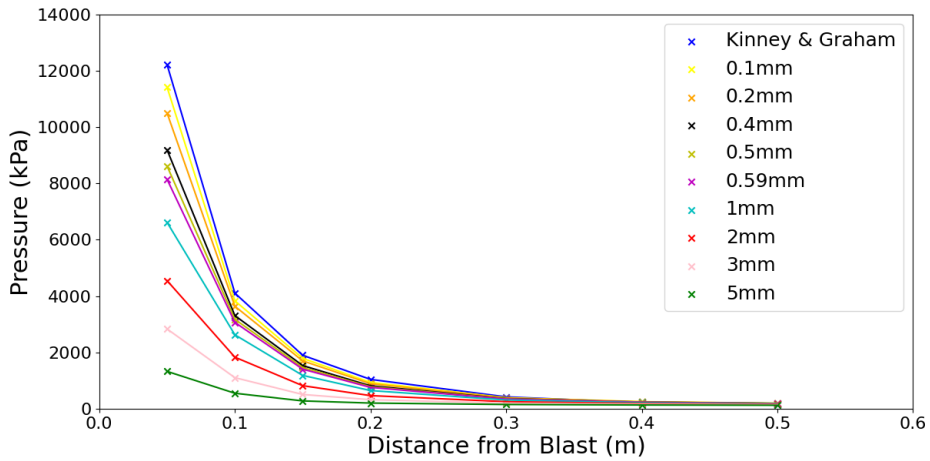

Figure 5.2 Graph comparing the pressure recorded at various distances from detonation with varying mesh sizes.

Figure 5.3 shows that elements larger than $0.5mm$ showed a significant change in simulated pressure as the size of the elements increased. Elements smaller than $0.2mm$ showed minimal change in simulated pressure, but took much longer to complete the simulation. The times recorded from the mesh convergence study would be exponentially

smaller than for the numerical simulations conducted for the actual experiments due to the complexity of the simulation.

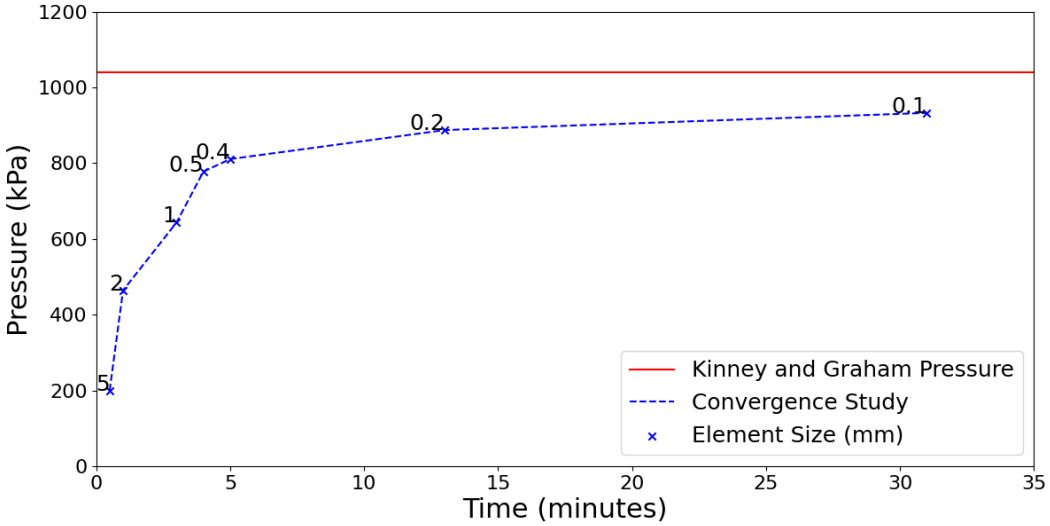

Figure 5.3 Graphical representation of the pressure recorded compared to the time taken to complete the simulation at 0.2m from detonation.

Table 5.1 *Table listing the data fathered from the convergence and displayed in Figure 5.3.*

Element Size (mm)	**Time (min)**	**Pressure (kPa)**	**Percentage Pressure of Maximum Pressure**
5	0.5	199.54	21.39
2	1	464.02	49.74
0.5	4	778.09	83.40
0.2	13	887.56	95.14
0.1	31	932.91	100

In computational work, there is always a compromise between accuracy of experiments and run time. For this reason, a $0.4mm$ mesh size was selected to perform the numerical simulations. As shown in Table 5.1, the $0.4mm$ size allowed for results to be validated

using the experiments with minimal variation in pressure while being completed within a reasonable time.

5.2 Model Description

A two-dimensional axisymmetric model was used in the simulation, to exploit the cylindrical geometry of the experiments and save computational costs associated with 3D simulations. The simulation geometry was similar to that of the experiments, with appropriate boundary conditions. Gauge points at key locations were generated to capture key features such as pressure and displacement. Figure 5.4 shows the simulation set-up.

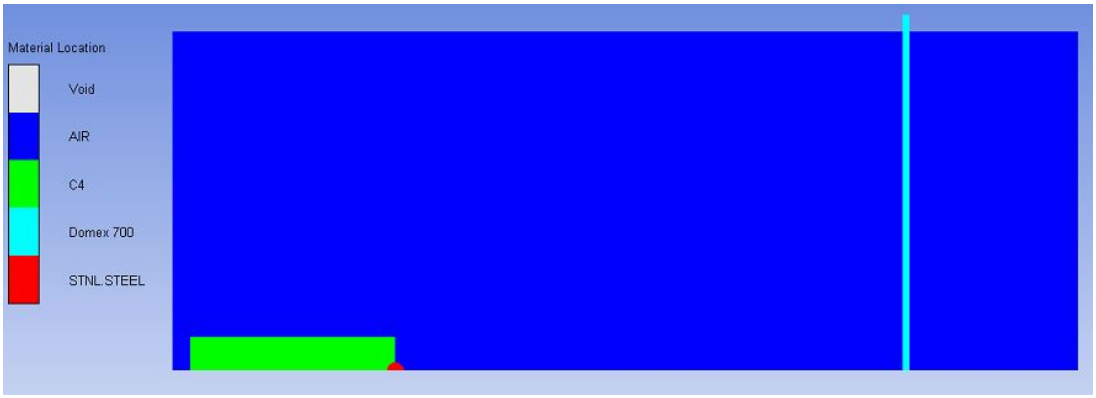

Figure 5.4 Illustration taken from AUTODYN depicting the Numerical Set-Up.

5.3 Model Set Up

The air was modelled by creating a block to encompass the charge, SOD and target target plate used in the experiments. The air block had a consistent height of $100mm$ but varied in length depending on the length of the charge used, but ranged from $248mm$ to $339mm$, accounting for the length of the charge, the $150mm$ SOD as well as additional space behind the target plate to account for any deflections the target plate might have experienced. The part was created with the $0.4mm$ element size with an Eulerian mesh.

The C-4 was modelled as a rectangle, $10mm$ in height and ranging from $41mm$ to $122mm$ in length depending on the required charge size, using the fill feature in AUTODYN. The

fill feature meant that a certain space in the air mesh was designated as explosive and those elements were filled with C-4 material and its corresponding properties, ensuring the explosive was modelled with an Eulerian mesh.

The Domex 700 target plate was modelled by placing a separate Lagrangian part onto the air mesh. The element size for the Domex target plate was also set to $0.4mm$. The target plate had a height of $105mm$ and length of $2mm$. The height of the target plate was greater than the height of the air block by $5mm$. This allowed for the target plate to have boundary conditions placed on the protruding part of target plate to replicate the clamping set up used in the experiments.

The ball bearing was implemented into the numerical set-up in a similar way to the Domex target plate, as a Lagrangian part placed onto the air mesh. The bearing initial position varied in placement according to the experiment being simulated. The set-up was modelled as a half circle, $5mm$ in diameter with a mesh size of $0.4mm$, on the symmetric axis.

The simulation was run using a coupled Lagrangian-Eulerian solver to allow for interaction between the two mesh types. The detonation point was placed at the rear end of the charge. Gauge points were added in a grid pattern in the air to measure pressure at various strategic points in the mesh. Moving gauge points were also added to the bearing and target plate in various places to track the displacement and velocity of these parts.

5.3.1 Boundary Conditions

5.3.1.1 Flow Out Boundary

The flow-out boundaries in the model allowed for the pressure and material to escape out of the simulation area. The flow out boundary replicated how the blast wave and gases escaped to the room via the open ends of the tube. The thick steel tube and clamps had minimal deflection under experimental blast loads. The tube was therefore modelled as a

reflective boundary to contain the pressure waves and material flow within the simulation domain. These boundaries are shown by the orange and green lines shown in Figure 5.5.

5.3.1.2 Constant Velocity Boundary

To mimic the clamp that holds the target place in place, constant velocity boundaries with a value of zero were added to the plate edge outside of the reflective boundary. The constant velocity boundary is shown by the yellow lines in Figure 5.5.

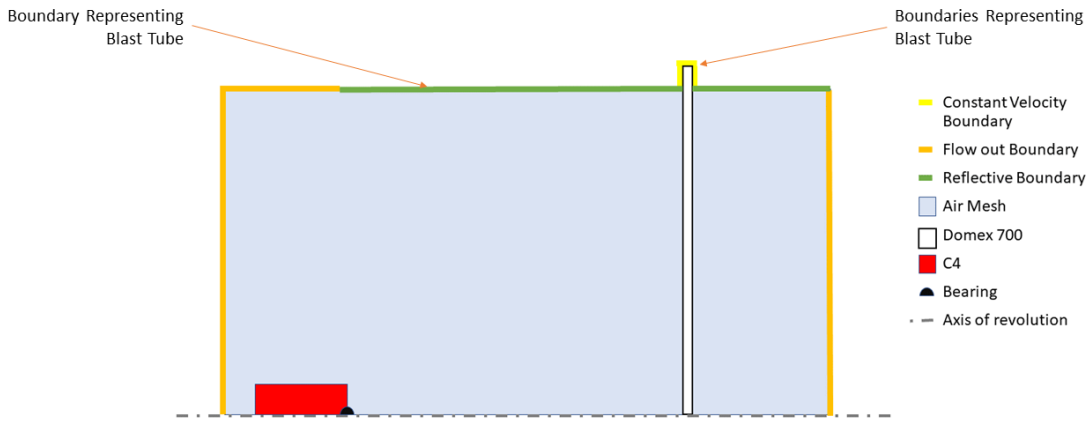

Figure 5.5 Schematic of the simulation layout highlighting the boundary conditions and material locations.

5.3.2 Material Models

5.3.2.1 Air

The air mesh was assigned the ideal gas Equation of State (EOS), shown in Equation 5.2.

$$PV = nRT \tag{5.2}$$

To replicate the experiments as much as possible, the initial conditions were set to 25°C at 1 bar pressure. The parameters used to describe the properties of are were provided by the Autodyn library [85] and are listed in Table 5.2.

Table 5.2 *Table listing the material properties of air from [85].*

Property	**Value**
Density (g/cm^3)	0.001225
γ	1.4
Specific Heat (J/kgK)	717.6

5.3.2.2 Explosive

The expansion of air due to the detonation of the PE4 charge was modelled using the Jones-Wilkins-Less, Equation 5.3, Equation of State (JWL) (EOS) for C4 explosive.

$$P = A(1 - \frac{w}{R_1 V})e^{-R_1 V} + B(1 - \frac{w}{R_2 V})e^{-R_2 V} + \frac{wE}{V} \tag{5.3}$$

Even though PE4 explosive charge was used during the experiments, there are many cases shown where C4 and PE4 are interchangeable and show very similar results [36, 86, 87]. Bogosian *et al.* [87] stated that C4 and PE4 are similar in structure. Both are composed of the chemical compound RDX, or hexogen, mixed with a plasticiser in slightly different proportions: 91% RDX for C4 and 88% RDX in PE4. Bogosian *et al.* [87] conducted experiments to determine how both plastic explosives compare to equivalent TNT mass. Both explosives have an equivalence of 1.2 for both pressure and impulse. The C4 model can therefore be used to approximate PE4 with minimal variation. The properties of the C4 charge were taken from the Autodyn material library [85], and are listed in Table 5.3.

Table 5.3 *Table listing the material properties of C4 from [85].*

Property	**Value**
Density (g/cm^3)	1.601
Parameter A (MPa)	6.1x10^5
Parameter B (MPa)	1.3x10^4
Parameter R1	4.5
Parameter R2	1.4
Parameter ω	0.25
C-J Detonation velocity ($m \cdot s^{-1}$)	8190
C-J Energy/Unit Volume	9.0x10^6
C-J Pressure	2.8x10^7

5.3.2.3 Domex 700 Target Plate

The Domex 700 target plates were modelled using the Johnson-Cook strength model as described by Johnson-Cook [88],

$$\sigma = [A + Be_p^n][1 + Cln(\frac{\dot{e_p}}{\dot{e_o}})][1 - (T^*)^m] \tag{5.4}$$

Where σ is the stress response, e_p and $\dot{e_p}$ are the equivalent plastic strain and strain rate, $\dot{e_o}$ is the normalising reference strain rate, A and B are the strain hardening parameters, C is a dimensionless strain rate hardening coefficient and parameters n and m are the exponents for the strain hardening and thermal softening terms. T^* is a normalised temperature. Domex 700 steel was not listed in the AUTODYN materials library. The parameters used to describe the target plate were taken from Pickering [81] because the material were only ordered after simulations were carried out and Pickering had determined the Domex 700 values for the Johnson-Cook equation in previous research. The differences in the yield stress was minimal, with the yield stress of the Domex sheets as 746.674MPa (later obtained via tensile test), and the value used by Pickering was listed as 795.86MPa. This was a 6.17% difference in yield stress.

Table 5.4 *Table listing the material parameters of Domex 700 from [81] and the Tensile Tests.*

Property	**Value used in Numerical Simulation [81]**	**Value determined from Tensile Tests**
A (MPa)	795.86	746.67
B (MPa)	397.80	245.73
n	0.48	0.487
C	0.014	0.0322
T_{melt} (K)	1793	1793

Once the results from the tensile tests were determined, values determined from the tests are listed in Table 5.4, a simulation was conducted to compare the difference in responses between the material properties obtained from Pickering and the tensile tests. From these simulations, the differences in final deflection are presented in Table 5.5.

Table 5.5 *Table listing the difference in final deflection of the two Domex Plates.*

Gauge	Deflection (mm)		Difference (mm)
	Material based on the values from Pickering [81]	Material based on the values from Tensile Tests	
1	7.45	7.5	0.05
2	7.05	7.12	0.07
3	6.95	7.02	0.07

Comparing the differences in the response of the plates for the different material properties, it was determined that the difference in response was marginal. The simulations conducted using the values obtained from Pickering [81] were therefore assumed to show a good correlation. These results could be validated against the experiments.

5.3.2.4 Stainless Steel Ball Bearing

The ball bearing used to represent the shrapnel in the experiments was made from martensitic stainless steel AISI 420C (X46Cr13) as described by Qi *et al.* [61]. The closest material available in the Autodyn library [85], being the generic "stainless steel", was used to model the ball bearing, as implemented by Qi *et al* [61]. The Johnson-Cook strength model was used to model the ball bearing. The values used in the simulation for the stainless steel ball bearing are listed in Table 5.6.

Table 5.6 *Table listing the parameters used to describe stainless steel in numerical simulations [61, 85]*

Equation of State/Strength Model	Property	Value
Shock	Density(g/cm^3)	7.86
	Gruneisen Coefficient	1.67
	Parameter C1 ($m \cdot s^{-1}$)	4610
	Parameter S1	1.73
Piecewise Johnson-Cook	Shear Modulus (GPa)	73
	Yield Stress (MPa)	689
	Effective Plastic Strain #1	0.3
	Yield Strength #1 (GPa)	1
	Strain Rate Constant	$4.37 \text{x} 10^{-3}$
	Thermal Softening Exponent	1.00
Grady Spall Failure Model	Critical Strain Value	1.3
Geometric Erosion	Erosion Strain	2
	Type	Instantaneous

5.3.3 Simulation Plan

Table 5.7 shows the simulations that were completed while describing the placement of each of the ball bearings. The ball bearings had six placements throughout the charge length for different charge sizes. The ball bearings were placed at different percentage depths into the charge, measured from the centre of the ball bearing to the circular side facing towards the target plate. The exception to this was placement 2 which always had the surface of the ball bearing tangential to the circular side that faced towards the target plate, effectively always being $2.5mm$ into the ball bearing. The percentage depths are listed in Table 3.3.

Table 5.7 *Table describing the depth of each ball bearing along the cylindrical axis.*

Charge Size			Depth of ball bearing along cylindrical axis from side facing the target plate (mm)						
			ball bearing Placement						
Mass (g)	Diameter (mm)	Length (mm)	0	1	2	3	4	5	6
10	20	20.27	No ball bearing	0	2.5	4	6	8	10
20	20	40.55	No ball bearing	0	2.5	8.2	12.3	16.4	20.5
30	20	60.82	No ball bearing	0	2.5	12.2	18.3	24.4	30.5
40	20	81.1	No ball bearing	0	2.5	16.2	24.3	32.4	40.5
50	20	101.37	No ball bearing	0	2.5	20.2	30.3	40.4	50.5
60	20	121.65	No ball bearing	0	2.5	24.4	36.6	48.8	61

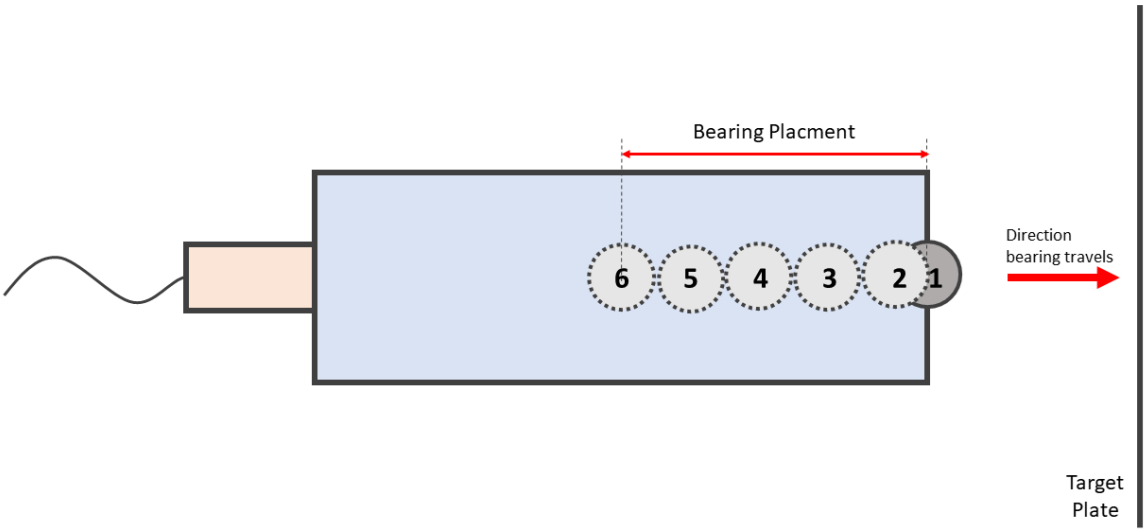

Figure 5.6 Sketch showing the different placements for each ball bearing for each charge. For ball bearing placement calculations, refer to Table 3.3.

Chapter 6

Simulation Results

This chapter presents the simulated blast results, examining aspects such as the pressure waves, ball bearing velocity and final deflection of the plate. The simulations completed for this dissertation were to validate the experiments and to gain further insight. A parametric study was carried out to investigate the response of a target plate exposed to the combined loading, where the depth of a ball bearing varied in a cylindrical charge of constant diameter and varying length.

6.1 Table of Results

Table 6.1 summarised key results obtained from all the simulations, namely: final deflection of the target plate, the impact velocity of the ball bearing as it impacted the target plate as well as the maximum pressure experienced $1mm$ in front of the target plate. In Table 6.1, DNR was placed in the impact velocity column to indicate when the ball bearing did not reach the target plate as the impact velocity when discharged from the explosive was too low.

Charge Size (g)	**Ball bearing Placement**	**Ball bearing Depth** (mm)	**Maximum Pressure** (MPa)	**Ball bearing Impact Velocity** ($m \cdot s^{-1}$)	**Final Deflection** (mm)
10	0	N/A	161	N/A	2.87
	1	0	133	598	5.50
	2	2.5	129	469	4.41
	3	4	168	243	3.17
	4	6	165	67.2	3.53
	5	8	145	DNR	1.09
	6	10	144	DNR	0.52
20	0	N/A	62.4	N/A	5.29
	1	0	148	680	8.67
	2	2.5	149	555	8.35
	3	8.2	66.2	64.2	4.45
	4	12.3	70.4	26.5	5.35
	5	16.4	66.6	14.1	3.75
	6	20.5	66.3	DNR	5.15
30	0	N/A	104	N/A	7.2
	1	0	125	668	7.8
	2	2.5	139	595	8.87
	3	12.2	147	24.2	7.57
	4	18.3	122	15.5	7.58
	5	24.4	151	12.8	7.74
	6	30.5	141	7.50	7.58
40	0	N/A	118	N/A	7.21
	1	0	168	694	8.25
	2	2.5	162	603	9.00
	3	16.2	105	21.7	7.33
	4	24.3	108	17.8	7.64
	5	32.4	108	13.5	7.29
	6	40.5	118	11.2	7.43
50	0	N/A	111	N/A	7.27
	1	0	160	695	8.38
	2	2.5	165	606	9.35
	3	20.2	110	20.7	7.29
	4	30.3	109	19.0	7.57
	5	40.4	108	17.1	7.47
	6	50.5	113	13.8	7.42

Charge Size (g)	Ball bearing Placement	Ball bearing Depth (mm)	Maximum Pressure (MPa)	Ball bearing Impact Velocity ($m \cdot s^{-1}$)	Final Deflection (mm)
60	0	N/A	105	N/A	7.44
	1	0	167	705	8.52
	2	2.5	170	583	9.41
	3	24.4	112	29.6	7.24
	4	36.6	110	19.3	7.48
	5	48.8	110	17.4	7.51
	6	61	106	18.31	7.44

Table 6.1 *Table listing the velocity, pressure and final deflection for all the simulations.*

6.2 Numerical Results of the Pressure acting within the Blast Tube

During the simulation process, the pressure interactions and magnitudes within the blast tube were recorded, as shown in Figure 6.1. During the initial blast propagation, the pressure wave propagated outward from the charge, as show in Figures 6.1(a) to 6.1(c). A clear double wave feature as expected from cylindrical charges was visible. This development of the shock wave demonstrated what Knock *et al.* [33] described. In Figure 6.1(d), a reflective wave is visible reflecting off the blast tube wall. Consequently, a reflected wave built up at the centre of the target plate in Figure 6.1(h).

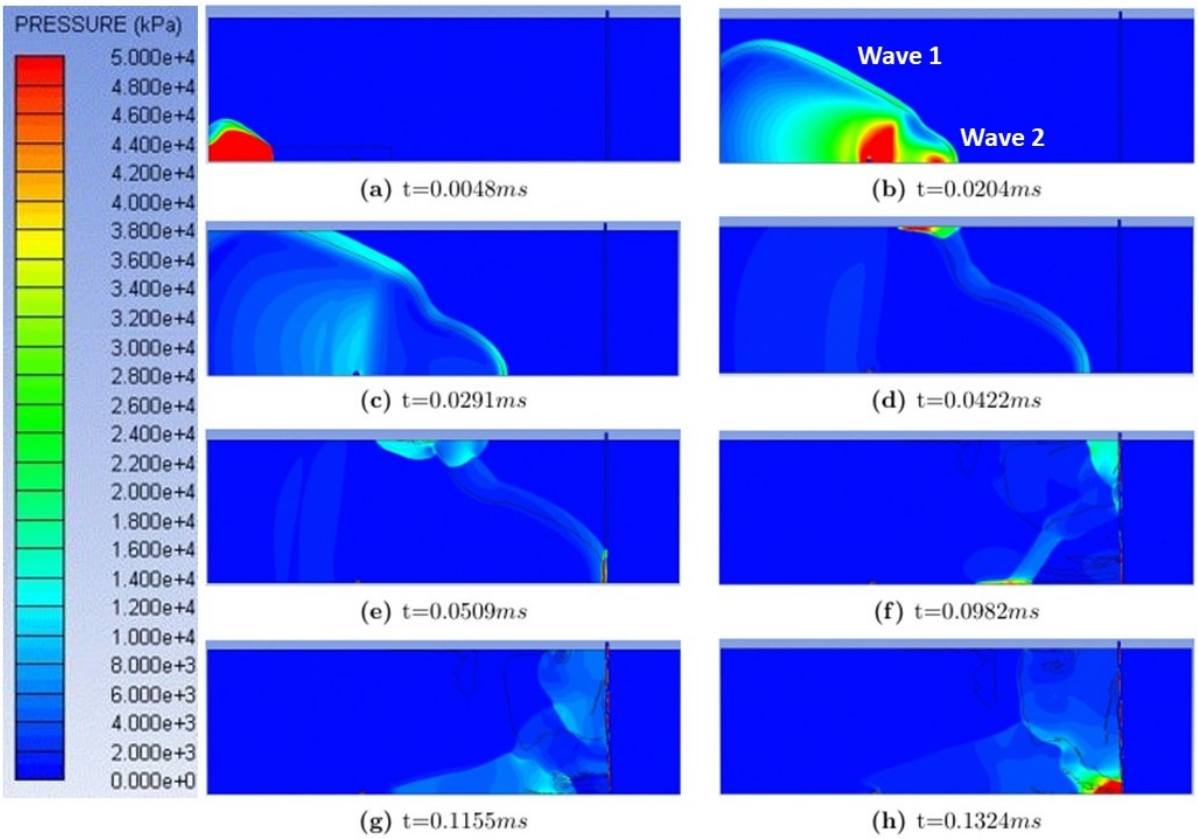

Figure 6.1 Sequence of images taken from AUTODYN showing how the pressure wave and interacted with the ball bearing and target plate for 40g charge over 130 microseconds.

Figure 6.2 describes the pressure $1mm$ in front of the target plate for a $40g$ charge for various bearing placements. The pressure was measured at this location as Autodyn cannot provide a pressure reading on a moving face, such as the face between the target plate and the air. When there was no bearing present, or Placement 0, and when the ball bearing was placed deeper inside the charge, nominally Placements 3 and deeper, pressures of a similar magnitude were observed. When the ball bearing was placed closer to the face of the charge (Placements 1 and 2), the peak pressure observed was greater than the other placements.

Figure 6.3 shows the maximum pressure experienced by the plate for all charge sizes. The $20g$, $40g$, $50g$ and $60g$ charge masses followed a similar trend shown by the $40g$ charge, as shown in Figure 6.3. The $10g$ and $30g$ charges did not follow the same trend as the others. The $10g$ charge peak pressure dropped as the bearing was placed closer to

the end of the charge and then increased in magnitude again as the bearing was placed deeper into the charge. The 30g charge had a steady increase in pressure as the bearing was placed further into the charge till placement 4 and onward when it followed a more inconsistent trend.

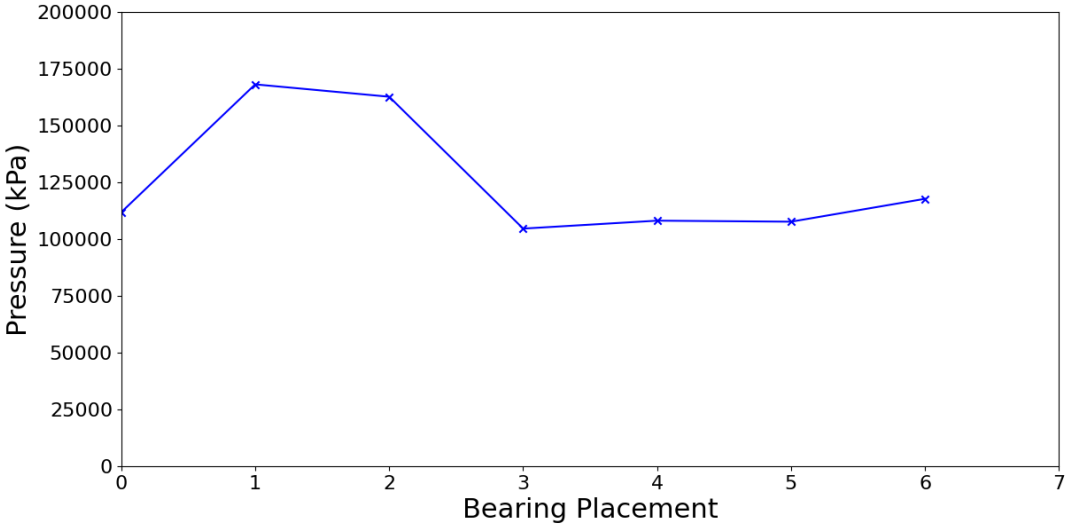

Figure 6.2 Graph comparing the maximum pressure experienced in front of the plate to the different ball bearing locations for the 40g size charge.

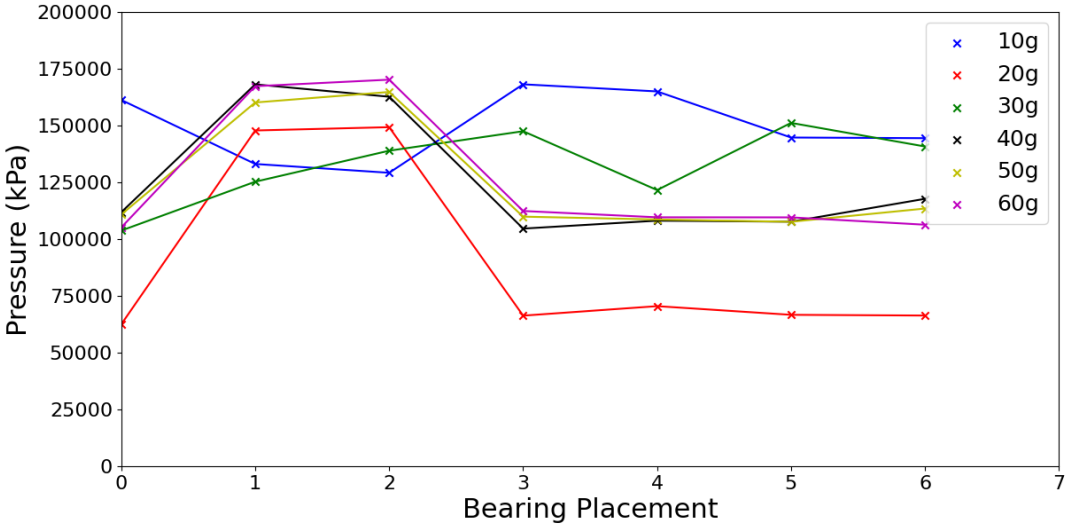

Figure 6.3 Graph comparing maximum pressure experienced in front of the plate to the different ball bearing locations of the various charge sizes.

The inconsistent pressure readings for the 10g charge were suspected to have been caused by ball bearings interaction with the pressure wave when the ball mass to charge mass ratio was below a certain value. When the bearing is at Placement 1 or 2, the ball bearing created an obstacle for the wave to pass. This created a small void behind the ball bearing as the pressure wave passed the ball bearing. Figure 6.4 compares the pressure wave interactions between ball bearings in Placement 1, Figure 6.4a, and Placement 4, Figure 6.4b from a $40g$ charge. Figure 6.4a shows how the pressure waves interacted with the ball bearing in such a way to create an inconsistent wave front in Placement 1, while Figure 6.4b shows how the wave front passed over the ball bearing in a more uniform way, leading to a more uniform wave front heading towards the target plate. The ball bearing in Figure 6.4a deforms more compared to the ball bearing in Figure 6.4b. The uniform loading in Placement 4 results in the loading retaining its shape as the ball bearing has effectively become incompressible compared to the non uniform loading in for the ball bearing in Placement 1.

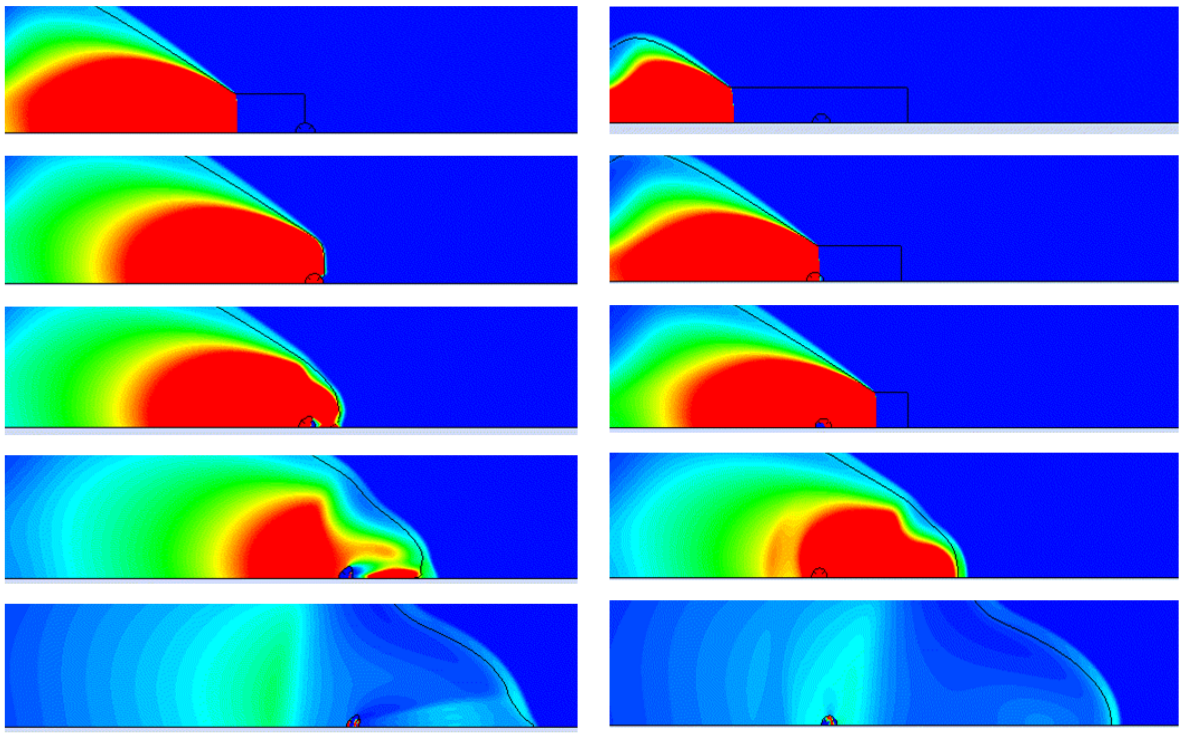

(a) Images from the numerical simulation depicting the interaction of the pressure wave with a ball bearing in Placement 1.

(b) Images from the numerical simulation depicting the interaction of the pressure wave with a ball bearing in Placement 4.

Figure 6.4 Transient response highlighting the pressure waves interaction with the ball bearing.

6.3 Ball Bearing Velocity

The velocity of the ball bearing was greatly influenced by the placement in the charge and the size of the charge. Figure 6.5 shows the maximum velocity, impact velocity and rebound velocity (velocity after the ball bearing has struck the plate and was travelling back towards the detonation point) experienced by the ball bearing for the various placements of the ball bearing in a 40g charge. As the ball bearing was placed further down the charge, the ball bearing experienced a slower impact velocity, with a drastic drop in impact velocity between Placements 2 and 3. The depth of the ball bearing within the cylindrical charge also affected the maximum velocity the ball bearing could achieve. This was clearly visible in Figure 6.5 when the graph flattened out just above zero for Placements 2 and 3, highlighting that for depths of Placement 3 and deeper, the maximum velocity would not be greatly affected. The material characteristics for the failure model were not complete, hence the ball bearing rebounds artificially for higher velocities, instead of both ball and target exhibiting fracture. The investigation of the failure model fell outside the scope of this research so was not investigated further.

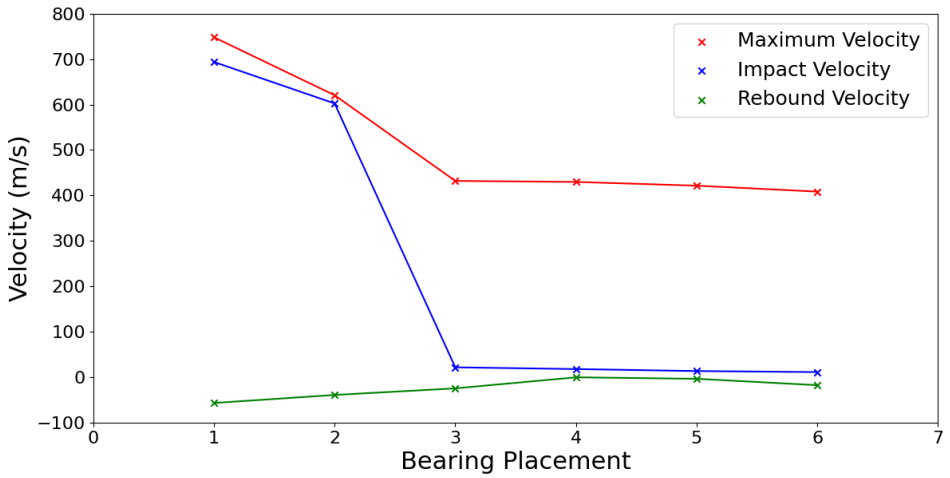

Figure 6.5 Graph comparing the various velocities experienced by the ball bearing for the different ball bearing Placements for the 40g size charge.

Figure 6.6 shows the velocity profiles for the ball bearings in the first four placements in a 40g charge. The profiles showed that the maximum velocity occurred shortly after

detonation, and that a clear impact time, where the velocity dropped drastically, was present. The impact velocity was followed by the rebound velocity as the velocity became negative. As the placements increased the ball bearing got embedded deeper because the placements were based on percentage depth, the charge mass between the bearing and front of the charge increased. As the mass behind the ball bearing reacted, the ball bearing accelerated, but as the mass in front of the ball bearing reacted, the ball bearing decelerated. The charges that had more mass in front of the bearing generated a lower impact velocity as the mass in front of the ball bearing provided a reverse impulse onto the ball bearing, slowing it down. Placements 3 and 4 showed how the ball bearing reached maximum velocity as the pressure wave in the charge passed over the ball bearing but slowed down rapidly as the explosive in front of the ball bearing reacted. The ball bearings never struck the plate in Placements 3 and 4 within $0.5ms$ due to the slower velocity and therefore longer time to travel the same distance.

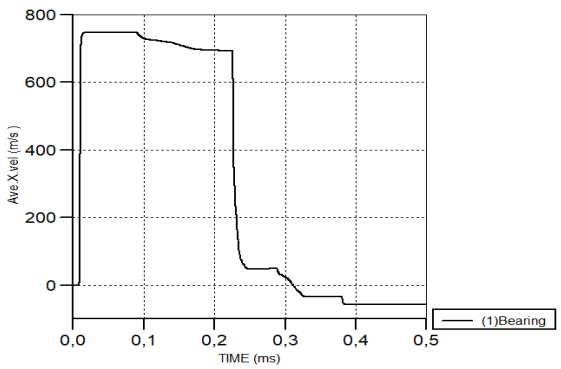

(a) Graph depicting the velocity profile of ball bearing in Placement 1.

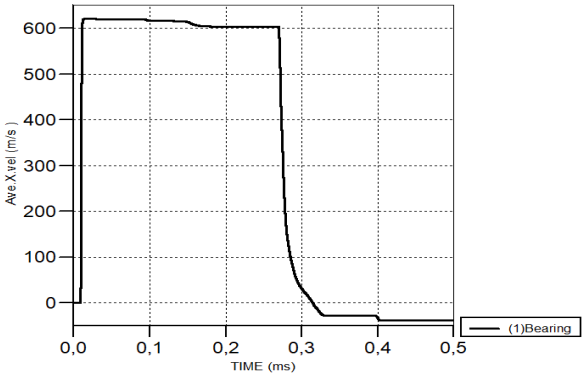

(b) Graph depicting the velocity profile of ball bearing in Placement 2.

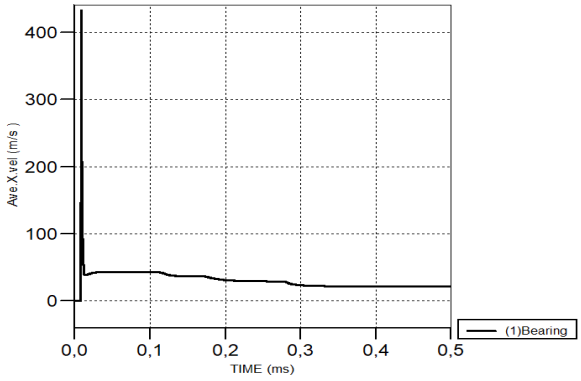

(c) Graph depicting the velocity profile of ball bearing in Placement 3.

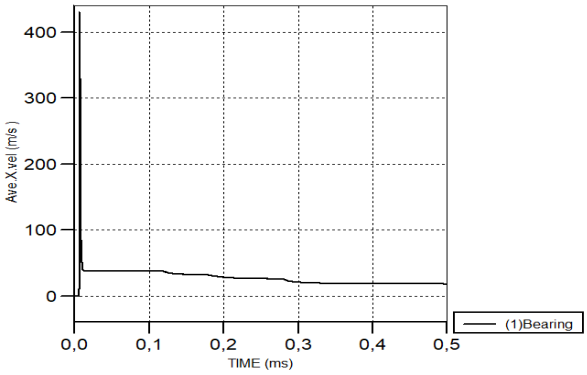

(d) Graph depicting the velocity profile of ball bearing in Placement 4.

Figure 6.6 Graphs showing the ball bearing velocity profiles.

6.4 Deflection of the Target Plate

The combined loading of the blast and fragment caused various deflections of the simulated target plate. The displacement was tracked with the use of three gauges as shown in Figure 6.7. Two gauge points were placed at the centre of the plate, one at the front (Gauge 1) and one at the back (Gauge 2) of the plate. This allowed compression of the plate at the point of impact to be measured as well as maximum deflection. Another gauge was placed $10mm$ above the centre on the front of the plate (Gauge 3) to measure deflection at a slight offset from the centre.

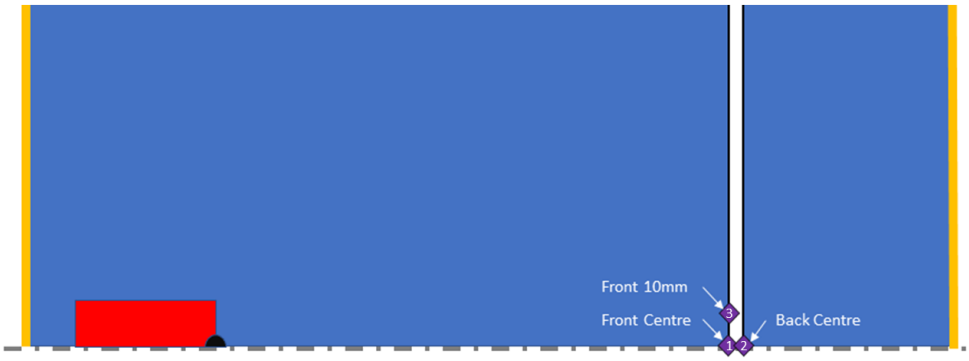

Figure 6.7 Schematic showing the placement of the three gauges in the Domex 700 plate in the numerical simulations in AUTODYN.

A displacement history, as shown in 6.8, was captured from the gauges. It can be observed how the blast pressure wave first interacted with the target plate causing deflection. The plate started to rebound to its original position before the ball bearing impacted the plate at around $0.25ms$ causing further deflection away from the detonation site. When the plate had experienced maximum deflection and the pressure magnitude had significantly decreased, the air mesh around the plate was removed to allow for a shorter simulation time. The plate subsequently oscillated about its final deflection due to inertia. The final deflection was determined as the average of the oscillation.

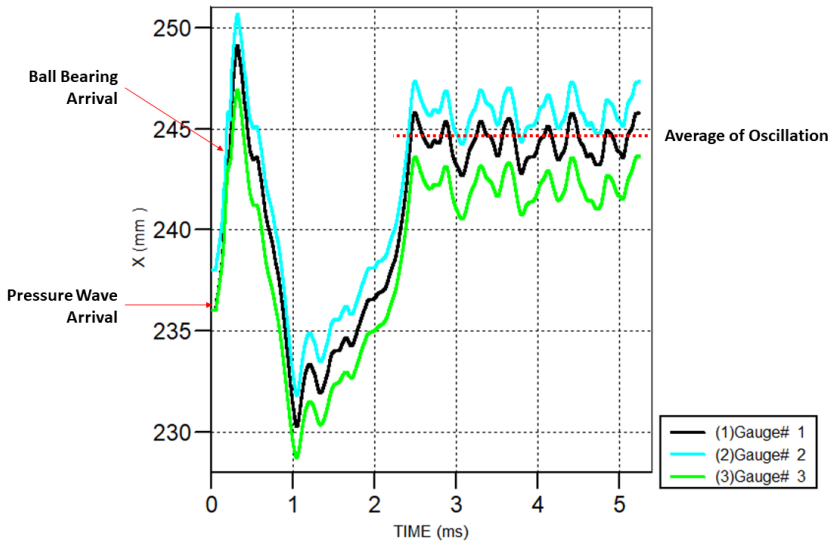

Figure 6.8 Graph showing the deflection history of the 3 gauges. Gauge one is the front centre, two is the back centre and three is the front of the plate, $10mm$ above the centre.

Figure 6.9 shows the overall trends for the final deflection at the point of impact for all the charge sizes and placements of the ball bearings. For the charge masses of $30g$ and above, the deflection indicated a similar trend. The deflection increased as the placement increased from Placement 0 till Placement 2. Thereafter the deflection converged to a value as if no ball bearing was present. The $10g$ and $20g$ charges followed a similar trend. The magnitude of deflection in their cases were however lower. The data showed that the target plates experienced the greatest deflection when the ball bearing was at Placement 2.

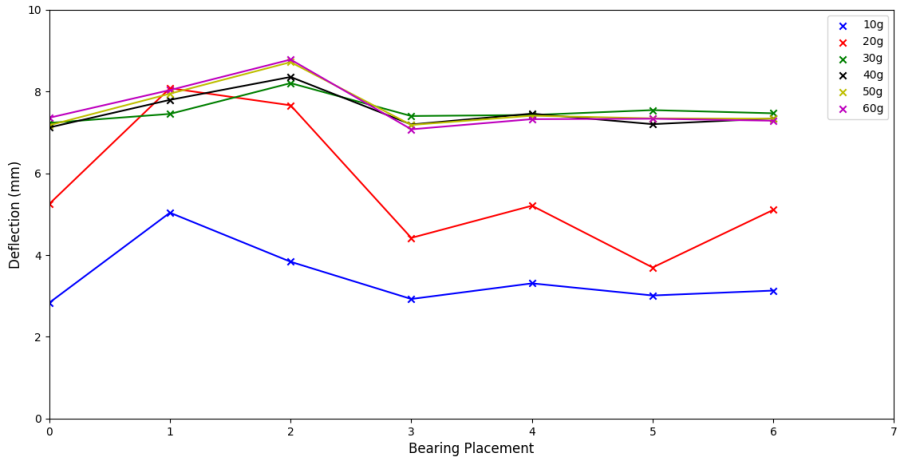

Figure 6.9 Graph comparing the deflection to the placement of the ball bearing for all placements and charge sizes.

Chapter 7

Discussion of Results

7.1 Influence of the Critical Mass on Combined Loading Events

Kennedy [35] showed that the critical length of a cylindrical charge is a function of the diameter, described by Equation 7.1. Qi *et al.* [61] also observed this phenomenon.

$$L_{critical} = D \cdot \sqrt{3}/2 \tag{7.1}$$

Where D is the charge diameter, and $L_{critical}$ is the critical length of the cone as shown in Figure 7.1. The critical volume is illustrated as the highlighted triangle in Figure 7.1 and defined as the mass of charge that lies within the cone created by the critical length.

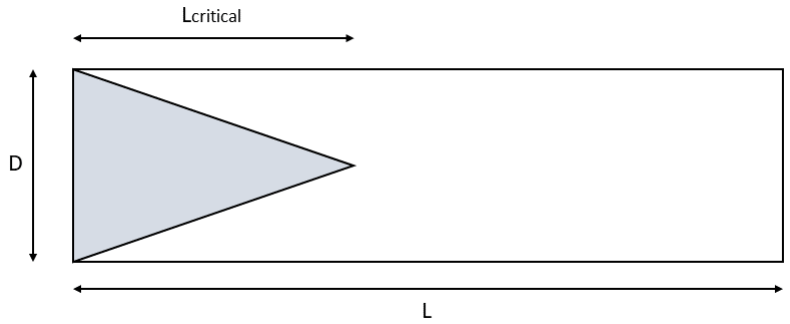

Figure 7.1 Diagram of a cylindrical charge highlighting the critical length.

The critical mass of a charge subsequently played a key role in the outcome in many aspects of combined loading events. All forward impulse from a cylindrical charge should be generated from within this triangle, or critical mass. For charge that is $20mm$ in diameter, as it was for experimental and computational research in this study, the critical length of a charge was $17.32mm$. The smallest charge had a mass of $10g$ and a length of $20.27mm$, showing that all charges had the same critical mass present as all the charges were longer than the critical length for a $20mm$ diameter charge.

7.1.1 Effect of Critical Mass on the Impact Velocity of the Ball Bearing

Due to the ball bearing placement being a percentage of length of the charge rather than set depths, the velocity for the various placements for the different charge sizes could not be compared directly. The ball bearing placement in terms of depth in millimetres fluctuated as the mass fluctuated. The placements were converted to depth in millimetres, listed in Table 7.1 and shown graphically in 7.2, to investigate the ball bearing velocity based on the depth of the ball bearing in a charge. When the ball bearing was placed beyond the critical length of the charge, no substantial difference in impact velocity was observed, as listed in Table 6.1. This could be due to the symmetrical loading on the ball bearing as the loading behind the ball and in front of the ball were consistent when the ball bearing was beyond the critical depth.

Table 7.1 *Table listing the results from the numerical simulations showing the ball bearing velocity and depth of the ball bearing. Ball Bearing Placements outside 17.32mm (critical length) were not listed.*

Charge Size (g)	Placement	Depth (mm)	Velocity ($m \cdot s^{-1}$)
60	1	0	705
60	2	2.5	583
60	3	24.4	29.6
50	1	0	695
50	2	2.5	606
50	3	20.2	20.7
40	1	0	694
40	2	2.5	603
40	3	16.2	21.6
40	4	24.3	17.8
30	1	0	668
30	2	2.5	595
30	3	12.2	24.2
30	4	18.3	15.5
30	5	24.4	12.8
20	1	0	680
20	2	2.5	555
20	3	8.2	64.2
20	4	12.3	26.5
20	5	16.4	14.1
20	6	20.5	N/A
10	1	0	598
10	2	2.5	469
10	3	4	243
10	4	6	67.2
10	5	8	N/A
10	6	10	N/A

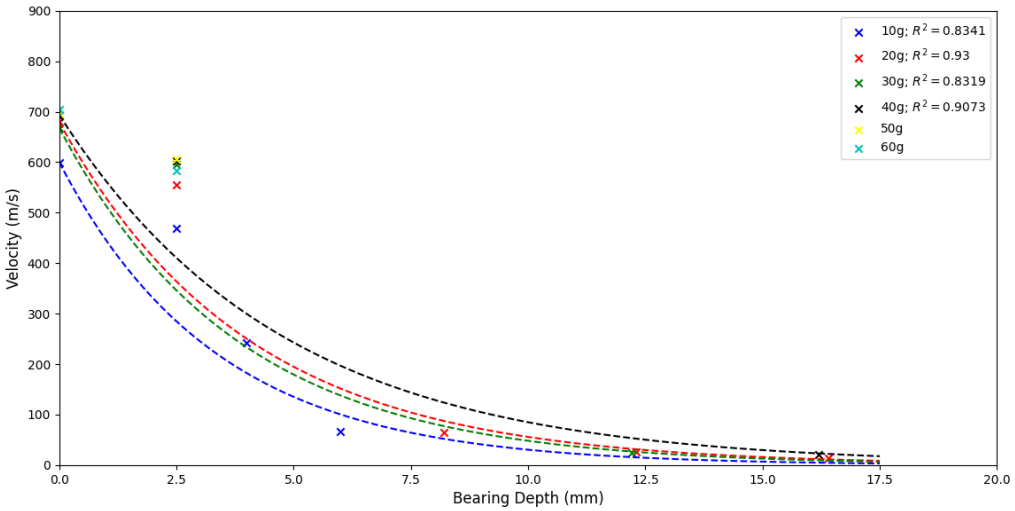

Figure 7.2 Graph showing the variation of the ball bearing velocity compared to the depth of the ball bearing in the charge from the numerical simulations. Note that the $50g$ and $60g$ charges did not have a trend line plotted due to the lack of points gathered.

The trend between ball bearing depth and ball bearing impact velocity, as plotted in Figure 7.2. As the bearing was embedded deeper into the charge, the impact velocity decreased exponentially. It should be noted that the charge size also had an impact. An increase in impact velocity was observed for charges larger than the critical length of the charge, suggesting that any charge mass outside of the critical volume still contributed to the impact velocity of the ball bearing. The data showed that at Placement 2 ($2.5mm$ from the charge end) the impact velocity was higher than the assumed trend due to the ball bearings interaction with the blast pressure wave within the charge. The deflections recorded for ball bearings placed at that depth showed a significant increase in impact velocity when compared to the trend of the data.

7.1.2 Deflection of the Target Plates

7.1.2.1 Comparison of Numerical Deflections to Experimental Deflections

Table 7.2 lists the data comparing the global deflection obtained from the numerical simulation and the experiments. The data from those experiments did not include a cap

deflection. These data points were therefore excluded from the average. Figure 7.4 shows the data from the $10g$ experiments. The numerical data was plotted for all placements.

Table 7.2 *Table listing global deflection between the numerical and experimental results. The average difference between the results is also shown. '*' indicates the ball bearing penetrated the target plate in that experiment.*

Charge Size(g)	Ball Bearing Placement	Numerical Deflection (mm)	Experimental Deflection (mm)	Difference (mm)
30	0	7.23	6.67	-0.57
30	1	4.45	7.02*	-0.43*
30	2	8.20	8.98	0.78
30	3	7.40	6.41	-0.99
30	3	7.40	6.67	-0.74
20	0	5.25	5.3	0.05
20	1	8.08	5.96*	-2.12*
20	2	7.66	8.17	0.51
20	3	4.30	5.22	0.91
10	0	2.83	3.07	0.24
10	1	5.04	5.44	0.40
10	2	3.84	5.50	1.67
10	3	2.92	3.56	0.63
Average Difference (mm)				0.26

In general, the data showed a good correlation between the numerical simulations and the experiments shown in Figure 7.4. The greatest deflections were recorded at Placements 1 and 2. As the ball bearing was placed deeper into the charge the deflection converged to the same deflection as if no ball bearing was embedded in the charge (Placement 0).

This observation is highlighted in Figure 7.3. A larger variation in deflection obtained between the numerical simulations and experiments was observed when the ball bearing was blast driven from Placement 2. The difference in deflections was within a plates thickness ($2mm$) suggesting that the numerical simulations were acceptable.

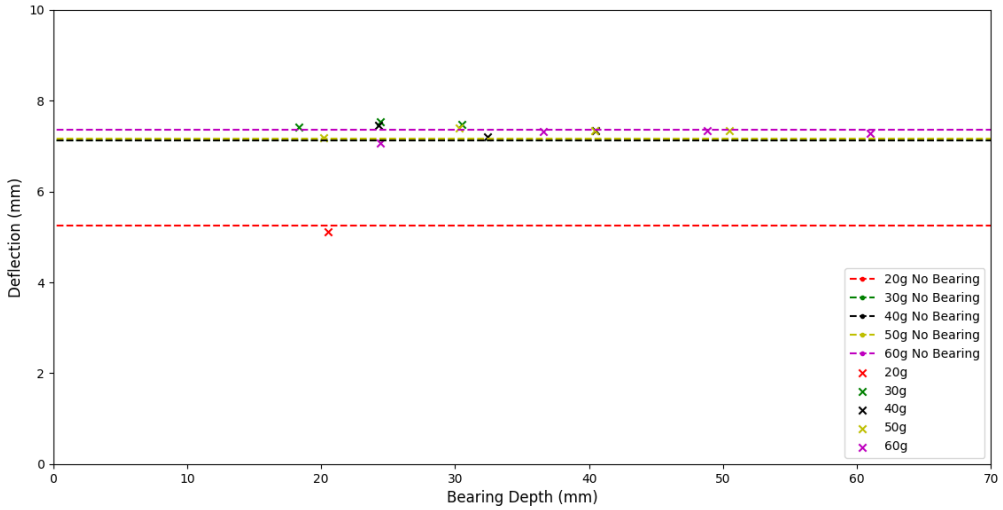

Figure 7.3 Graph comparing the deflection for various charge sizes to the ball bearing depths along the cylindrical axis when placed outside the critical length.

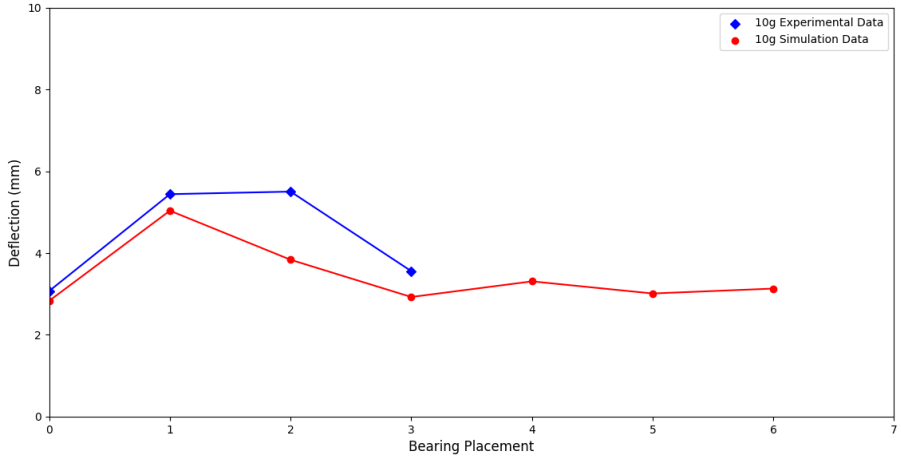

Figure 7.4 Graph comparing the numerical and experimental deflection for the $10g$ charges.

The deflections measured from the 20g charges are presented in Figure 7.5. The data showed a similar pattern to that of the 10g data. The difference between experimental and numerical deflections were once again minimal. The larger variation was observed when the ball bearings were at placement 1. The ball bearing penetrated the target plate in the experiments, denoted by a diamond with a black outline in Figure 7.5. Penetration did not occur in the numerical simulations as expected because the failure model for the Domex 700 was not correctly implemented. The penetration in experiments meant that the plate did not exhibit a cap deflection on the target plate where the ball bearing impacted the plate. The lack of a cap deflection reduced global deflection of the plate, hence the difference in deflections. Figure 7.6 shows the data for the 30g charge data, for both the numerical and experimental work. The data exhibited a similar trend to that of the 20g and 10g data, with placement 1 in the experimental data having less deflection due to the ball bearing penetrating the target plate, as with the 20g experiment.

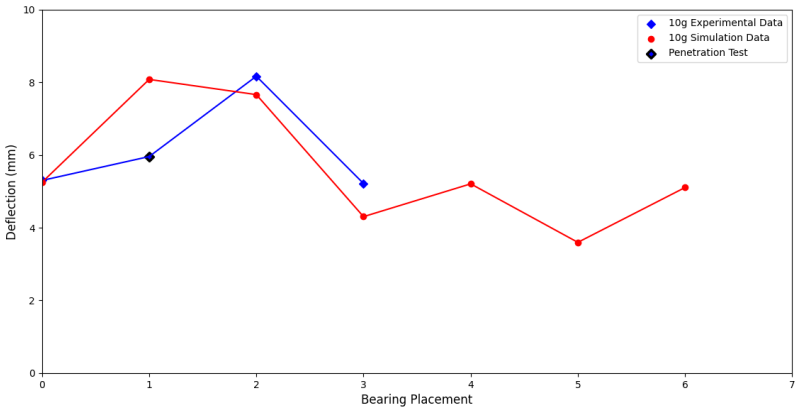

Figure 7.5 Graph comparing the numerical and experimental deflection for the 20g charges.

The overall trends between numerical and experimental work showed a very good correlation for deflection, validating the numerical model. The data also highlighted that the greatest deflection occurred when the ball bearing was placed at Placement 1. The ball bearing was also more likely to penetrate the plate at Placement 1.

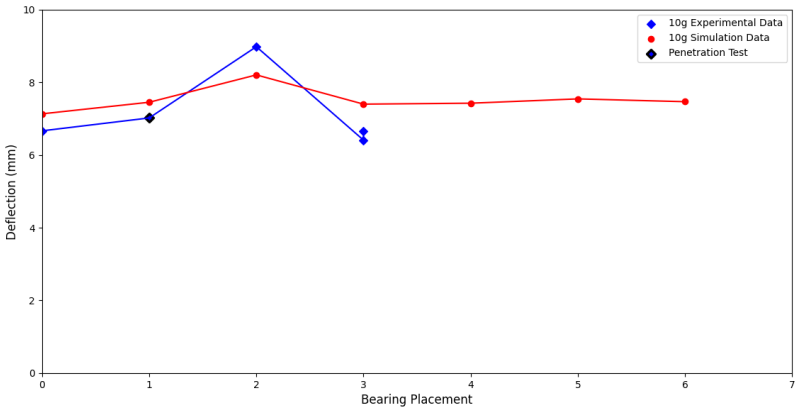

Figure 7.6 Graph comparing the numerical and experimental deflection for the 30g charges.

7.1.2.2 Deflection based on Ball Bearing Depth

Figure 7.7 shows the data comparing the numerical and experimental data obtained for the deflection of the target plate for the different ball bearing placements. Curves were included for the 10g and 20g because there was more experimental and numerical data to formulate a polynomial curve.

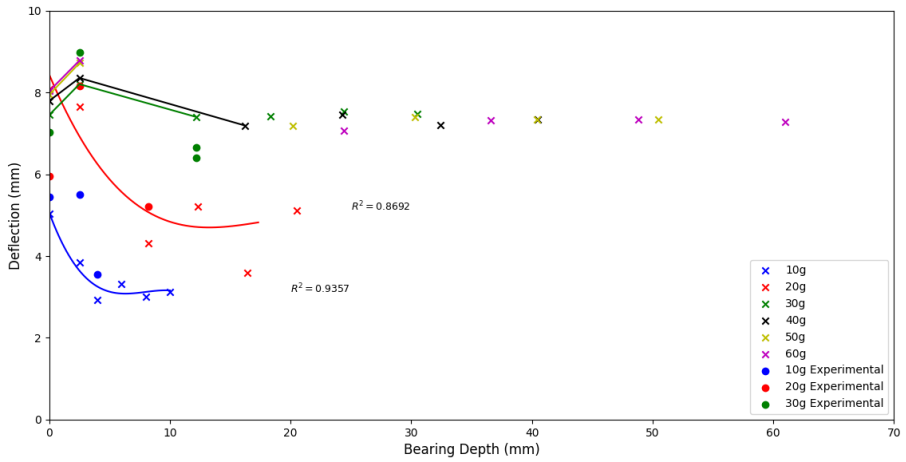

Figure 7.7 Graph showing the final maximum global deflection for various charge sizes and ball bearing depth along the cylindrical axis for numerical and experimental set-ups.

The data showed a clear trend of increasing deflections for increasing charge masses for charge sizes $10g$, $20g$ and $30g$. The ball bearing placement was plotted in actual length (as opposed to percentage depth) to examine how critical length of charge affects the target deflection. When the ball bearing was placed outside the critical length of the charge, the data point was not connected to the graph line. Figure 7.3 highlights how the deflection of embedded ball bearings when placed outside the critical length had little variation in final deflection. The final deflection was similar to the deflections observed when no ball bearing was placed in the charge. The deflections for $10g$ and $20g$ charges were substantially lower than other charge sizes as expected. Maximum deflection of the plate occurred at the Placement 2 (ball bearing centre $2.5mm$ inside the charge from the cylindrical face), as shown in Figure 7.7. The greatest deflection occurred when the ball bearing was buried just within the surface of the charge. Similar observations were made by Kang [21]. It is important to note that for the $30g$ and larger charges, the points were connected with the use of a piecewise line rather than a trend line drawn as with the $10g$ and $20g$ charge. This was due to the lack of data points inside the critical length for those charge sizes. The point plotted with a $16.4mm$ depth and a $3.6mm$ deflection in the $20g$ graph was deemed to be an outlier. This was due to the ball bearing having a low impact velocity which resulted in negligible cap deflection.

7.1.3 Influence of Critical Mass Ratio on the Deflection of a Target from a Combined Loading Event

Figure 7.7 illustrated that the final deflection increased with charge size. This trend was apparent even though all charge sizes were longer than the critical length. This result was not expected as the extra charge mass behind the critical length should not have contributed to the forward impulse that the plates received. Figure 7.8 shows the deflection of a target plate compared to charges with varying critical ratio, which is defined as the ratio of critical mass of the charge to total mass of the charge as described Equation 7.2. The charges had no embedded bearing and had a constant $20mm$ diameter. The critical mass ratio was expressed in percentage on a log scale on the x axis. From Figure 7.8, it was clear that around 10%, there was minimal difference in deflection as the ratio

decreased. As the total mass increased, the deflection also increased until the ratio reached a critical value at around 10%, which equated to a length of 57.7mm for a 20mm diameter charge. The decrease in deflection at this specific critical mass ratio showed that even for charges with excess mass outside the critical volume, the mass still affected the final deflection of the plate, but to a lesser extent than the critical mass. As the total mass increased, the effect of mass outside the critical volume became less significant. This could be a result of the time taken for the blast wave within the charge to propagate enough so the blast wave was parallel to the flat end face of the charge, rather than a curved pressure front, shown in Figure 7.9. A series of simulations were carried out to gain insights into the propagation of the blast waves inside the charge as they travelled down the explosive. The 5g simulated charge, as shown in Figure 7.9a, showed that the blast front wave was still curved (not planar) by the time it reached the end of the charge. For longer charges, as shown in Figure 7.9d, the front was more parallel with the cylindrical face, allowing for a more even detonation of the critical mass when the blast front reached the end of the charge. While this could be due to the numerical code and the interaction between cells, it should be investigated further as explosive waves from charges detonate in a circular fashion. The blast wave propagation within the charge provided some insights into how the critical mass was not the only contributing factor towards the plate deflection. For the 5g charge, the whole critical mass was not detonated at the same time leading to a loss of peak pressure and less deflection.

$$CriticalMassRatio = \frac{Mass_{Critical}}{Mass_{Total}} \tag{7.2}$$

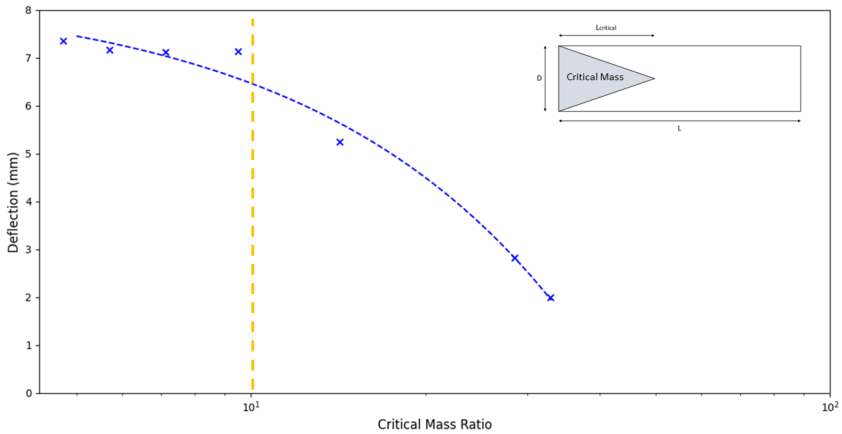

Figure 7.8 Graph comparing the deflection compared to the ratio of critical mass to the total mass of the charge.

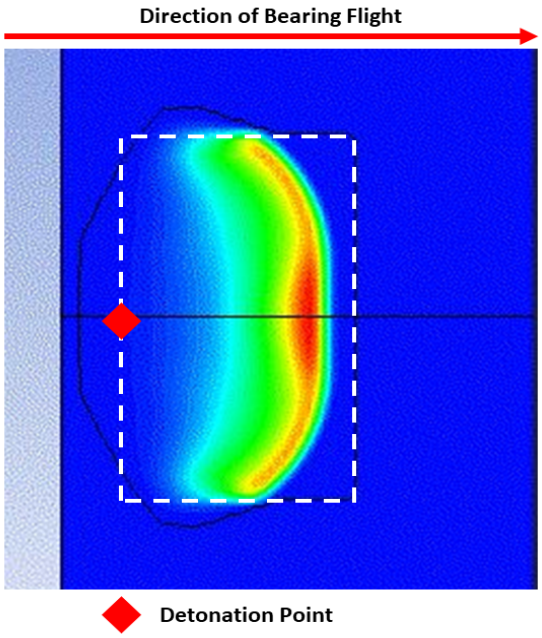

(a) AUTODYN image showing the blast front as it reached the cylindrical face of a 5g charge.

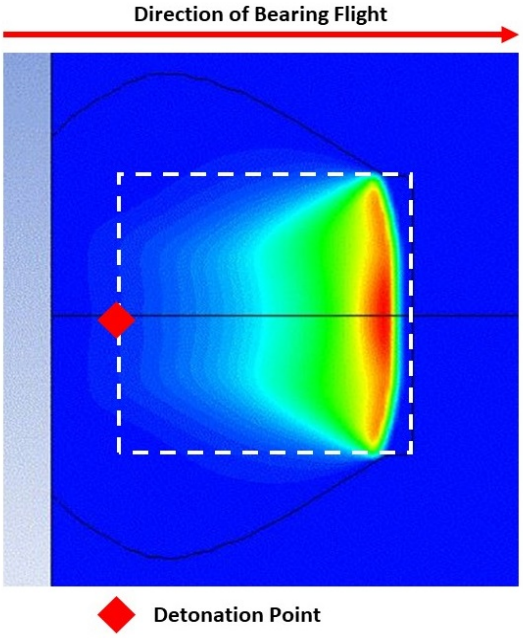

(b) AUTODYN image showing the blast front as it reached the cylindrical face of a $10g$ charge.

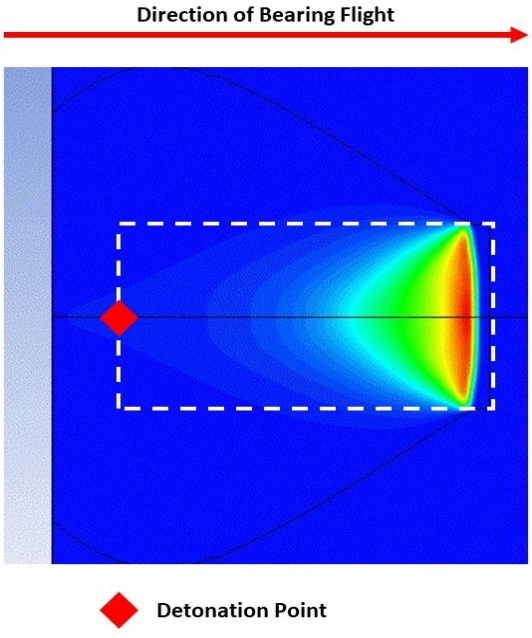

(c) AUTODYN image showing the blast front as it reached the cylindrical face of a $20g$ charge.

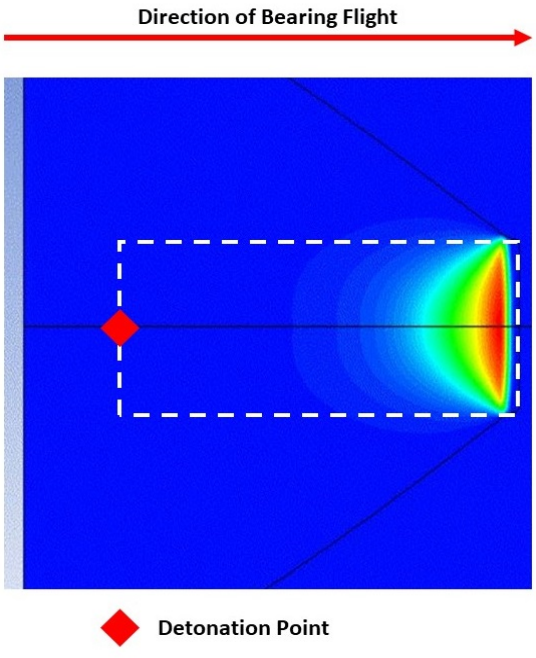

(d) AUTODYN image showing the blast front as it reached the cylindrical face of a $30g$ charge.

Figure 7.9 AUTODYN images showing how the blast wave varied in shape as it reached the end of the charge for different charge lengths.

7.2 Cap Deflection

For the blast-driven ball bearing impact analysis, the velocity had to be inferred from the numerical simulations. However, the variation of the time of impact between the simulations and experiments, as shown in Figure 4.4, was deemed small enough suggesting that any variation in velocity would not be significant. The data comparing blast cap deflections to impact test cap deflections is represented graphically with log graphs in Figure 7.10.

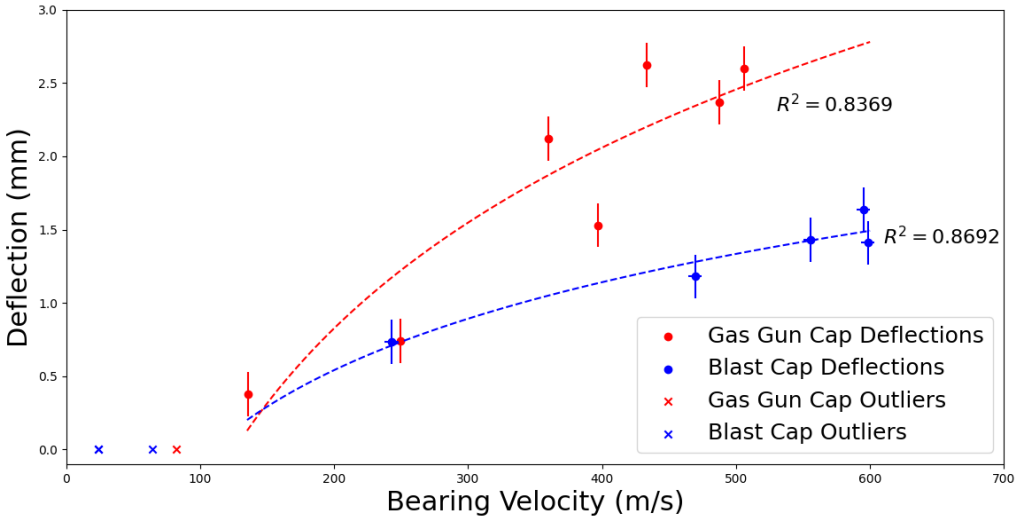

Figure 7.10 Graph comparing the deflection of the cap deflection from projectile impact tests to blast-driven ball bearing impacts.

There was a clear trend showing that the cap deflection obtained from the impact tests were larger than the combined blast and impact loading tests for the same velocity. It was important to note that any ball bearing that produced zero cap deflection had been deemed an outlier as it was unknown what ball bearing impact velocity produced zero cap deflection. A possible reason for the lower cap deflections from blast loading could be because the target plate experienced work hardening from the blast wave prior to the ball bearing impacting the plate. This was possible as the target plate experienced plastic deformation as a result of the blast loading prior to the ball bearing impacting the plate. The time of arrival for the pressure waves can be observed from the data captured by the

Hopkinson Bar for a 20g charge with the ball bearing at Placement 1 (Experiment 4.21.1) in Figure 7.11. The initial and secondary pressure waves arrived at the Hopkinson Bar before the ball bearing impacted the cap.

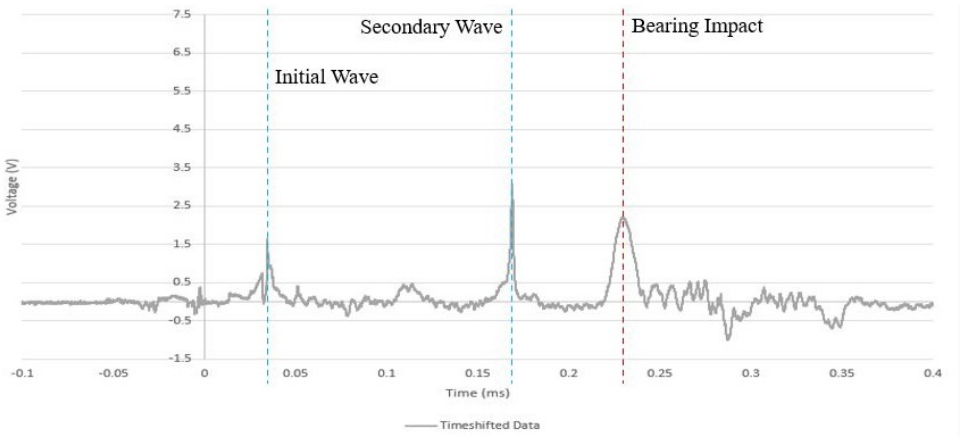

Figure 7.11 Graph showing the data captured from the Hopkinson bar highlight the arrival time of the pressure wave and ball bearing.

The time of arrival of the pressure waves was validated by the pressure history obtained from the numerical simulation, Figure 7.12, where the pressure was measured directly in front of the target plate for a 40g charge. From this data, it was concluded that the target plate had experienced multiple blast waves prior to ball bearing impacting the target plate for all charge sizes. The blast waves work-hardened the target plates, therefore limiting the cap deflection on the target plate.

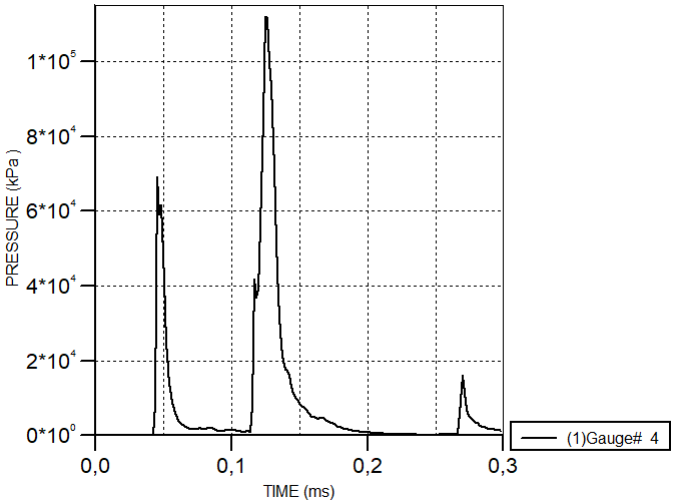

Figure 7.12 Pressure history showing the pressure profile of a $40g$ charge with no ball bearing $1mm$ in front of the target plate in a numerical simulation.

7.3 Investigation of the Sum of the Separate Deflection Types

Several components of the deflection from impact and blast load results were compared, namely the deflection from a blast load with no ball bearing impact, the cap deflection from the blast load (this was done by measuring the area around the cap and then measuring the deflection of the cap), and the global deflection from combined loading.

The various deflections were then obtained from the experiments where the ball bearing was embedded at Placement 2 (just under the surface) for various charge sizes. All the different deflections were plotted in Figure 7.13. Both the global and blast deflection increased with an increase in charge size. The cap deflection did not change substantially as the charge size increased. There was, however, a small increase visible. The difference between the global and cap deflection was calculated by subtracting the cap deflection from the global deflection for the corresponding charge sizes and plotted on the same set of axes. The combination of blast and ball bearing impact loading shows a greater deflection than the sum of the individual blast and combined loading deflections. This

is evident in Figure 7.13 where the graph shows the cap deflection subtracted from the global deflection is greater than the blast loading data. This agrees with the data reported by [72].

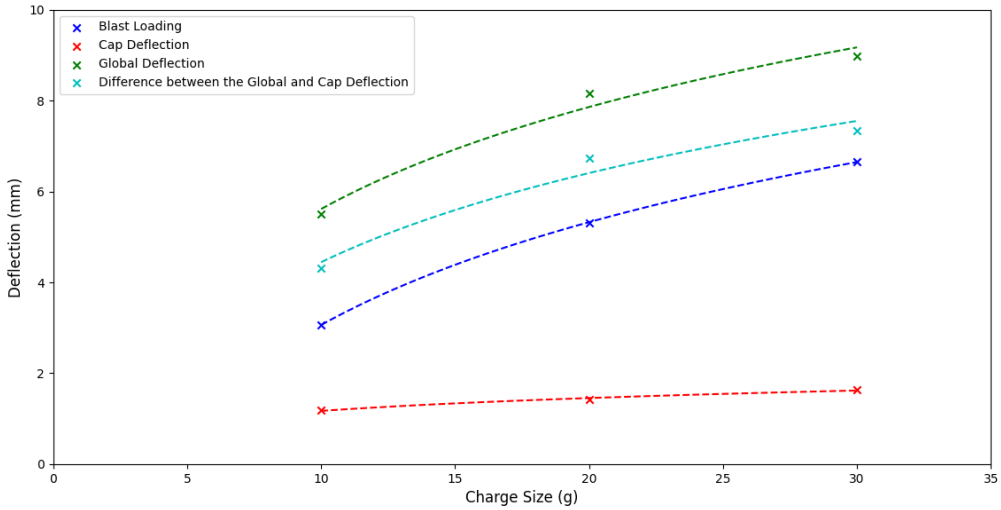

Figure 7.13 Graph showing the deflection breakdown for the various charge sizes with the ball bearing placed at Placement 2

7.4 Summary

- The overall data provided evidence that the ball bearing placement within a cylindrical charge affected the deflection of the target plate as expected. The maximum deflection was likely to happen when the ball was placed just within the charge, or at Placement 2. As the ball bearing was placed further into the charge, the deflection of the target plate decreased with less significant effect at deeper placements.

- The ball bearing was most likely to penetrate the target plate when half buried into the charge, or at Placement 1 due to the higher velocity.

- While all the charges were longer than the critical length of the charge, the plate showed greater deflections as the charge increased in length. When a ratio of critical charge mass to total charge mass was compared to the deflection on a log-scaled graph, it was noticed that at around 10%, the deflection started to show smaller deflections per decrease in the ratio showing that even mass beyond the critical length still affected the deflection of the plate.

- The ball bearing velocity decreased as the ball bearing was placed further down the axis of a cylindrical charge. When the ball bearing was placed beyond the length of the critical mass, the velocity of the ball bearing, once the pressure front had passed the bearing, dropped to such a low velocity that it consequently did not impact the plate.

- The combined blast and impact load showed a greater deflection than the sum of separate ball bearing impact and blast deflections. While this was expected from the literature, it contradicted the experimental result where the cap deflection from the two stage gas-gun impact test was less than the cap deflection from combined and impact tests. So even though the cap deflection from combined blast and impact testing was less than the cap deflection from impact velocity tests, the combined blast and impact loading exhibited greater global deflection.

Chapter 8

Conclusions and Recommendations

8.1 Conclusions

From the findings presented in preceding chapters, it is believed that a better understanding of IEDs, and the coupled effect that a blast and shrapnel loading event as on metal plates, has been gained. Based on these findings, the following conclusions were drawn on the objectives stated.

1) Investigate how the length of a charge with a constant diameter affects the velocity of the ball bearing and the damage the ball bearing causes to a steel target plate.

- It was observed that the velocity of the ball bearing increased marginally as the length of the charge increased, but once the critical mass was present and the pressure wave has time to become parallel with the directional face, the extra charge did not add significant velocity to the bearing.
- The damage the bearing did to the plate was significant. The bearing cap deflection was less than if the bearing impact was isolated from the blast but the overall deflection was still greater than the sum of the blast and bearing impact loads if conducted after each other.

2) Investigate how the depth of a ball bearing along the cylindrical axis of a charge affects the velocity of the ball bearing and the subsequent damage to a steel target plate.

- At placement 1, the ball bearing experiences its greatest impact velocity compared to other placements.
- The greatest deflection procured at either Placement 1 or 2 (depending on charge size or whether the data was captured experimentally or numerically) and decreased as the ball bearing was placed deeper into the charge.
- The greatest chance of cap deflection occurred when the ball bearing was placed at Placement 1, with the cap deflection decreasing as the ball bearing was placed deeper into the charge.
- While an understanding of the behaviour of shrapnel when located at different places within a charge was gained, shrapnel placed at closer to the edge of the charge remains a greater cause for concern for injuries and damage to humans and equipment.

3) Create a numerical simulation to replicate a blast-driven ball bearing for varying depths and charge lengths at a target plate to validate the experimental data and gain further data and to validate the model using experimental methods.

- A two-dimensional axial symmetric numerical simulation study was carried out in Ansys AUTODYN. The blast pressure waves, boundary conditions and interactions were all simulated in this work.
- The validation of the bearing velocity was calculated by the impact time of the ball bearing. This was proven to have a close agreement, with the average difference in time of arrival being -3.6%. This marginal error was shown for several charge sizes, helping to prove the close agreement in bearing velocity.
- Strong similarities were also observed in the global deflection of the target plates between the numerical work and practical experiments, with an average difference of $0.26mm$ between the experimental and numerical deflections.

- The one difference that was observed was the penetration of some experimental setups. The bearings penetrated the target plate when placed half buried for the larger charges, but penetration was not observed in the numerical work. This shows that the data used to describe the failure model for Domex 700 was not correct but this fell outside the scope of this project.

4) Conduct a parametric study, using both FEM models and experimental data, with the length of the charge and depth of the ball bearing in the charge along the cylindrical axis.

A parametric study was completed in this project and the following observations were made:

- Both the depth of the ball bearing and the length of the charge had a point of maximum deflection or damage.
- While increasing the charge increased the deflection of the target plate and velocity of the ball bearing, there was a ratio of critical mass to total charge mass where the addition of mass only increased the damage marginally.

8.2 Recommendations

Experiments should be carried out using a target plate material that has a lower yield stress:

Domex 700 is a relatively strong steel, which exhibits small permanent deflections even when subjected to loads of large magnitude. A weaker material will deflect more for the same force applied to the target. It is therefore recommended that a weaker material be used to allow for greater deflections, but the model size also be shrunk to prevent bearing penetration. The experimental data should also be expanded on to determine outliers or to close up on areas of uncertainty.

Experiments should be carried out to compare bearing depth in smaller increments and set lengths rather than percentages:

This project focused on percentage depth when burying the ball bearing in the charge. A recommendation would be to bury the bearing based on set depths based on units. These increments should also be smaller than the distances used in this project to allow for studying the bearing depth within the critical length of the charge. This will allow for a true maximum deflection based on bearing depth to be found as this project had large distances to the next buried depth. The charge sizes that did have smaller increments also had smaller charges so didn't allow for a true reflection of bearing depth to maximum deflection.

Investigate how charges can affect the material properties as a results of blast loading
Some of the observations from experiments suggested that the blast loading caused strain hardening of the steel. This greatly affected how projectiles interacted with a target. Future studies should investigate this aspect of blast interaction and how bearings interact with blast hardened steel targets.

Research on critical mass ratio should be conducted:
Even though the charge sizes all had a full critical mass present, the target plates increased in deflection as the charge size increased up to a certain mass. This was observed to be as a result of the ratio of critical mass to total mass. Experiments should be carried out to investigate the effect of the critical mass ratio

References

[1] "Improvised Explosive Devices research - AOAV", URL https://aoav.org.uk/explosiveviolence/ieds/.

[2] "IED Attack: Improvised Explosive Devices", Tech. rep., URL https://www.dhs.gov/xlibrary/assets/prep_ied_fact_sheet.pdf.

[3] R Craigie, P Farrelly, R Santos, S Smith, J Pollard & D Jones, "Manchester Arena bombing: lessons learnt from a mass casualty incident", *BMJ military health*, vol. 166, (2020), pp. 72–75.

[4] I Torjesen & A Gulland, "Manchester doctors describe aftermath of bomb blast as NHS continues to treat casualties", *BMJ (Clinical research ed.)*, vol. 357, (2017), p. j2628, URL http://dx.doi.org/doi:10.1136/bmj.j2628.

[5] C Kopp, "Technology of improvised explosive devices", *Defence Today*, vol. 4649, (2008), pp. 46–48, URL http://www.ausairpower.net/SP/DT-IED-1007.pdf.

[6] A Singh, E Goralnick, G Velmahos, P Biddinger, J Gates & A Sodickson, "Radiologic features of injuries from the Boston marathon bombing at three hospitals", *American Journal of Roentgenology*, vol. 203, (2014), pp. 235–239.

[7] P Mansoor, "improvised explosive device", 2022, URL https://www.britannica.com/technology/improvised-explosive-device.

[8] K Ghazali & M Jadin, "Detection improvised explosive device (IED) emplacement using infrared image", *Proceedings - UKSim-AMSS 16th International Conference on Computer Modelling and Simulation, UKSim 2014*, pp. 307–310.

[9] Engineering National Academies of Sciences and Medicine, *Reducing the Threat of Improvised Explosive Device Attacks by Restricting Access to Explosive Precursor Chemicals*, National Academies Press, 2018.

[10] C Wilson, "Improvised Explosive Devices (IEDs) in Iraq and Afghanistan: Effects and Countermeasures", Tech. rep., LIBRARY OF CONGRESS WASHINGTON DC CONGRESSIONAL RESEARCH SERVICE, 2005, URL `https://apps.dtic.mil/sti/citations/ADA475029`.

[11] FBI, "Eric Rudolph", URL `https://www.fbi.gov/history/famous-cases/eric-rudolph`.

[12] N Johnson, "explosive", 2022, URL `https://www.britannica.com/technology/explosive`.

[13] P Cooper, *Explosives engineering*, John Wiley & Sons, 2018.

[14] J Zukas & W Walters, *Explosive effects and applications*, Springer Science & Business Media, 2013.

[15] M Goel, V Matsagar & A Gupta, "Dynamic response of stiffened plates under air blast", *International Journal of Protective Structures*, vol. 2, (2011), pp. 139–156.

[16] M Goel, V Matsagar, A Gupta & S Marburg, "An abridged review of blast wave parameters", *Defence Science Journal*, vol. 62, (2012), pp. 300–306.

[17] G Kinney & K Graham, *Explosive Shocks in Air*, Springer, Berlin and New York, 2nd edn., 1985.

[18] S Glasstone & P Dolan, *The effects of nuclear weapons*, United States Department of Defense and the United States Department of Energy, 1977.

[19] D Chapman, "The rate of explosion in gases", *Nature*, vol. 47, (1893), pp. 299–300.

[20] E Jouguet, "On the propagation of chemical reactions in gases", *J. de mathematiques Pures et Appliquees*, vol. 1, (1905), p. 2.

[21] G Kang, "The Response of a Structural Target to an Explosive Charge Incorporating Foreign Objects: A Numerical Study", 2020.

[22] Y Zel'dovich, "On the theory of the propagation of detonation in gaseous systems", *Zh. eksp. teoret. fiz.*, vol. 10, (1940), pp. 542–568.

[23] J Von Neuman, "Theory of detonation waves", p. 40, URL `https://apps.dtic.mil/docs/citations/ADB967734`.

[24] W Döring, "Über den detonationsvorgang in gasen", *Annalen der Physik*, vol. 435, (1943), pp. 421–436.

[25] W Baker, P Cox, J Kulesz, R Strehlow & P Westine, *Explosion hazards and evaluation*, Elsevier, 2012.

[26] L Hill, J Bdzil & T Aslam, "Front curvature rate stick measurements and detonation shock dynamics calibration for PBX 9502 over a wide temperature range", Tech. rep.

[27] J Bdzil & D Stewart, "Modeling two-dimensional detonations with detonation shock dynamics", *Physics of Fluids A: Fluid Dynamics*, vol. 1, (1989), pp. 1261–1267.

[28] J Bdzil & D Stewart, "Time-dependent two-dimensional detonation: the interaction of edge rarefactions with finite-length reaction zones", *Journal of Fluid Mechanics*, vol. 171, (1986), pp. 1–26.

[29] T Aslam, J Bdzil & L Hill, "Extensions to DSD theory: Analysis of PBX 9502 rate stick data", Tech. rep.

[30] J Bdzil, T Aslam, R Catanach, L Hill & M Short, "DSD Front Models: Nonideal Explosive Detonation in ANFO", *Twelfth International Symposium on Detonation*, vol. 836, (2002.

[31] C Chiquete, M Short, S Voelkel, E Anderson & S Jackson, "Detonation shock dynamics modeling and calibration of the HMX-based conventional high explosive PBX 9501 with application to the two-dimensional circular arc geometry", *Combustion and Flame*, vol. 222, (2020), pp. 213–232.

[32] B Hopkinson, "British ordnance board minutes 13565", *The National Archives, Kew, UK*, vol. 11, (1915).

[33] C Knock, N Davies & T Reeves, "Predicting blast waves from the axial direction of a cylindrical charge", *Propellants, Explosives, Pyrotechnics*, vol. 40, (2015), pp. 169–179.

[34] C Knock & N Davies, "Blast waves from cylindrical charges", *Shock Waves*, vol. 23, (2013), pp. 337–343.

[35] J Kennedy, "Gurney energy of explosives: Estimation of the velocity and impulse imparted to driven metal", Tech. rep., Sandia Laboratories, Albuquerque.

[36] S Davids, G Langdon & G Nurick, "The influence of charge geometry on the response of partially confined right circular stainless steel cylinders subjected to blast loading", *International Journal of Impact Engineering*, vol. 108, (2017), pp. 252–262.

[37] E Lee, H Hornig & J Kury, "Adiabatic expansion of high explosive detonation products", Tech. rep.

[38] R Castedo, M Natale, L López, J Sanchidrián, A Santos, J Navarro & P Segarra, "Estimation of Jones-Wilkins-Lee parameters of emulsion explosives using cylinder tests and their numerical validation", *International Journal of Rock Mechanics and Mining Sciences*, vol. 112, (2018), pp. 290–301.

[39] H Jones & A Miller, "The detonation of solid explosives: the equilibrium conditions in the detonation wave-front and the adiabatic expansion of the products of detonation", *Proceedings of the Royal Society of London. Series A. Mathematical and Physical Sciences*, vol. 194, (1948), pp. 480–507.

[40] M Wilkins, B Squier & B Halperin, "Equation of state for detonation products of PBX 9404 and LX04-01", in: "Symposium (International) on Combustion", , vol. 10Elsevier, 1965, pp. 769–778.

[41] Sourabh Koli, P Chellapandi, Lokavarapu Bhaskara Rao & Akshay Sawant, "Study on JWL equation of state for the numerical simulation of near-field and far-field effects in underwater explosion scenario", *Engineering Science and Technology, an International Journal*, vol. 23, (2020), pp. 758–768.

[42] P Acosta, "Overview of UFC 3-340-02 structures to resist the effects of accidental explosions", in: "Structures Congress 2011", 2011, pp. 1454–1469.

[43] UFC U.S. ARMY CORPS OF ENGINEERS 3-340-02, "UFC 3-340-02. Structures to resist the effects of the accidental explosions", *Unified Facilities Criteria U.S. ARMY CORPS OF ENGINEERS*, p. 1943.

[44] C Geretto, S Chung Kim Yuen & G Nurick, "An experimental study of the effects of degrees of confinement on the response of square mild steel plates subjected to blast loading", *International Journal of Impact Engineering*, vol. 79, (2015), pp. 32–44, URL `http://dx.doi.org/10.1016/j.ijimpeng.2014.08.002`.

[45] I Edri, Z Savir, V Feldgun, Y Karinski & D Yankelevsky, "On blast pressure analysis due to a partially confined explosion: I. experimental studies", *International Journal of Protective Structures*, vol. 2, (2011), pp. 1–20.

[46] R Karpp, T Duffey & T Neal, *Response of containment vessels to explosive blast loading*, Ph.D. thesis, University of California, 1983.

[47] R Houlston, J Slater & N Pegg, "On analysis of structural response of ship panels subjected to air blast loading", *Computers & Structures*, vol. 21, (1985), pp. 273–289.

[48] T Wierzbicki & G Nurick, "Large deformation of thin plates under localised impulsive loading", *International Journal of Impact Engineering*, vol. 18, (1996), pp. 899–918.

[49] A Jacinto, R Ambrosini & R Danesi, "Experimental and computational analysis of plates under air blast loading", *International Journal of Impact Engineering*, vol. 25, (2001), pp. 927–947.

[50] R Teeling-Smith & G Nurick, "The deformation and tearing of thin circular plates subjected to impulsive loads", *International Journal of Impact Engineering*, vol. 11, (1991), pp. 77–91.

[51] N Jacob, G Nurick & G Langdon, "The effect of stand-off distance on the failure of fully clamped circular mild steel plates subjected to blast loads", *Engineering Structures*, vol. 29, (2007), pp. 2723–2736.

[52] G Nurick, M Gelman & N Marshall, "Tearing of blast loaded plates with clamped boundary conditions", *International journal of impact engineering*, vol. 18, (1996), pp. 803–827.

[53] G Nurick & J Martin, "Deformation of thin plates subjected to impulsive loading-a review Part II: Experimental studies", *International Journal of Impact Engineering*, vol. 8, (1989), pp. 171–186.

[54] S Chung Kim Yuen, G Nurick, G Langdon & Y Iyer, "Deformation of thin plates subjected to impulsive load: Part III – an update 25 years on", *International Journal of Impact Engineering*, vol. 107, (2017), pp. 1339–1351.

[55] N Mehreganian, L Louca, G Langdon, R Curry & N Abdul-karim, "International Journal of Impact Engineering The response of mild steel and armour steel plates to localised air-blast loading-comparison of numerical modelling techniques", *International Journal of Impact Engineering*, vol. 115, (2018), pp. 81–93, URL `https://doi.org/10.1016/j.ijimpeng.2018.01.010`.

[56] N Jacob, S Chung Kim Yuen, G Nurick, D Bonorchis, S Desai & D Tait, "Scaling aspects of quadrangular plates subjected to localised blast loads - Experiments and predictions", *International Journal of Impact Engineering*, vol. 30, (2004), pp. 1179–1208.

[57] G Langdon, S Chung Kim Yuen & G Nurick, "Experimental and numerical studies on the response of quadrangular stiffened plates. Part II: localised blast loading", *International Journal of Impact Engineering*, vol. 31, (2005), pp. 85–111.

[58] G Nurick, S Mahoi & G Langdon, "The response of plates subjected to loading arising from the detonation of different shapes of plastic explosive", *International Journal of Impact Engineering*, vol. 89, (2016), pp. 102–113, URL `http://dx.doi.org/10.1016/j.ijimpeng.2015.11.012`.

[59] D Fiserova, *Numerical Analyses of Buried Mine Explosions With Emphasis on Effect of Soil Properties on Loading*, Phd, Cranfield University, 2006, URL `http://hdl.handle.net/1826/1209`.

[60] Century Dynamics, "ANSYS AUTODYN: User Manual", pp. 1–501.

[61] R Qi, G Langdon, T Cloete & S Chung Kim Yuen, "Behaviour of a blast-driven ball bearing embedded in rear detonated cylindrical explosive", *International Journal of Impact Engineering*, vol. 146, (2020), p. 103698.

[62] W Flis, "A Lagrangian approach to modeling the acceleration of metal by explosives", in: "17th Southeastern Conf. Theor. Appl. Mech", .

[63] G Fairlie, "The numerical simulation of high explosives using AUTODYN-2D & 3D", in: "Institute of explosive engineers 4th biannual symposium", pp. 743–751.

[64] T Slavik, "A coupling of empirical explosive blast loads to ALE air domains in LS-DYNA®", in: "IOP Conference Series: Materials Science and Engineering", , vol. 10IOP Publishing, p. 12146.

[65] Z Tabatabaei & J Volz, "A comparison between three different blast methods in LS-DYNA: LBE, MM-ALE, Coupling of LBE and MM-ALE", in: "12th International LS-DYNA Users Conference", 2012, pp. 1–10.

[66] M Grujicic, B Pandurangan & B Cheeseman, "The effect of degree of saturation of sand on detonation phenomena associated with shallow-buried and ground-laid mines", *Shock and Vibration*, vol. 13, (2006), pp. 41–61.

[67] B Robins, *New Principles of Gunnery: Containing the Determination of the Force of Gunpowder, and Investigation of the Difference in the Resisting Power of the Air*, F. Wingrave, in the Strand.

[68] L Euler, "Neue grundsätze der artillerie", .

[69] W Goldsmith, "Non-ideal projectile impact on targets", *International Journal of Impact Engineering*, vol. 22, (1999), pp. 95–395.

[70] M Backman & W Goldsmith, "The mechanics of penetration of projectiles into targets", *International Journal of Engineering Science*, vol. 16, (1978), pp. 1–99.

[71] M Nishida, Y Hiraiwa, K Hayashi & S Hasegawa, "Scaling laws for size distribution of fragments resulting from hypervelocity impacts of aluminum alloy spherical projectiles on thick aluminum alloy targets: Effects of impact velocity and projectile diameter", *International Journal of Impact Engineering*, vol. 109, (2017), pp. 400–407.

[72] U Nyström & K Gylltoft, "Numerical studies of the combined effects of blast and fragment loading", *International Journal of Impact Engineering*, vol. 36, (2009), pp. 995–1005, URL http://dx.doi.org/10.1016/j.ijimpeng.2009.02.008.

[73] K Marchand, M Vargas & J Nixon, "The synergistic effects of combined blast and fragment loadings", Tech. rep.

[74] R Gurney, "The Initial Velocities of Fragments from Bombs, Shell, and Grenades", *Ballistic Research Laboratories*, vol. 405, (1943), pp. 1–22, URL http://oai.dtic.mil/oai/oai?verb=getRecord&metadataPrefix=html&identifier=ADA8001

[75] Manfred Held, "Single fragment generator", *Propellants, Explosives, Pyrotechnics*, vol. 25, (2000), pp. 8–12.

[76] P Choudha, A Kumaraswamy & K Dhote, "Parametric study of single confined fragment launch explosive device", *Defence Technology*, vol. 15, (2019), pp. 179–185, URL https://doi.org/10.1016/j.dt.2018.08.015.

[77] H Grisaro & A Dancygier, "Numerical study of velocity distribution of fragments caused by explosion of a cylindrical cased charge", *International Journal of Impact Engineering*, vol. 86, (2015), pp. 1–12, URL http://dx.doi.org/10.1016/j.ijimpeng.2015.06.024.

[78] H Grisaro & A Dancygier, "Characteristics of combined blast and fragments loading", *International Journal of Impact Engineering*, vol. 116, (2018), pp. 51–64, URL https://doi.org/10.1016/j.ijimpeng.2018.02.004.

[79] U S Army, "CONWEP, Conventional Weapons Effects", *Fundamentals of protective design for conventional weapons TM5-855-11992, US Army. Engineer Waterways Experiment Station, Vicksburg.*

[80] J Leppänen, *Concrete structures subjected to fragment impacts*, Chalmers Tekniska Hogskola (Sweden).

[81] E Pickering, S Chung Kim Yuen, G Nurick & P Haw, "The response of quadrangular plates to buried charges", *International journal of impact engineering*, vol. 49, (2012), pp. 103–114.

[82] S Chung Kim Yuen, G Langdon, G Nurick, E Pickering & V Balden, "Response of V-shape plates to localised blast load: Experiments and numerical simulation", *International Journal of Impact Engineering*, vol. 46, (2012), pp. 97–109, URL `http://dx.doi.org/10.1016/j.ijimpeng.2012.02.007`.

[83] P Sherkar, J Shin, A Whittaker & A Aref, "Influence of charge shape and point of detonation on blast-resistant design", *Journal of structural engineering*, vol. 142, (2016), p. 4015109.

[84] J Jestin, F Ali, A Zaidi, M Koslan & M Othman, "Mesh Sensitivity Study of Soil Barrier Subjected to Blast Loading: Numerical Methods Using AUTODYN 3D", *Modern Applied Science*, vol. 8, (2014), p. 250.

[85] Ansys Inc, "Ansys Autodyn material library", .

[86] G Langdon, S Kriek & G Nurick, "Influence of venting on the response of scaled aircraft luggage containers subjected to internal blast loading", *International Journal of Impact Engineering*, vol. 141, (2020), p. 103567, URL `https://doi.org/10.1016/j.ijimpeng.2020.103567`.

[87] D Bogosian, M Yokota & S Rigby, "TNT Equivalence of C-4 and PE4 : a Review of Traditional Sources and Recent Data", .

[88] G Johnson, "A constitutive model and data for materials subjected to large strains, high strain rates, and high temperatures", *Proc. 7th Inf. Sympo. Ballistics*, pp. 541–547.

[89] N Jacob, *The effect of stand-off distance on the failure of thin plates subjected to blast loads*, Ph.D. thesis, University of Cape Town, 2005, URL

https://uct.primo.exlibrisgroup.com/permalink/27UCT_INST/1jjtfba/alma99
0007852890904041.

Appendices

Appendix A

Impulse Experimental Procedure and Calculations

The impulse captured from blast experiments has provided insight into the effects of charge shape and size [56, 58, 57, 61]. In this Appendix, how the displacement history was captured is presented. This is followed by the displacement history graphs from the light sensor and the calculations used to determine the impulse.

A.1 Capturing the Horizontal Displacement Profile of the Ballistic Pendulum

During a blast test, the horizontal displacement time history of the ballistic pendulum was tracked with the use of a laser sensor that projected onto a plate at the back of the pendulum, as displayed in Figure A.1. The location of the laser sensor is shown in Figure A.2.

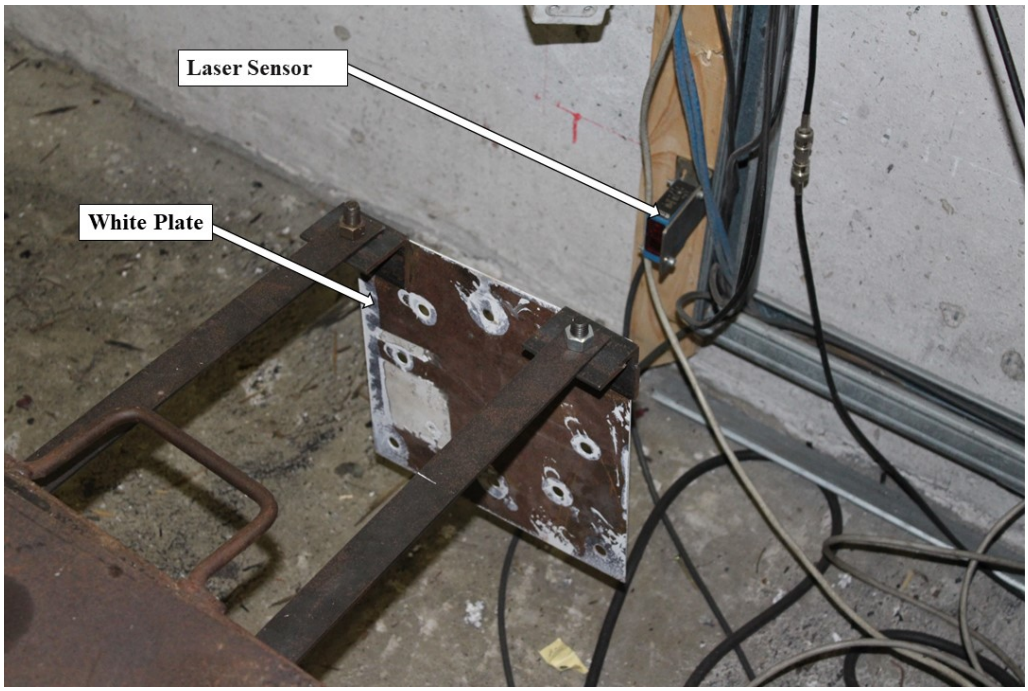

Figure A.1 Photograph showing the laser pointing towards the white plate at the rear of the pendulum.

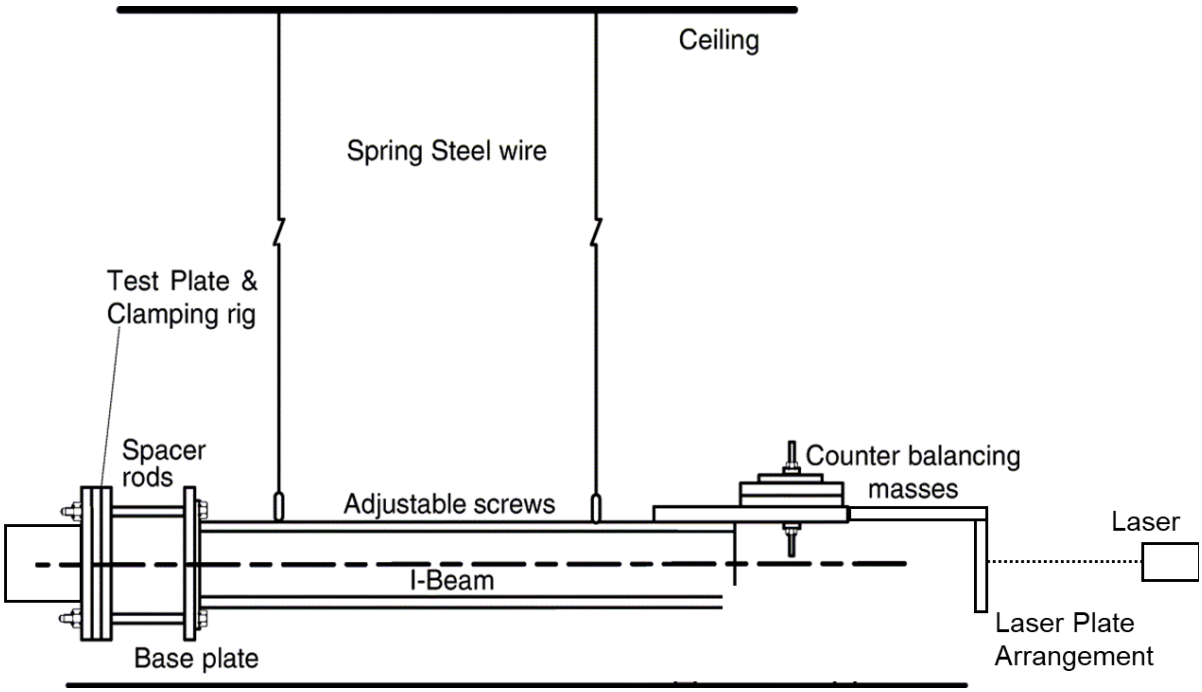

Figure A.2 Schematic of the ballistic pendulum used in the blast experiments [56].

A.2 Displacement vs Time history graphs recorded from the light sensor

Figures A.3 through to A.8 shows the displacement vs time history graph for the data captured from the laser sensor for the various charge sizes and ball bearing placements.

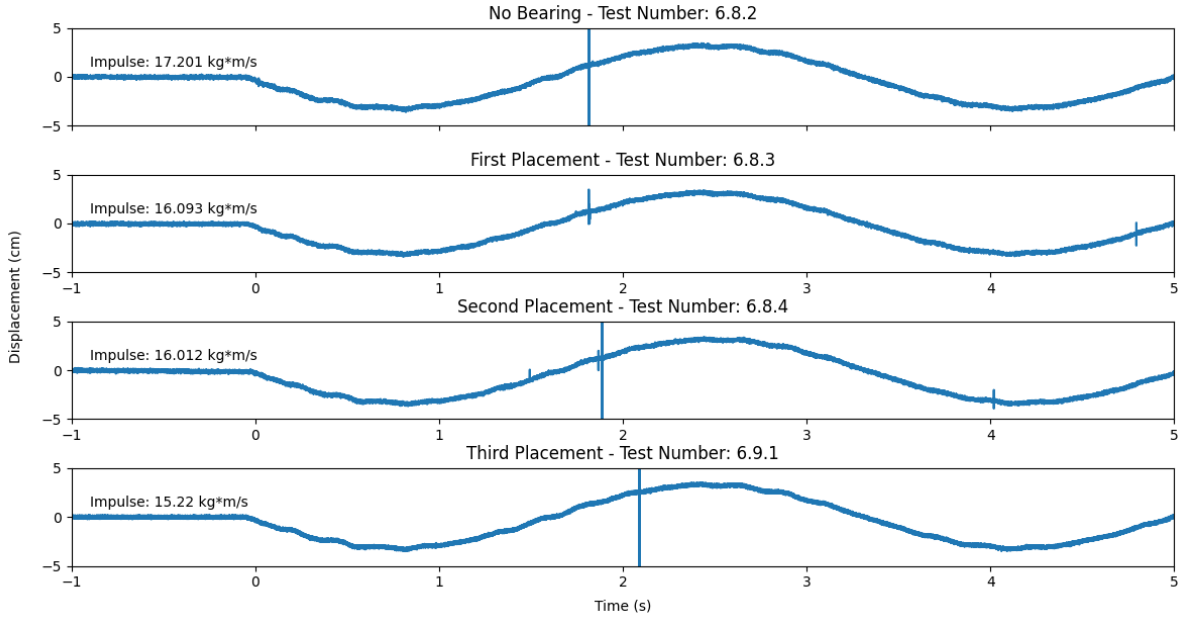

Figure A.3 Graphs showing the side by side comparison of the 10g.

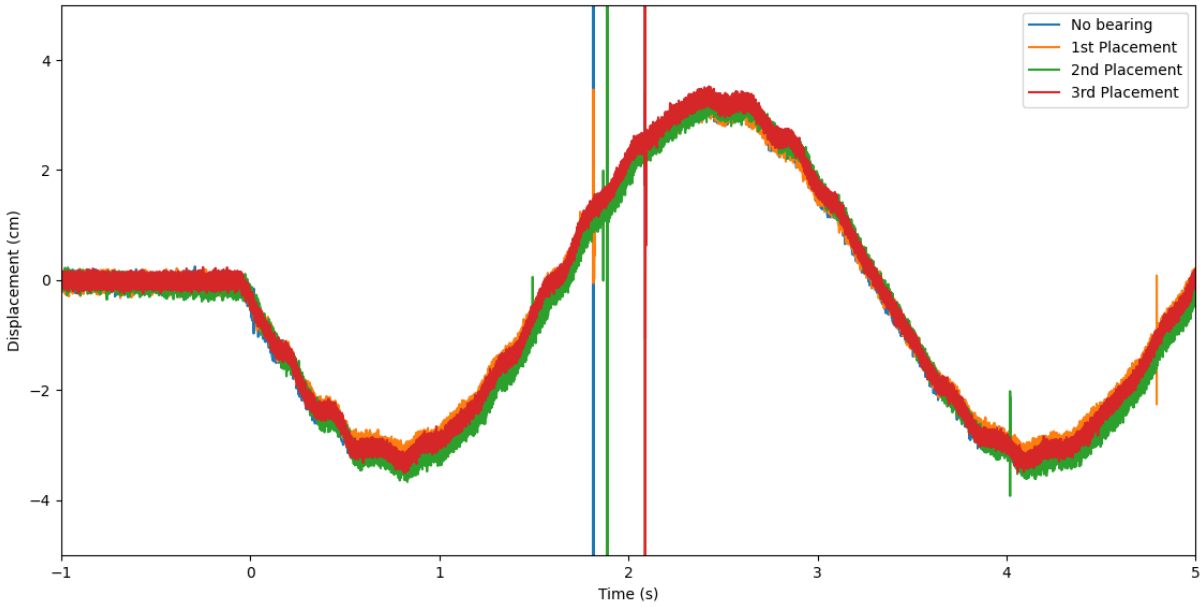

Figure A.4 Graphs showing the 10g tests layered onto each other.

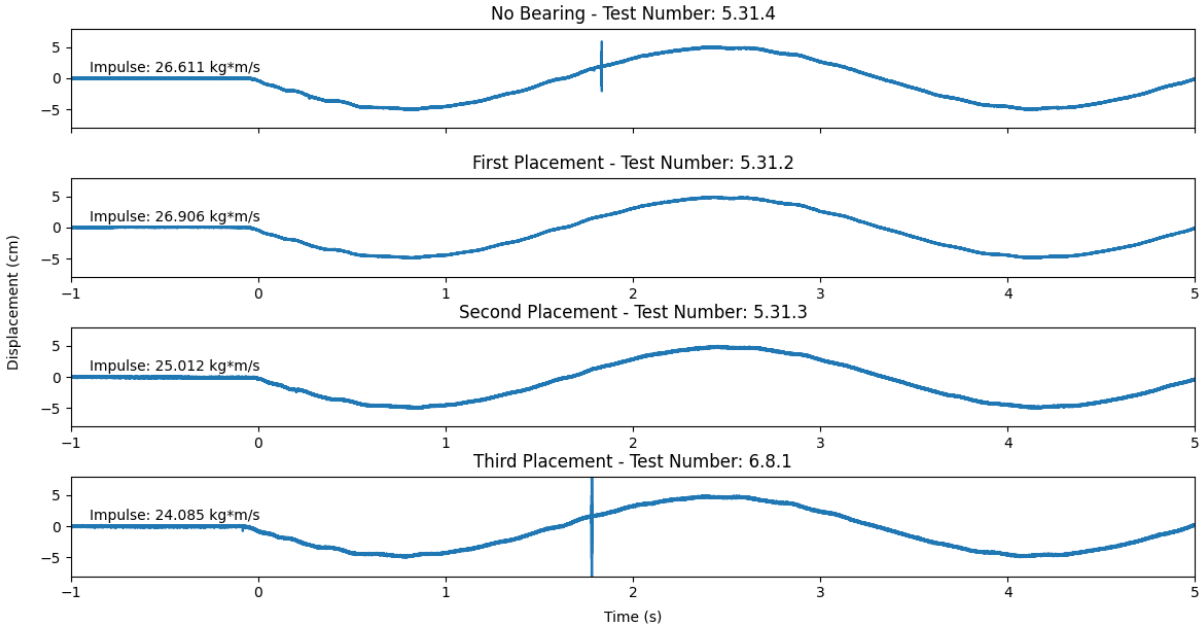

Figure A.5 Graphs showing the side by side comparison of the $20g$.

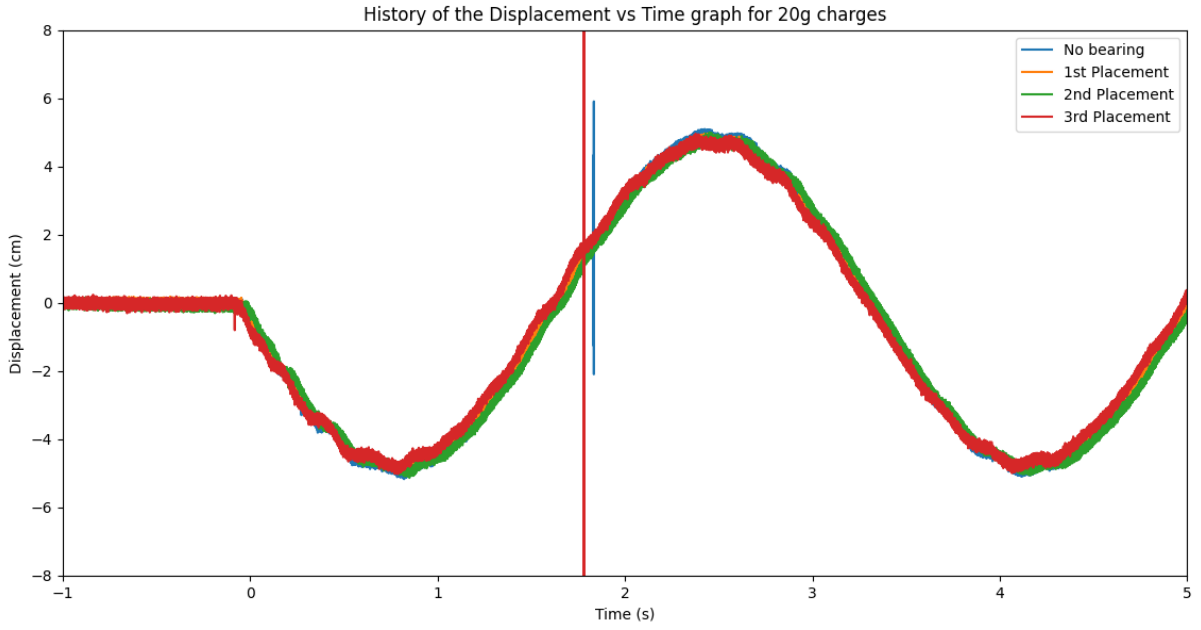

Figure A.6 Graphs showing the $20g$ tests layered onto each other.

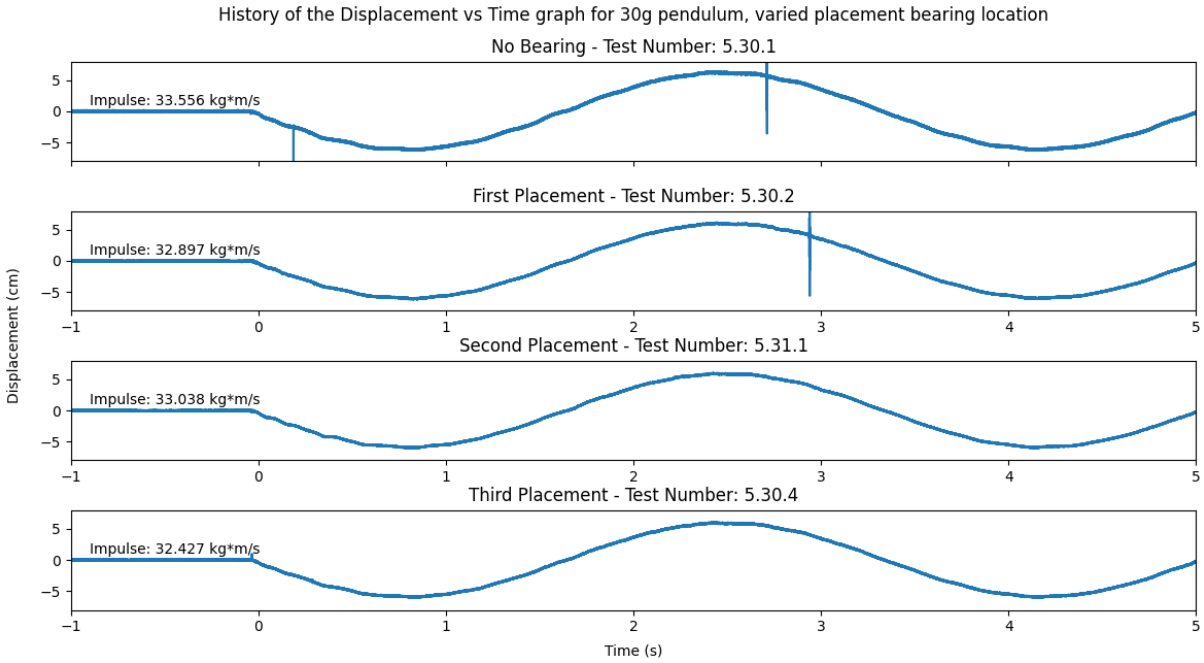

Figure A.7 Graphs showing the side by side comparison of the 30g.

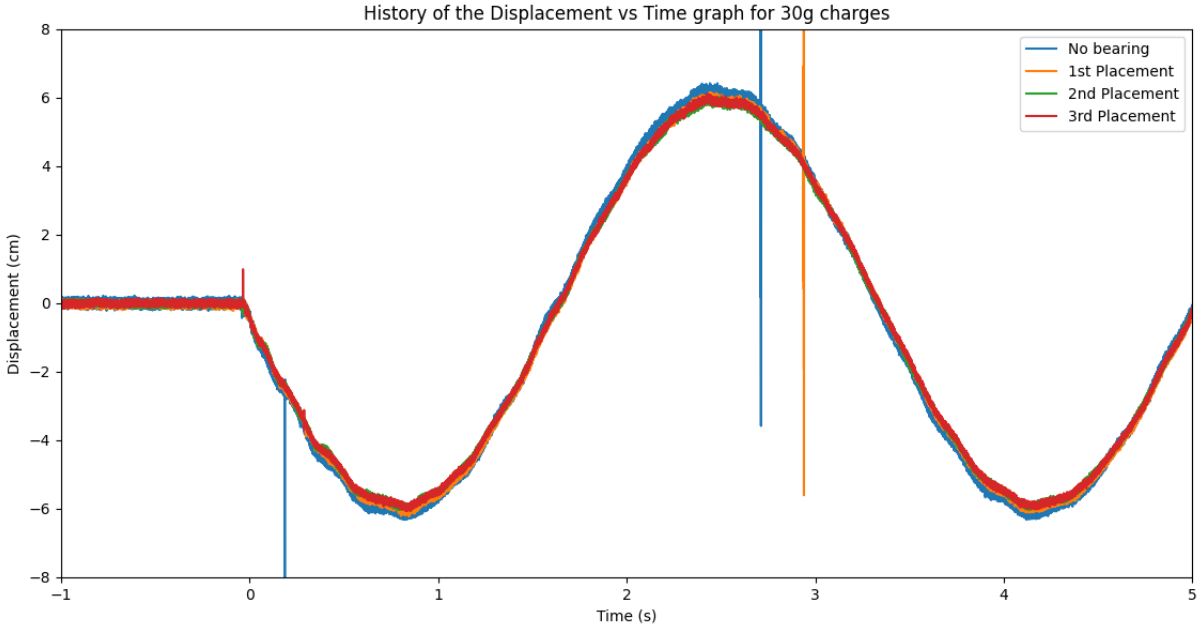

Figure A.8 Graphs showing the 30g tests layered onto each other.

A.3 Derivation of Impulse from Graphs

With the displacement history captured, it was possible to calculate the impulse delivered from the charge. The impulse was determined using a similar method to Jacob [89], and a brief derivation is presented. The initial impulse of the blast is directly proportional to the mass and initial velocity of the pendulum. The pendulum can be modeled as a single dimension free vibration problem. This means the equation of motion can be written as Equation A.1.

$$m\ddot{x} + c\dot{x} + kx = 0 \tag{A.1}$$

Where m is the mass, k is the spring coefficient and c is the damping coefficient. The general coefficient can then be written as

$$x(t) = x_0 + \frac{e^{-\beta t}\dot{x}_0 sin(w_d t + \theta)}{w_d} \tag{A.2}$$

where x_0 is the initial displacement, $\dot{x}_0$ is the initial velocity of the pendulum, w_d is the damped frequency, θ is the phase of motion and β is an expression shown by the damping coefficient over twice the mass. Derived from the above equations, and shown by [89], impulse can be shown as:

$$I = m\ddot{(}x) \tag{A.3}$$

In Table A.1, the results presented in Figures A.3 to A.8, as well as the recorded impulses are listed in tabular form.

Table A.1 *Table listing the impulse and maximum displacement of the pendulum for the experiments.*

Test No.	**Charge Mass** (g)	**Placement**	**Impulse** (Ns)	**Maximum Horizontal Displacement (m)**
6.08.2	10	N/A	17.2	0.036
6.08.3	10	1	16.09	0.034
6.08.4	10	2	16.01	0.037
6.09.1	10	3	15.22	0.035
5.31.4	20	N/A	26.61	0.052
5.31.2	20	1	26.91	0.05
5.31.3	20	2	25.01	0.051
6.08.1	20	3	24.09	0.050
5.30.1	30	N/A	33.56	0.063
5.30.2	30	1	32.9	0.062
5.31.1	30	2	33.04	0.060
5.30.4	30	3	32.43	0.061
6.9.2	10	Pre-cut	15.11	0.031
6.9.3	20	Pre-cut	25.36	0.049
6.9.4	30	Pre-cut	33.87	0.063

Appendix B

Tensile Test Results

The true stress vs true strain graphs collected from the tensile tests for the Domex 700 steel, followed by the results gathered from the tests used in the Johnson-Cook equation to describe the Domex 700 in the numerical simulations are presented in this Appendix.

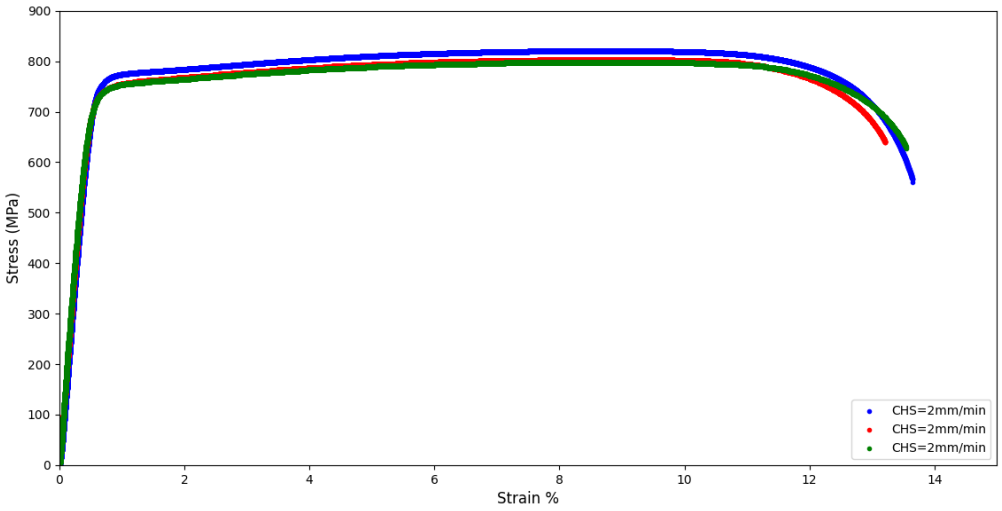

Figure B.1 Graphs showing the stress vs strain relation from the tensile tests with a cross head speed of $2mm/min$.

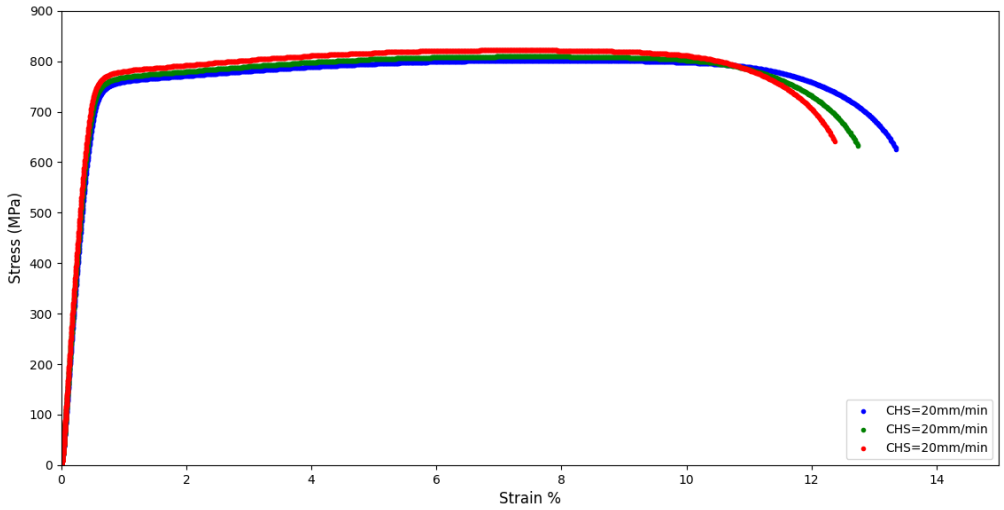

Figure B.2 Graphs showing the stress vs strain graphs relation the tensile tests with a cross head speed of $20mm/min$.

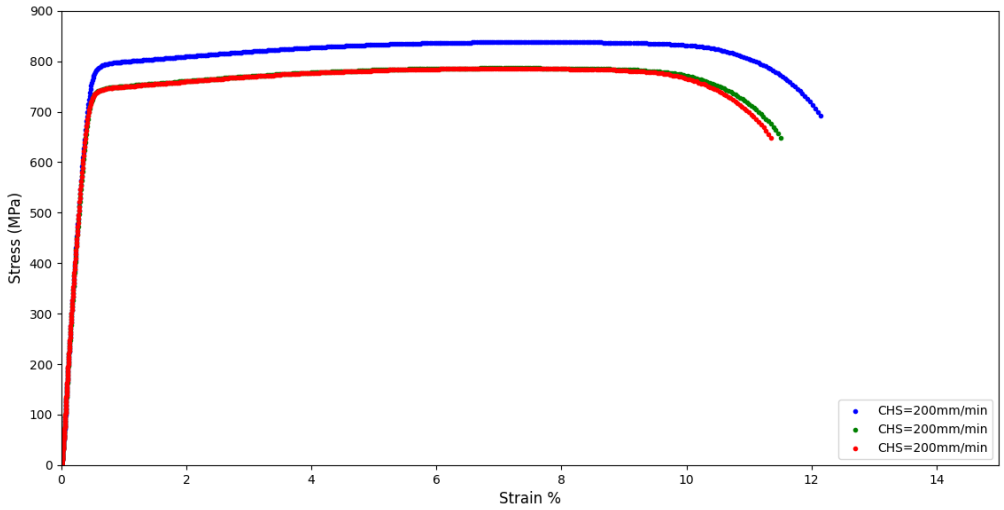

Figure B.3 Graphs showing the stress vs strain graphs relation the tensile tests with a cross head speed of $200mm/min$.

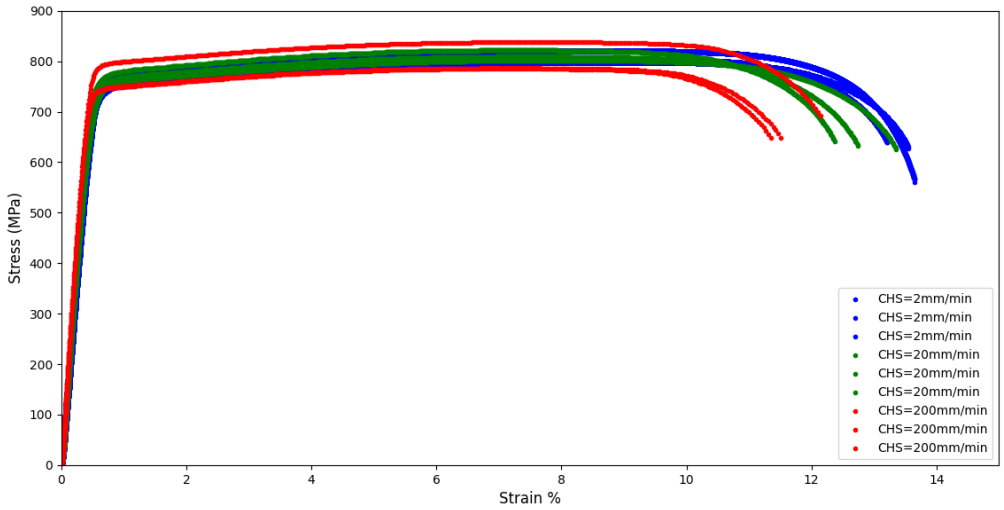

Figure B.4 Graphs showing all the tensile test graphs on the same set of axes.

Table B.1 *Table listing all the Johnson-Cook values gathered from the Tensile Tests.*

Exp Number	Johnson Cook Value			Strain at Failure (%)	Ultimate Tensile Strength (MPa)
	A (MPa)	B (MPa)	n		
3	753	227	0.559	0.136	821
4	739	242	0.457	0.132	803
5	731	275	0.510	0.135	798
6	741	293	0.551	0.134	802
7	752	132	0.361	0.127	810
8	763	350	0.606	0.124	822
9	779	209	0.447	0.121	838
10	731	270	0.528	0.115	787
11	731	214	0.471	0.113	785
	747	246	0.487	0.127	807

Appendix C

Engineering Drawings

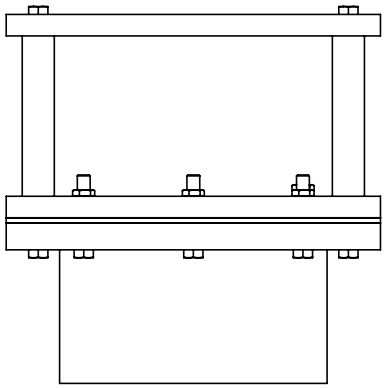

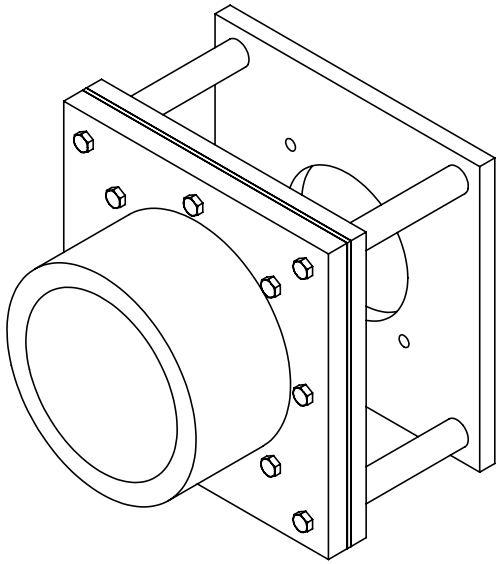

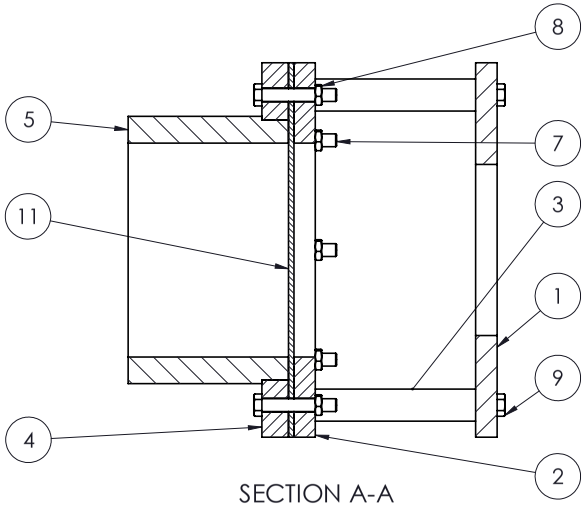

SECTION A-A

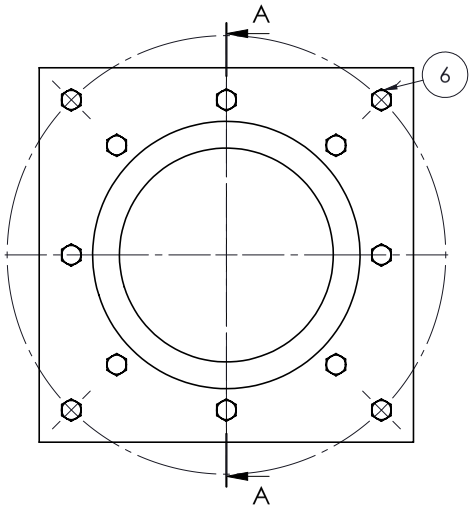

NO.	PART NUMBER	DESCRIPTION	SPECIFICATION	QTY
11	T_1	Target Plate	See DWG for details, Domex 700	1
10	UCT-11109	Hex nut M12	ISO 4032 - M12, Carbon Steel Gr 8.8	2
9	UCT-01107	Hex Bolt M12	ISO 4015 - M12 X 55 x 30, Carbon Steel Gr 8.8	4
8	UCT-11209	Hex thin nut M12	ISO 4035 - M12, Carbon Steel Gr 8.8	7
7	UCT-01113	Hex Bolt M12	ISO 4015 - M12 X 70 x 30, Carbon Steel Gr 8.8	8
6	UCT-01119	Hex Bolt M12	ISO 4015 - M12 X 100 x 30, Carbon Steel Gr 8.8	4
5	BR_1	Blast Tube	See DWG for details, Plain Carbon Steel	1
4	BR_2	Front Clamp	See DWG for details, Plain Carbon Steel	1
3	BR_5	Spacing Sleeve	See DWG for details, Plain Carbon Steel	4
2	BR_3	Back Clamp	See DWG for details, Plain Carbon Steel	1
1	BR_4	Extender Plate	See DWG for details, Plain Carbon Steel	1

Scale: 1:5 on A3	University of Cape Town Department of Mechanical Engineering			
Drawn By: Matthew Hoare	All un-toleranced dimensions to adhere to ISO 2768-m	Title: Blast Rig Assembly		
Checked :	Assembly drawing	Drawing Number : BR_A	Rev. : A	Sheet : 1 of 1

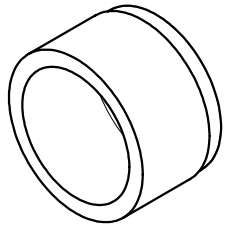

Scale1:10

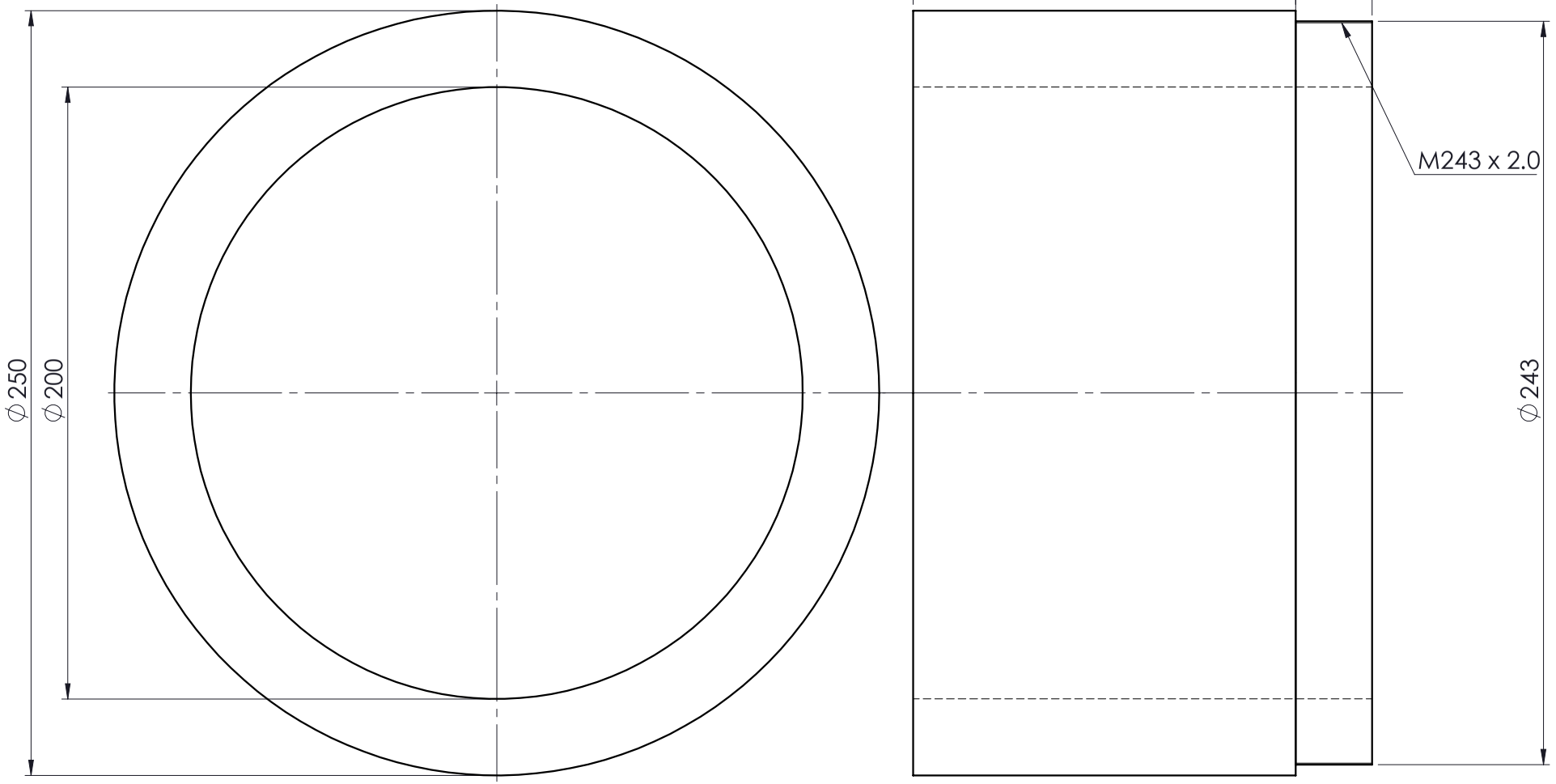

Scale: 1:2 on A4	University of Cape Town Department of Mechanical Engineering			
Drawn By: Matthew Hoare	All un-toleranced dimensions to adhere to ISO 2768-m	Title: Blast Tube		
Checked :	Material : Plain Carbon Steel	Drawing Number : BR_1	Rev. : A	Sheet : 1 of 1

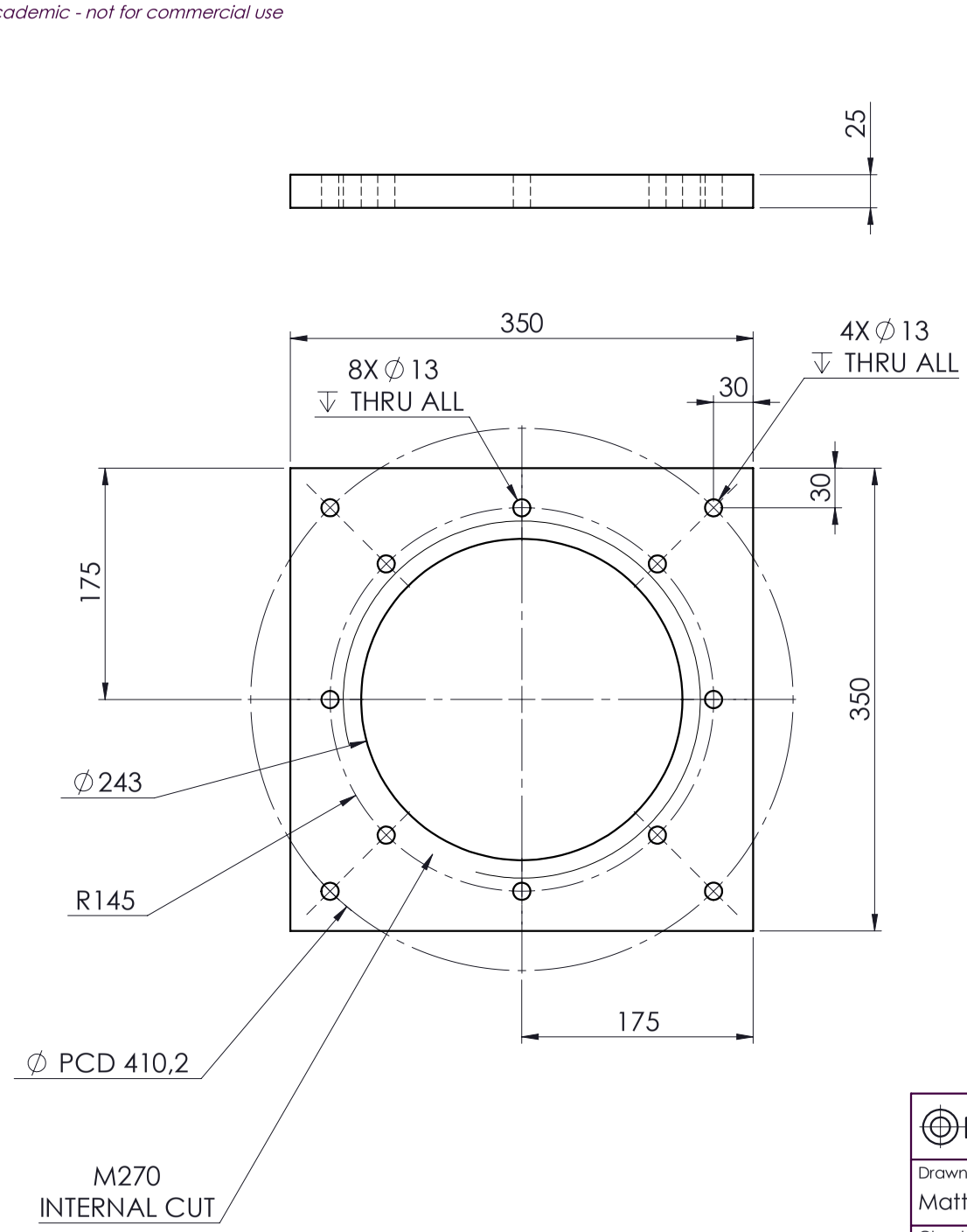

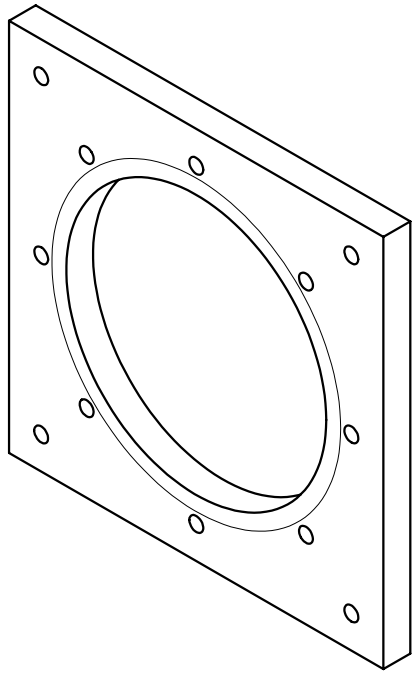

Scale: 1:5 on A4	University of Cape Town Department of Mechanical Engineering			
Drawn By: Matthew Hoare	All un-toleranced dimensions to adhere to ISO 2768-m	Title: Front Clamp		
Checked :	Material : Plain Carbon Steel	Drawing Number : BR_2	Rev. : A	Sheet : 1 of 1

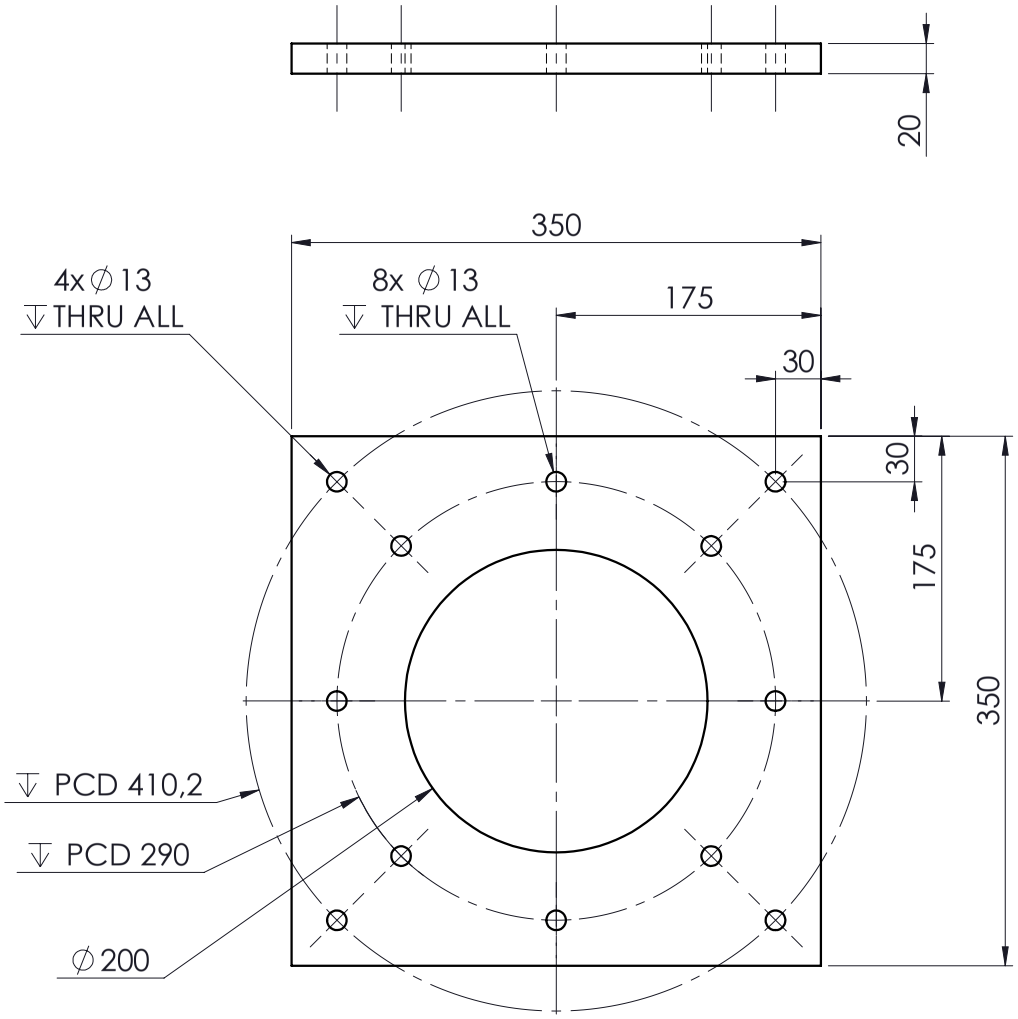

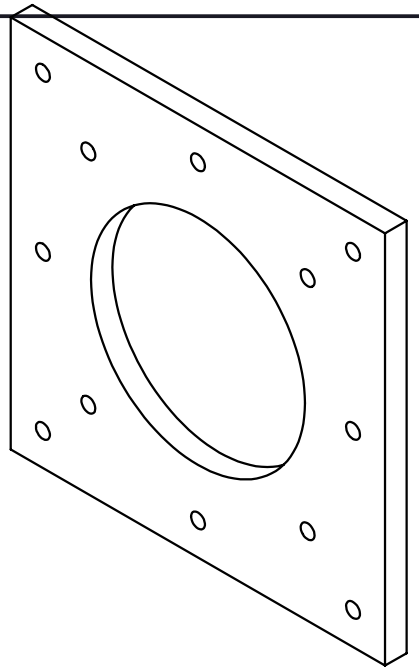

Scale: 1:5 on A4	University of Cape Town Department of Mechanical Engineering			
Drawn By: Matthew Hoare	All un-toleranced dimensions to adhere to ISO 2768-m	Title: Back Clamp		
Checked :	Material : Plain Carbon Steel	Drawing Number : BR_3	Rev. : A	Sheet : 1 of 1

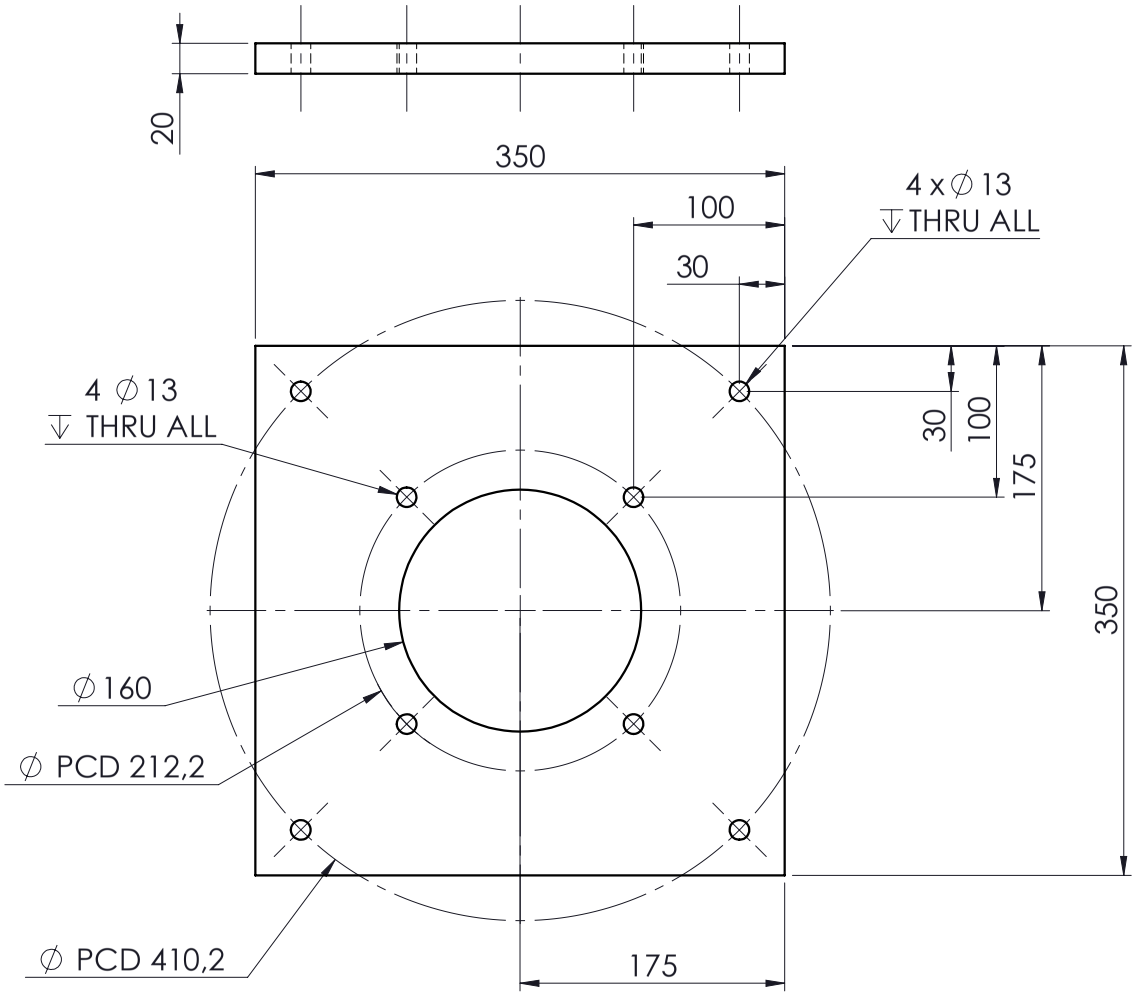

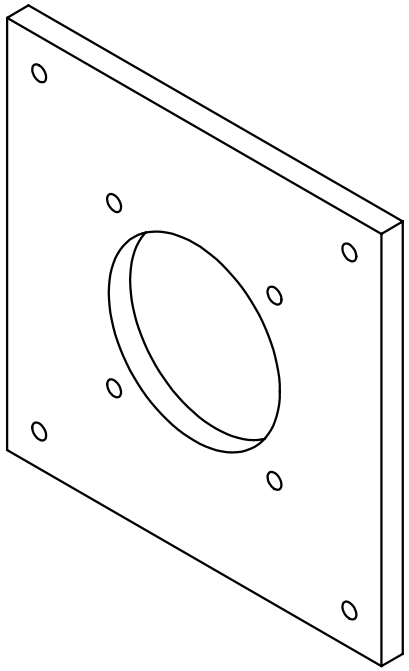

Scale: 1:5 on A4	University of Cape Town Department of Mechanical Engineering			
Drawn By: Matthew Hoare	All un-toleranced dimensions to adhere to ISO 2768-m	Title: Extender Plate		
Checked :	Material : Plain Carbon Steel	Drawing Number : BR_4	Rev. : A	Sheet : 1 of 1

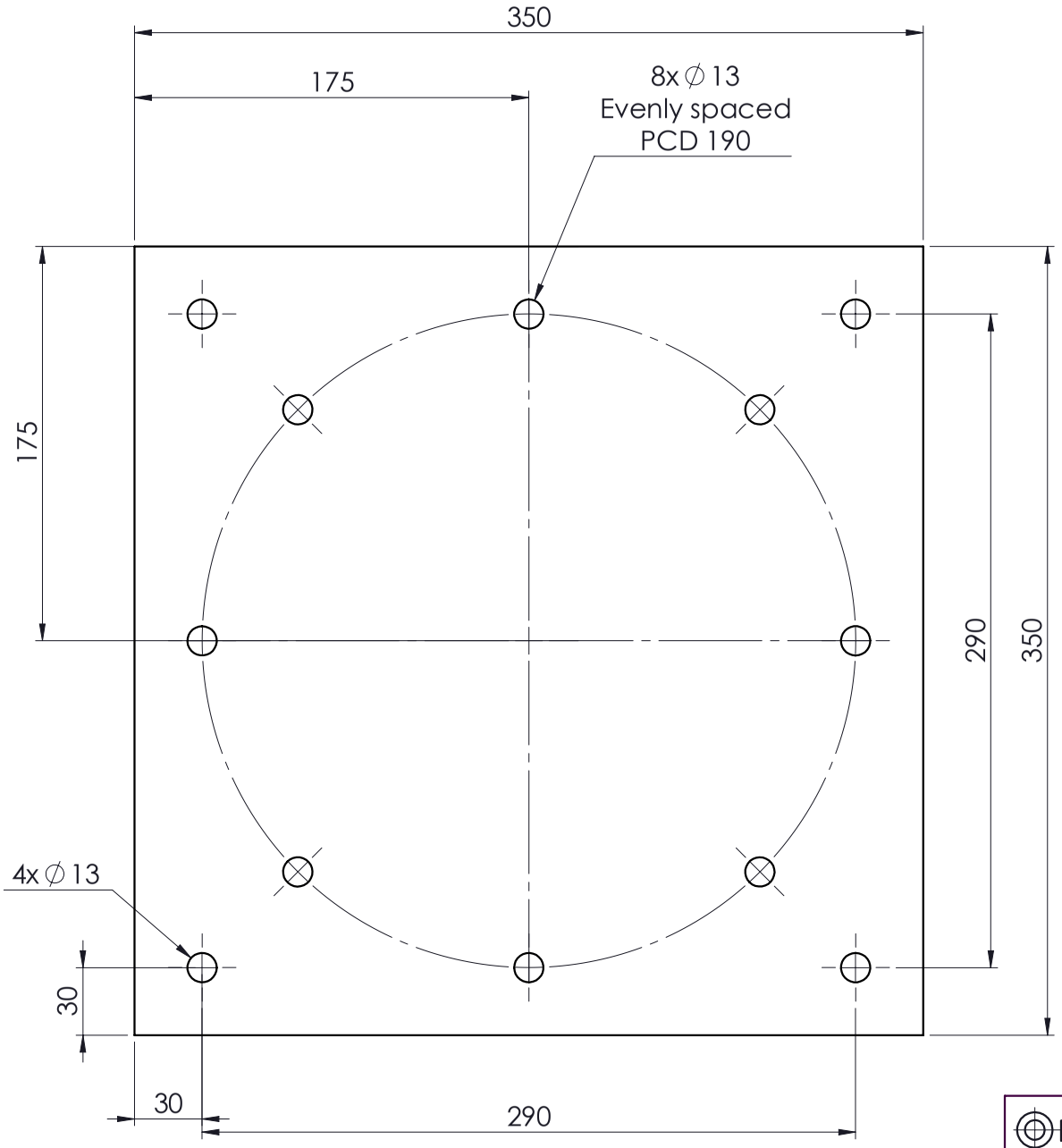

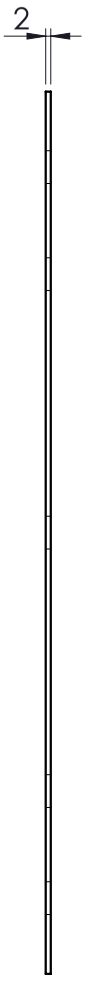

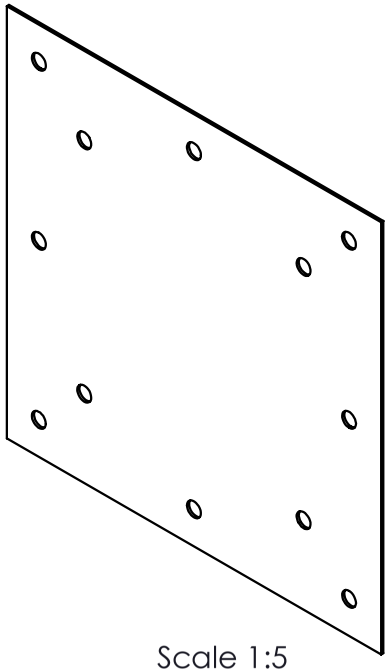

Scale 1:5

Quantity:
50

Note:
Holes through all

Scale: 1:3 on A4	University of Cape Town Department of Mechanical Engineering			
Drawn By: Matthew Hoare	All un-toleranced dimensions to adhere to ISO 2768-m	Title: Target Plate		
Checked :	Material : Domex 700	Drawing Number : 8	Rev. : A	Sheet : 1 of 1

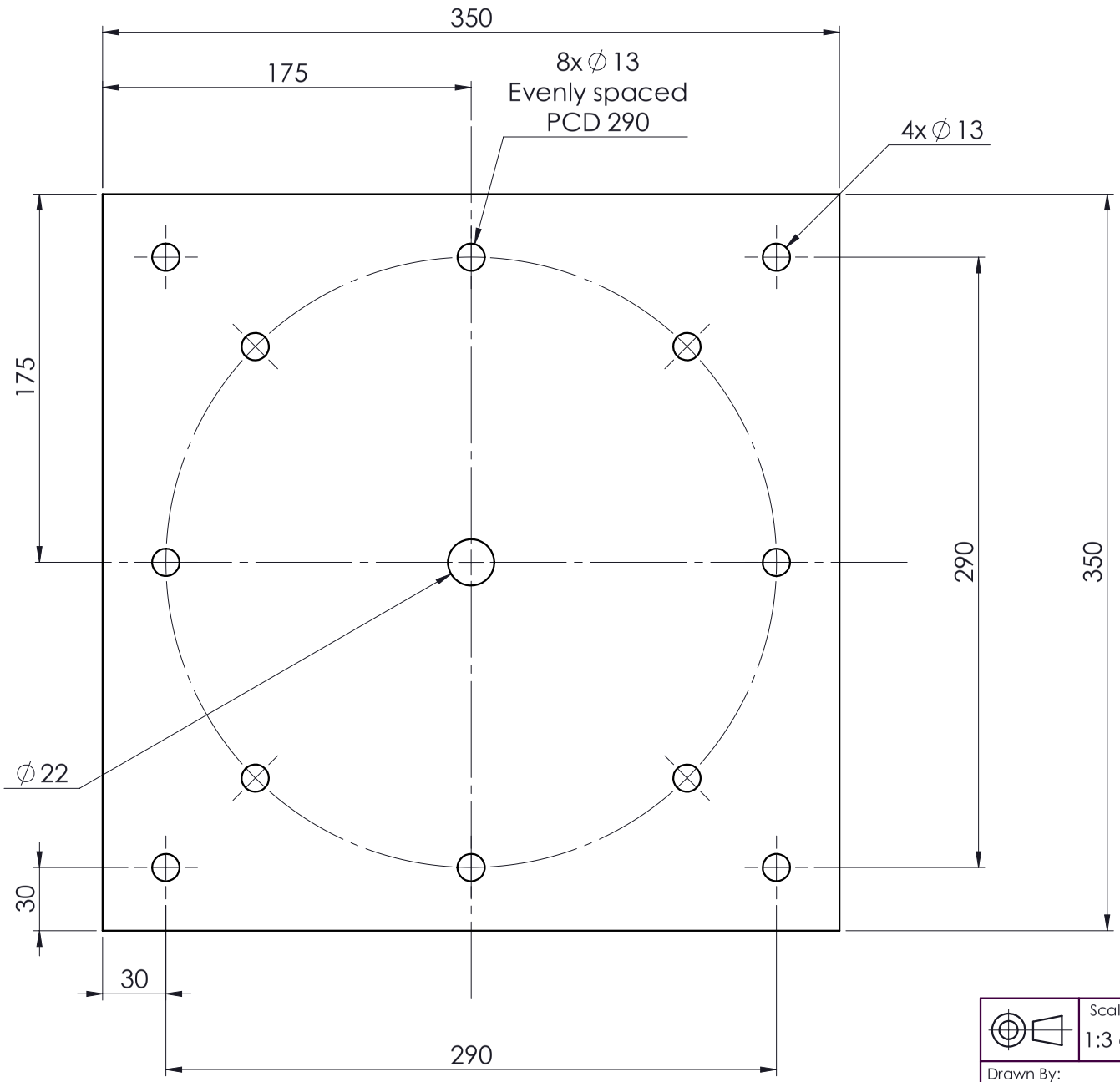

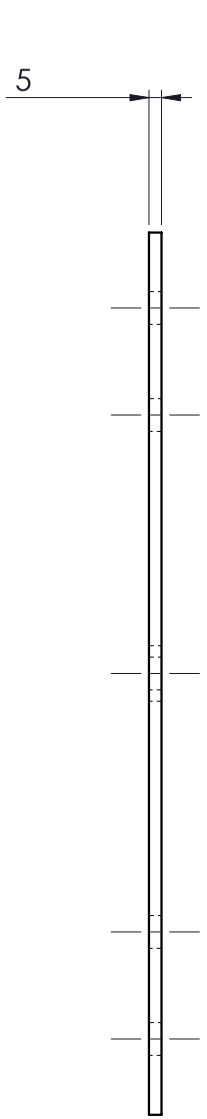

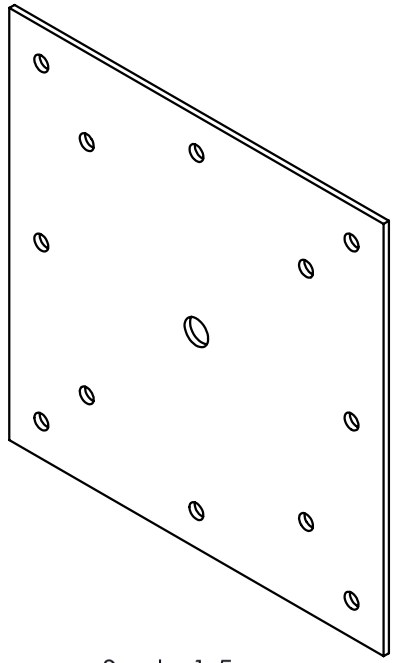

Scale 1:5

Quantity:
10 plates

Note:
Holes through all

Scale: 1:3 on A4	University of Cape Town Department of Mechanical Engineering			
Drawn By: Matthew Hoare	All un-toleranced dimensions to adhere to ISO 2768-m	Title: Velocity Target Plate		
Checked :	Material : Domex 700	Drawing Number : 7	Rev. : A	Sheet : 1 of 1

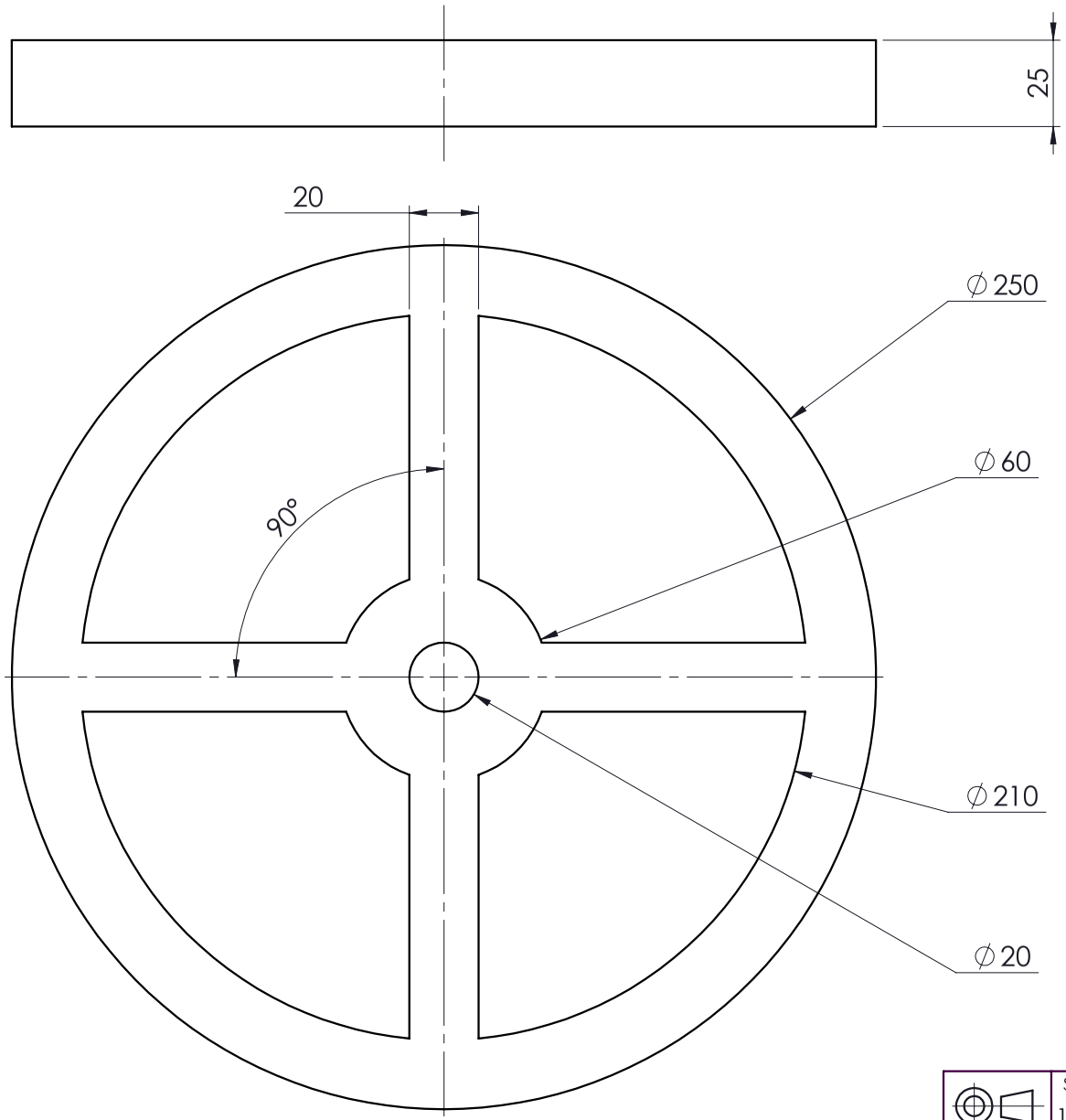

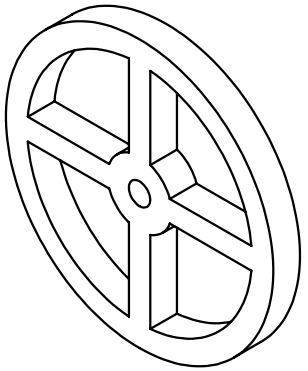

Scale 1:5

Scale: 1:5 on A4	University of Cape Town Department of Mechanical Engineering			
Drawn By: Matthew Hoare	All un-toleranced dimensions to adhere to ISO 2768-m	Title: Polystyrene Wheel		
Checked :	Material : Polystyrene	Drawing Number :	Rev. : A	Sheet : 1 of 1

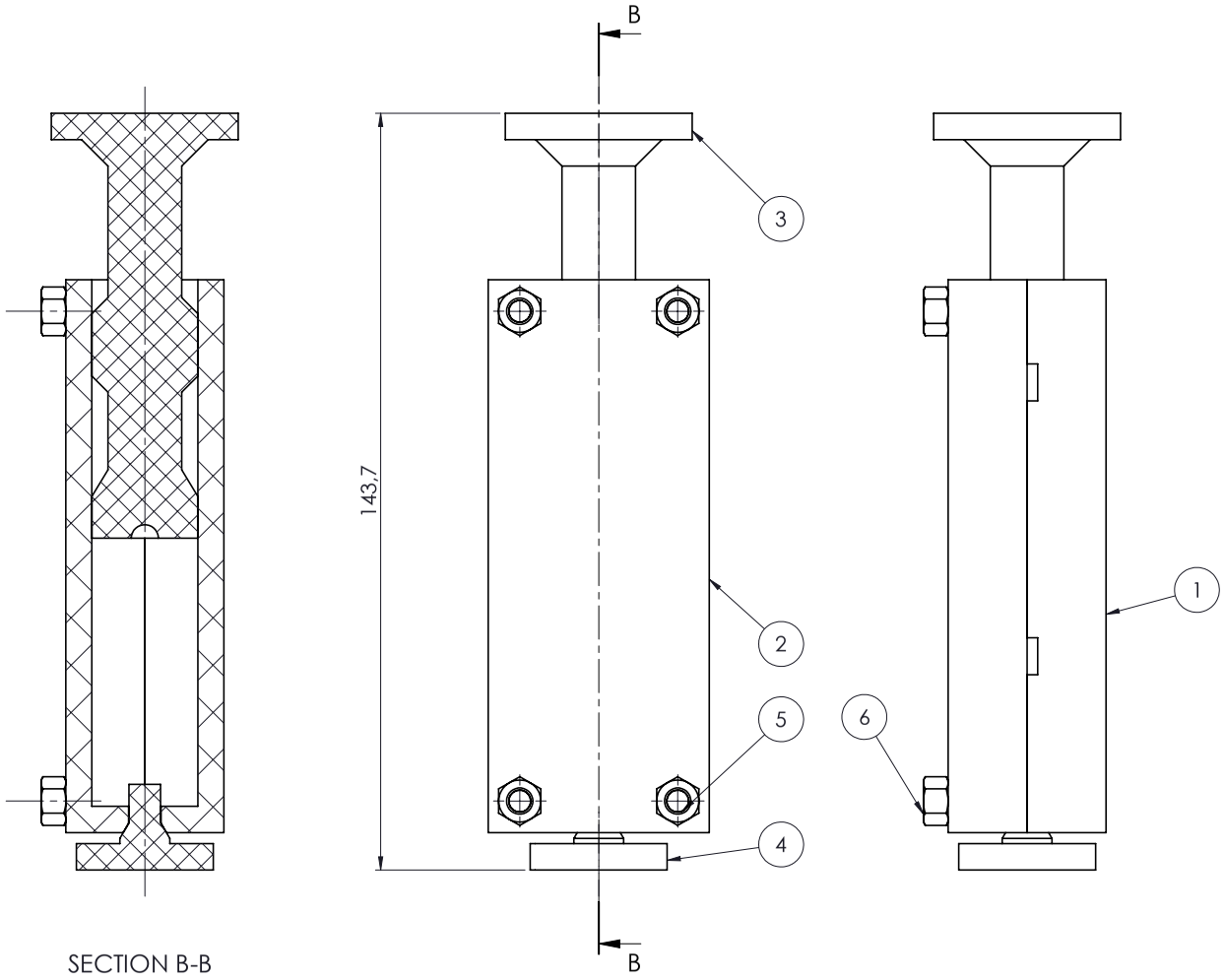

SECTION B-B

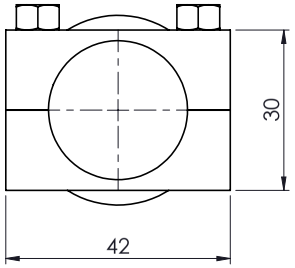

NO.	PART NUMBER	DESCRIPTION	SPECIFICATION	QTY
6	UCT-11105	Hex nut M5	ISO 4032 - M5, Carbon Steel Gr 8.8	4
5	UCT-01036	Hex Bolt M5	ISO 4015 - M5 X 30 x 30, Carbon Steel Gr 8.8	4
4	M_3	Detonator Press	See DWG for details, Polyester Resin	1
3			See DWG for details, Material <not specified>	1
2	M_1	Base_Female	See DWG for details, Polyester Resin	1
1	M_2	Base_Male	See DWG for details, Polyester Resin	1

Scale: 1:1 on A3

University of Cape Town
Department of Mechanical Engineering

Drawn By: Matthew Hoare

All un-toleranced dimensions to adhere to ISO 2768-m

Title: Charge Mould Assembly Drawing

Checked :

Assembly drawing

Drawing Number : M_A

Rev. : A

Sheet : 1 of 1

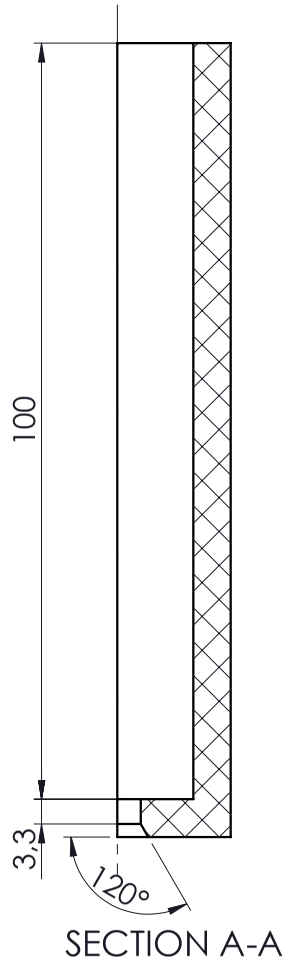

SECTION A-A

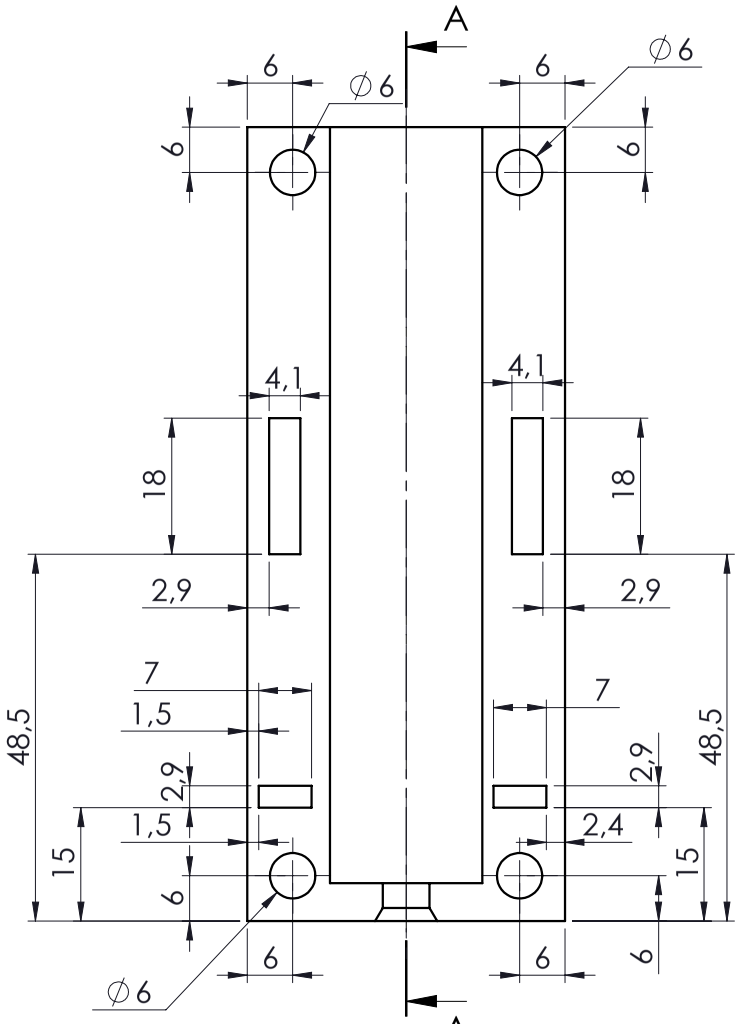

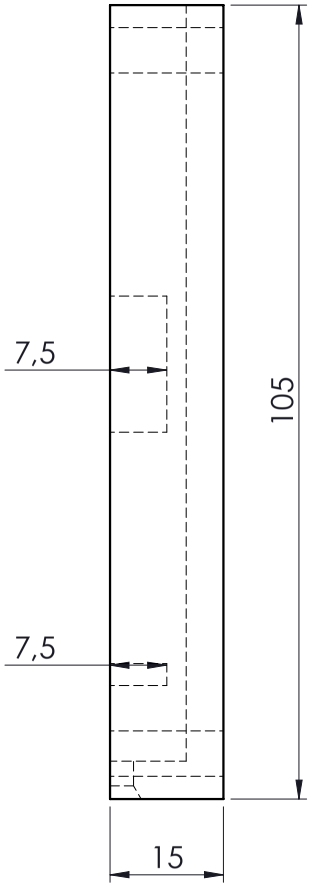

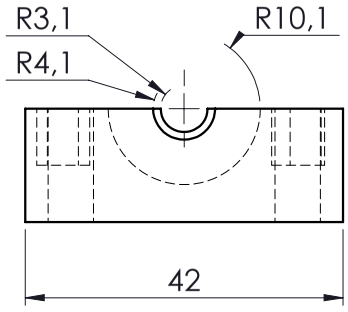

Scale: 1:1 on A4	University of Cape Town Department of Mechanical Engineering			
Drawn By: Matthew Hoare	All un-toleranced dimensions to adhere to ISO 2768-m	Title: Base_Female		
Checked :	Material : Polyester Resin	Drawing Number : M_1	Rev. : A	Sheet : 1 of 1

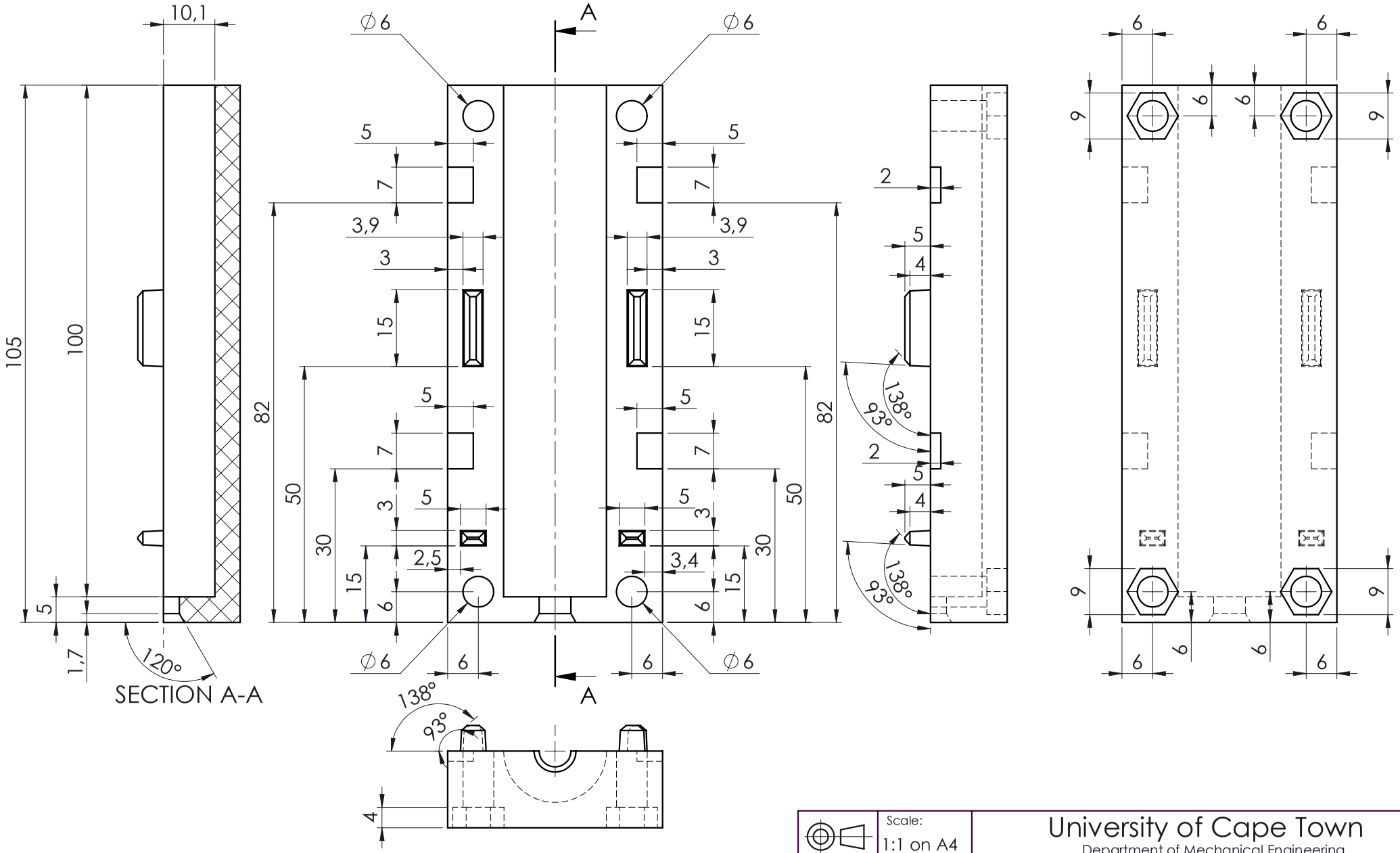

Scale: 1:1 on A4	University of Cape Town Department of Mechanical Engineering			
Drawn By: Matthew Hoare	All un-toleranced dimensions to adhere to ISO 2768-m	Title: Base_Male		
Checked :	Material : Polyester Resin	Drawing Number : M_2	Rev. : A	Sheet : 1 of 1

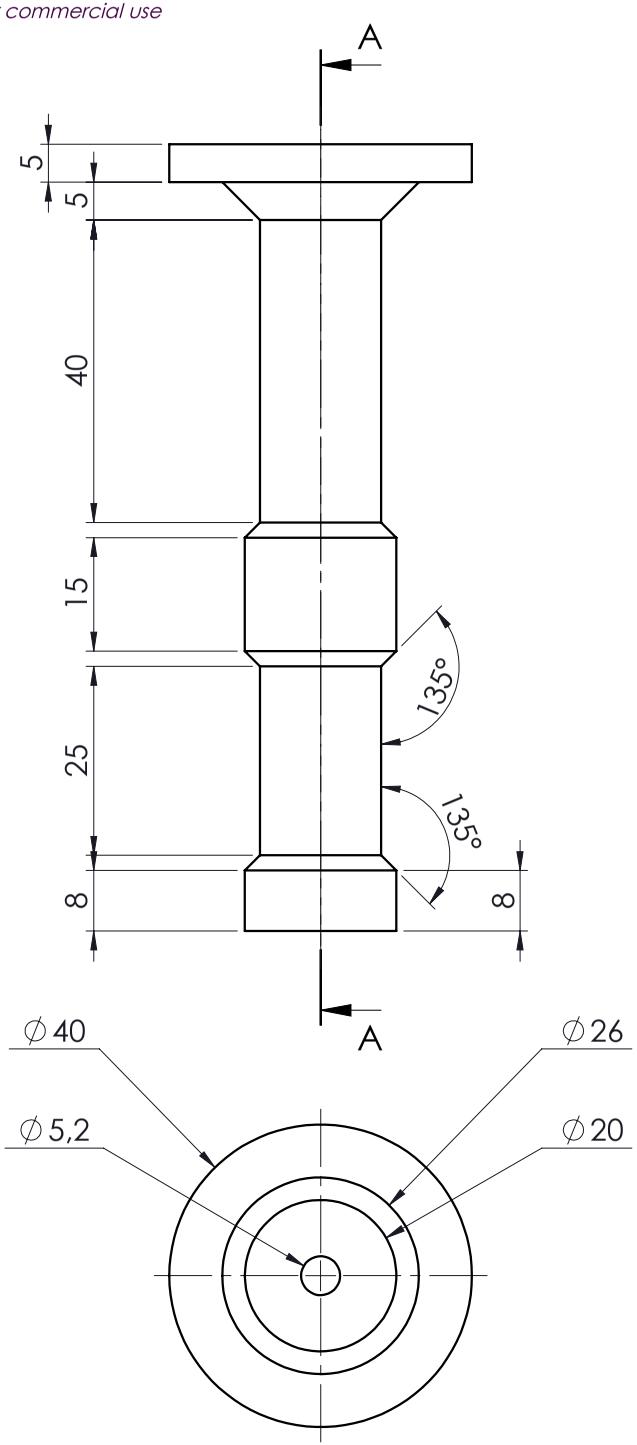

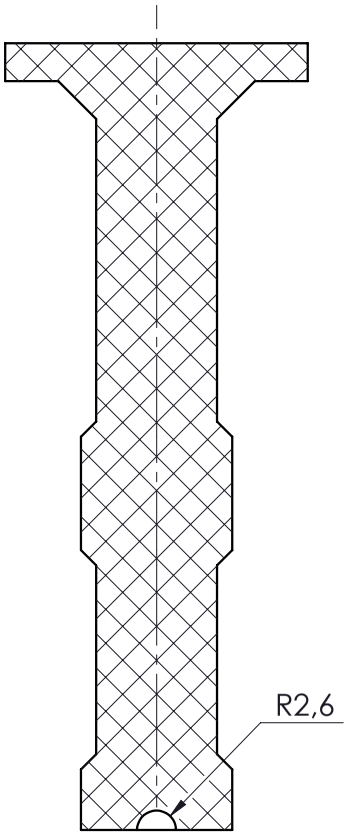

SECTION A-A

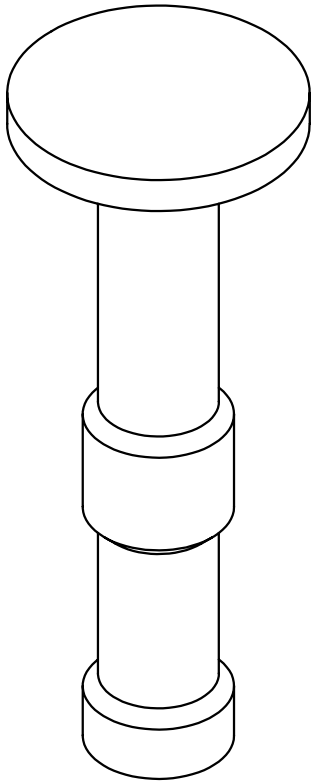

Scale: 1:1 on A4	University of Cape Town Department of Mechanical Engineering			
Drawn By: Matthew Hoare	All un-toleranced dimensions to adhere to ISO 2768-m	Title: Dented Press		
Checked :	Material : Polylactic Acid	Drawing Number : M_5	Rev. : A	Sheet : 1 of 1

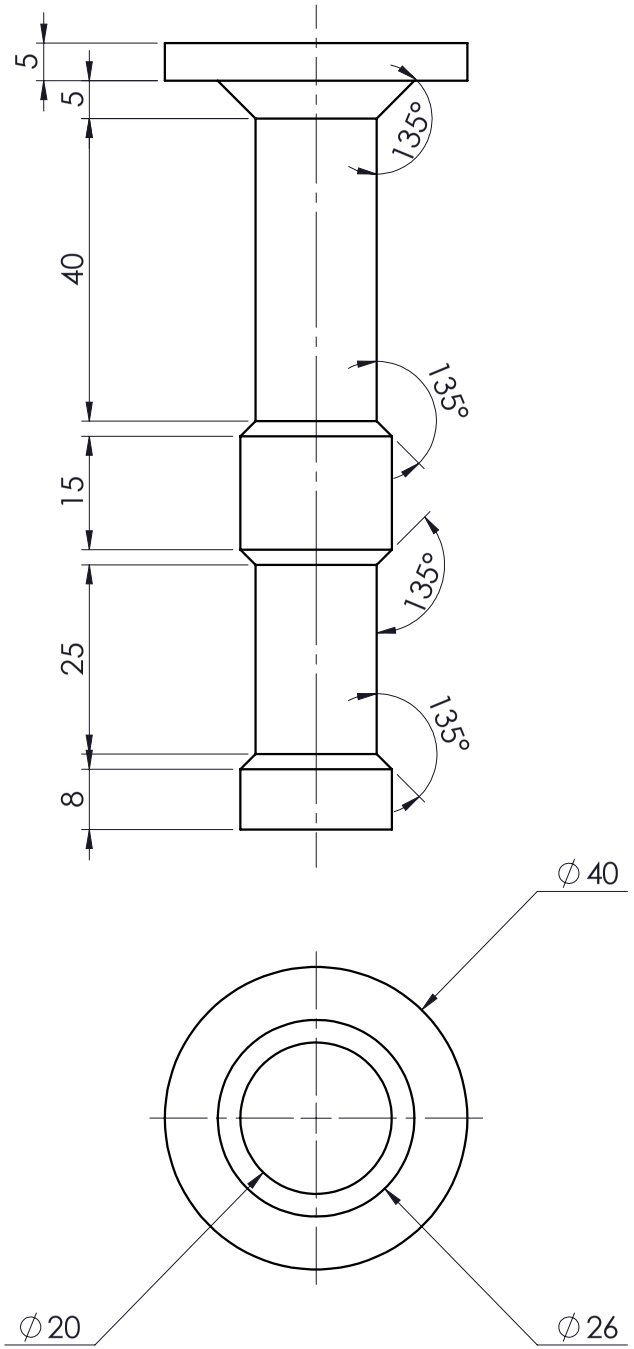

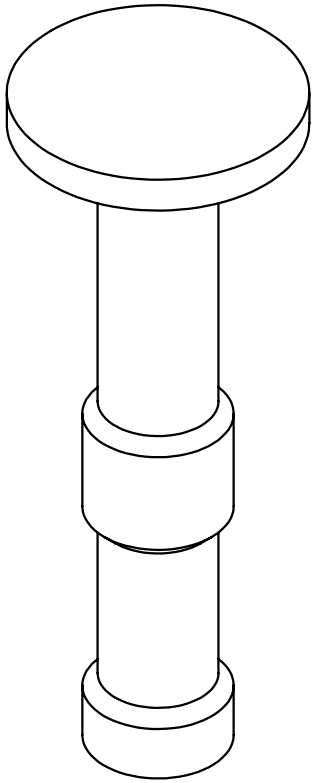

Scale: 1:1 on A4	University of Cape Town Department of Mechanical Engineering			
Drawn By: Matthew Hoare	All un-toleranced dimensions to adhere to ISO 2768-m	Title: Flat Press		
Checked :	Material : Polylactic Acid	Drawing Number : M_4	Rev. : A	Sheet : 1 of 1

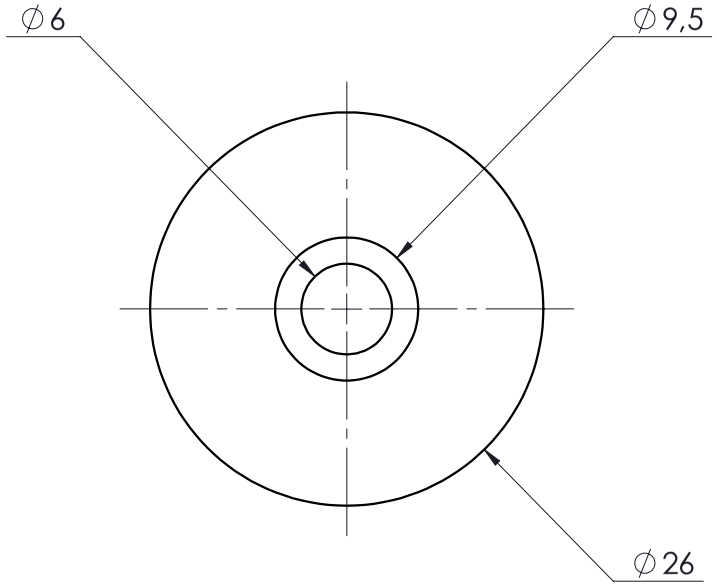

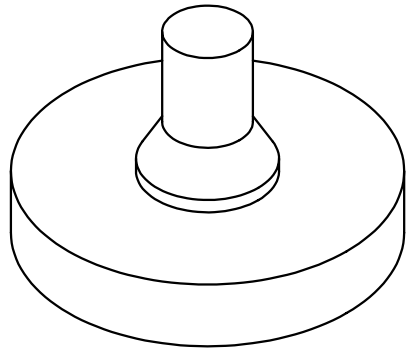

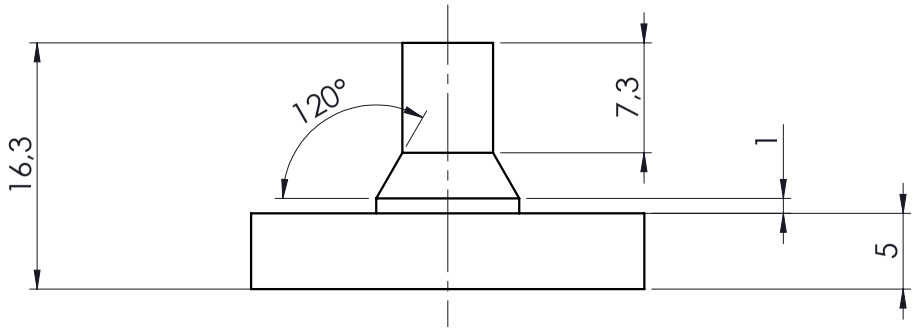

Scale: 2:1 on A4	University of Cape Town Department of Mechanical Engineering			
Drawn By: Matthew Hoare	All un-toleranced dimensions to adhere to ISO 2768-m	Title: Detonator Press		
Checked :	Material : Polyester Resin	Drawing Number : M_3	Rev. : A	Sheet : 1 of 1

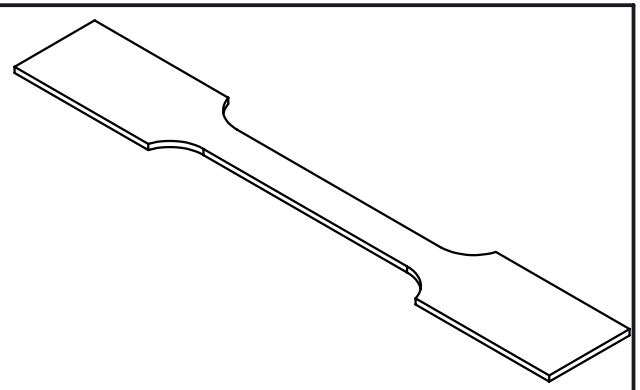

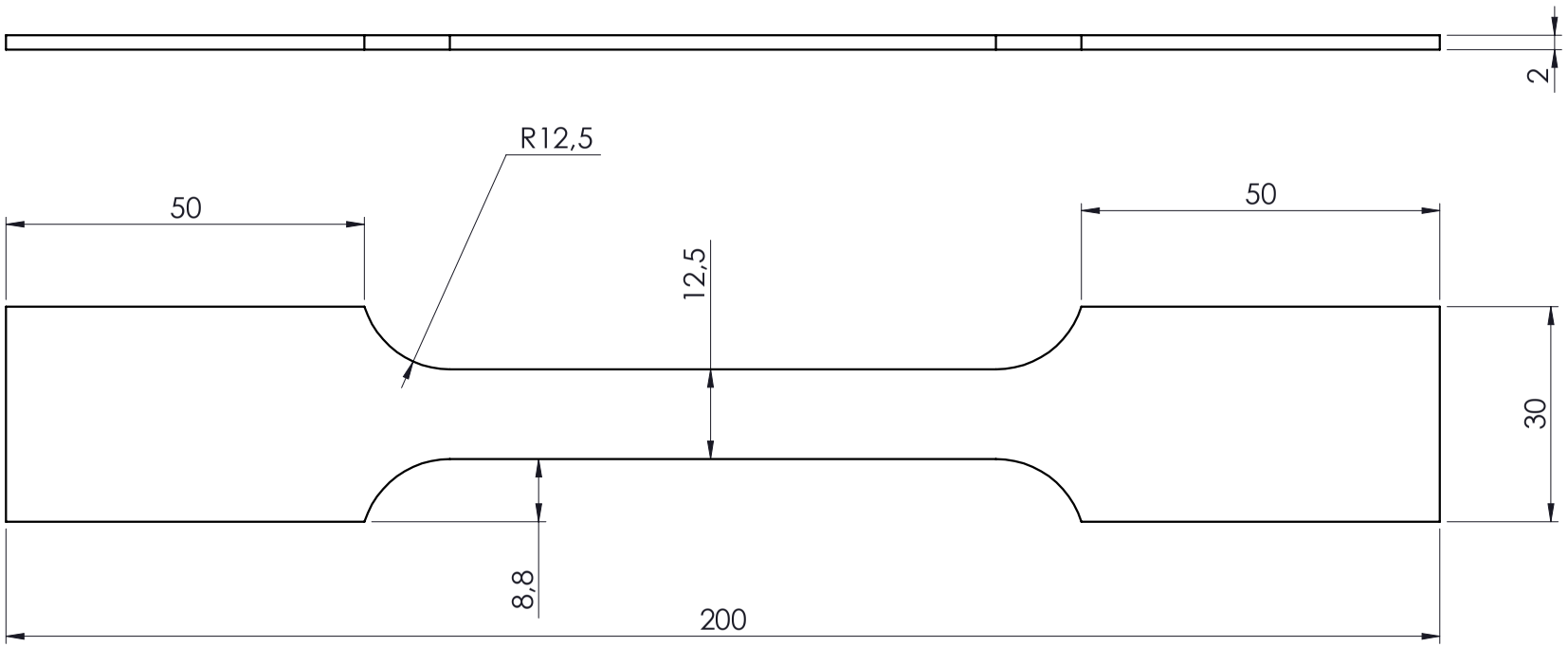

Quantity:
20

Scale: 1:1 on A4	University of Cape Town Department of Mechanical Engineering			
Drawn By: Matthew Hoare	All un-toleranced dimensions to adhere to ISO 2768-m	Title: Tensile Testing Specimen		
Checked :	Material : Domex 700	Drawing Number : 9	Rev. : A	Sheet : 1 of 1